HIGHLIGHTS 2019

MAX IV

Partners


Vetenskapsrådet


VINNOVA


Knut och Alice
Wallenbergs
Stiftelse


REGION
SKÅNE


LUND
UNIVERSITY


CHALMERS


UNIVERSITY OF
GOTHENBURG


Karolinska
Institutet


KTH


LULEÅ
UNIVERSITY
OF TECHNOLOGY


Stockholm
University


SLU


UPPSALA
UNIVERSITET


UMEÅ
UNIVERSITET


TREESEARCH


midt
regionmidtjylland


REGION
The Capital Region
of Denmark


Ministry of Higher Education
and Science – Denmark


novo
nordisk
fonden


UNIVERSITY OF
COPENHAGEN


DTU


AARHUS UNIVERSITY


ACADEMY
OF FINLAND


UNIVERSITY
OF OULU


UNIVERSITY
OF TURKU


Tampere University


UNIVERSITY OF HELSINKI

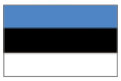


TARTU ÜLIKOOL
1632
UNIVERSITY OF TARTU

TABLE OF CONTENTS

Foreword

2019 was a landmark year for MAX IV Laboratory.

Continuing the long-standing tradition of delivering innovative technical instruments and capabilities for x-ray science to the research community since MAX-lab was inaugurated in 1987, MAX IV broke new ground by opening five new beamlines to users, and bringing three more into the commissioning phase for a total of eleven that “see the light”, including all five beamlines planned for the 1.5 GeV storage ring.

This number of beamlines is on par with the total operating at the former MAX-lab by the time it closed at the end of 2015.

2019 also marked substantial advances in the capabilities of the MAX IV accelerator systems on top of their regular stable and reliable operation, such as routine delivery of 400 mA stored current to the 1.5 GeV ring and 250 mA to the 3 GeV ring in multibunch mode.

Single-bunch became a regular delivery mode in the 1.5 GeV ring and an improved version multipole-injection kicker developed in collaboration with the SOLEIL team allowed for near-transparent injection into the 3 GeV ring.

In short, completion of the MAX IV laboratory portfolio of 16 funded beamlines is well along as they join the linear accelerator and two storage rings, including the world's first fourth-generation storage ring, in full-time operations.

More importantly, this year witnessed significant growth in the scientific activities at MAX IV by comparison to 2018: approximately 700 user visits to MAX IV up from 370, 450 proposals up from 140, and delivery of 3000 4-hour shifts up from 1300.

Nearly 50 peer-reviewed publications arose from research at MAX IV Laboratory. Several of these appeared in top scientific journals, highlighting the growing scientific impact and recognition of MAX IV research across a diverse range of disciplines.

Examples include uncovering additional molecular binding sites in cholera toxin, discovering a new family of copper-binding proteins potentially useful for converting agricultural products to biofuel, revealing a new emission mechanism that could lead to fast and cheap organic light-emitting diode display technologies, greater understanding of reaction mechanisms in single-atom catalysis, and a compelling demonstration that the focus of a coherent, nano-focused x-ray beam becomes tighter as the photon energy is increased, according to the famed “diffraction limit”.

This progress by the MAX IV staff and user community is all the more noteworthy in that it resulted during a very challenging year of intense construction and commissioning activities, overcoming several technical challenges, undergoing two major reviews, conducting a highly successful user meeting, on-boarding many new staff, and working within a tight operating budget.

I would like to thank everyone who contributed to this year's edition of MAX IV Highlights. I hope you enjoy reading about the outstanding accomplishments at MAX IV over the past year and that it will inspire you to even greater achievements in the future.

Ian McNulty
Director, MAX IV Laboratory

Science Highlights

Self-cleaning and surface chemical reactions during hafnium dioxide atomic layer deposition on indium arsenide

The atomic layer deposition of hafnium oxide on a III-V semiconductor surface offers a way to acquire the important defect free interface needed for next generation electronics. In this study the properties of the surface during the deposition process have been studied by Ambient pressure X-ray Photoelectron Spectroscopy at beamline SPECIES.

The Science

III–V semiconductors such as indium arsenide (InAs) or gallium arsenide (GaAs) are central candidates for next-generation high-speed/low-power electronics, mainly because their electron mobility is much larger than that of Si. However, one key challenge in using these materials is the detrimental effect of high interface trap densities, which are caused by unwanted oxides, atomic vacancies, dimers, or other atomic-scale interface defects formed during device fabrication.

These can in particular limit the performance of nanoscale metal-oxide-semiconductor field effect transistors (MOSFETs), which critically relies on the structural quality of the semiconductor–oxide interface. Strong improvement on this issue has been obtained by depositing ultra-thin barriers of hafnium dioxide (HfO_2) which not only has a high dielectric constant (high-k), but also potentially can substitute the native oxide with a well-controlled, stable, and defect-free semiconductor–oxide interface.

Here, we directly observe the chemical reactions at the surface during the initial hafnium dioxide deposition on indium arsenide under realistic synthesis conditions using photoelectron spectroscopy. We find that the widely used ligand exchange model of the atomic layer deposition (ALD) process for the removal of native oxide on the semiconductor and the simultaneous formation of the first hafnium dioxide layer must be significantly revised.

Our study provides substantial evidence that the efficiency of the self-cleaning process and the quality of the resulting semiconductor–oxide interface can be controlled by the surface chemistry involved in the molecular adsorption process of the metalorganic ALD precursor, rather than the subsequent oxide formation.

The Impact

ALD enables the ultrathin high-quality oxide layers that are central to all modern metal-oxide-semiconductor circuits. Crucial to achieving superior device performance are the chemical reactions during the first two half-cycles of the ALD process, which could ultimately result in atomic-scale perfection of the semiconductor–oxide interface. Previously, this process was typically studied by comparing surfaces before and after oxide deposition. Here, we present a time-resolved study of the self-cleaning effect occurring during the first few ALD half-cycles of HfO_2 deposition on InAs using ambient-pressure XPS (AP-XPS) with an in-vacuum gas cell design.

An almost perfect self-cleaning has been observed here by carefully monitoring the ALD reactions until they were completely finished. The study thus provides a perspective towards establishing fully defect-free semiconductor/high-k oxide interfaces as a source for superior device performance.

Summary

In our setup we can monitor chemical reactions between a solid surface and reactive gases flowing through the system under realistic synthesis conditions. We find that the formation of HfO_2 on the InAs surface during the first ALD half-cycle is

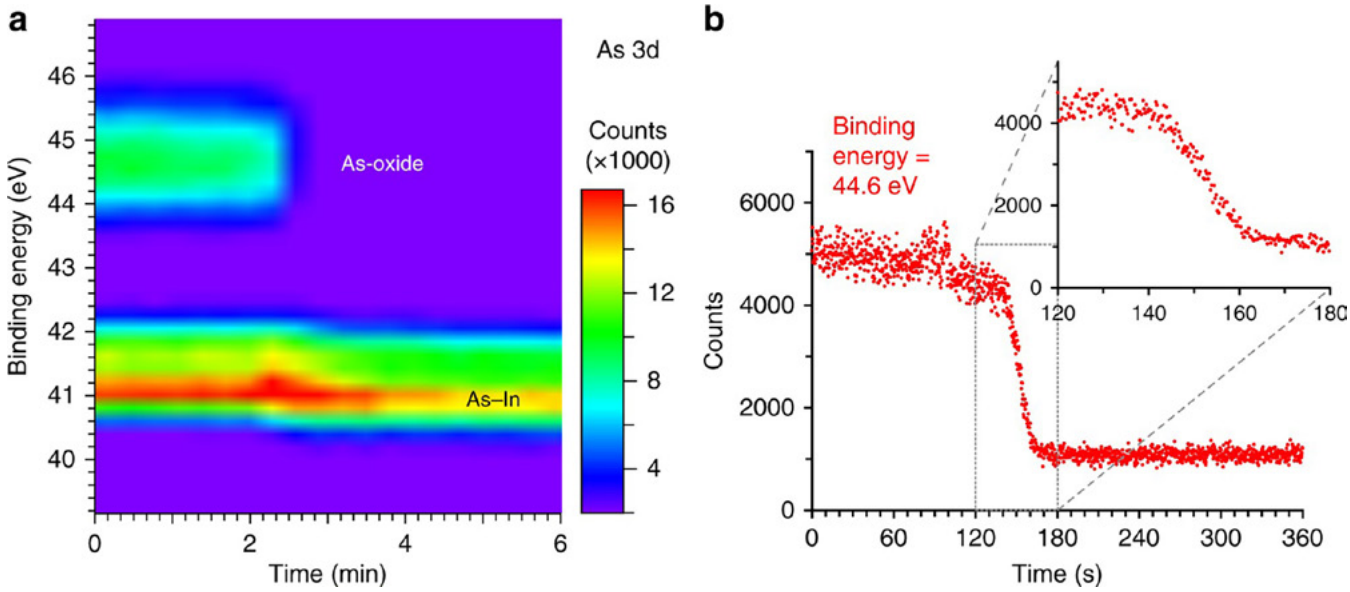

Time-resolved arsenic-oxide removal. a) Time evolution of As 3d XPS core level spectra during exposure to TDMA-Hf. Components corresponding to As oxide and to As bound to In (bulk) can clearly be distinguished at binding energies of 44.6 eV and 41 eV, respectively. The oxide component is removed completely after an initial delay of about 2 min, accompanied by a shift in binding energy of the bulk component. The time interval between subsequent spectra was 17 s. b) Time evolution of the XPS peak intensity at a binding energy of 44.6 eV, corresponding to the maximum of the As-oxide peak, during exposure to TDMA-Hf. The inset shows a zoom-in at the time period of strong oxide removal. The timescales correspond to the opening of the gas inlet valve. Spectra were obtained at a photon energy of 320 eV, a gas pressure of about 1 Pa, and a sample temperature of 200 °C (a) and 220 °C (b)

preceded by the presence of hafnium (Hf) atoms in a different chemical configuration, which we interpret as molecular adsorption of the metalorganic Hf precursor.

These findings challenge the established view of the ALD process. Current understanding of how the high-k oxide layer forms by ALD is based on the ligand exchange model, where the metalorganic precursor molecule splits off one of its ligands and instead forms a bond to an oxygen (O) atom from the sample surface, thereby replacing the unwanted native oxide with a high-quality high-k oxide film. In contrast, our results indicate that the molecular adsorption of the Hf-precursor molecules occurs prior to the ligand split-off, and that the native oxide is desorbed already during this precursor adsorption step, prior to Hf–O bond formation.

In fact, we observe an almost complete removal of the native oxide, including several As-oxide and In-oxide components. Our results have three important implications: (1) They call for significant revisions of the established ligand exchange model to describe the ALD process. (2) They yield an understanding of how a typically several monolayer thick native oxide layer is removed while only a sub-monolayer thick high-k oxide film is formed—this has been one of the main shortcomings of the ligand exchange model. (3) They point to new strategies for improving the interface quality between III–V semiconductors and high-k oxides by optimizing the ALD kinetics. While we chose to study ALD of HfO_2 on InAs because of its high technological relevance, our experimental approach using AP-XPS and the reported mechanistic insights on semiconductor–oxide interface formation are not limited to this system, but are relevant for understanding surface chemistry processes during ALD in general.

Funding

This work was performed within the NanoLund Centre for Nanoscience at Lund University, and was further supported by the Swedish Research Council, the Swedish Foundation for Strategic Research , the Crafoord Foundation, the Knut and Alice Wallenberg Foundation, and the European Research Council as well as the European Commission under the European Union's Seventh Framework Programme, Grant Agreements Nos 251862, 259141, and 608153.

Publication

Timm, R., Head, A.R., Yngman, S. *et al*. Self-cleaning and surface chemical reactions during hafnium dioxide atomic layer deposition on indium arsenide. *Nat Commun* **9**, 1412 (2018). https://doi.org/10.1038/s41467-018-03855-z Open Access

A combination of gel forming biomolecules for enhanced properties

A gel network formed by combining the biomolecules sodium deoxycholate and L-Phenylalanine was characterised at beamline I911-4 at MAX II. The resulting self-standing gel is formed in the pH 10–12 range and has an uncommon thermal stability in the range of 20–60°C. Gel networks are important as biocompatible materials in diverse areas from medical applications to catalysis or food.

The Science

Supramolecular hydrogels are 3D networks showing ability to entrap water and remarkable viscoelastic properties. The non-covalent character of the stabilizing interactions imparts higher structure responsiveness, reversibility, and adaptability than the polymeric gels. Owing to these properties, hydrogels turn out to be versatile materials for cosmetic formulation, tissue growth, drug delivery, catalysis and food industry.

Bile salts (BSs) are bio-surfactants produced in the liver and stored in the gallbladder. They play a critical role in the emulsification of fats and fat-soluble vitamins for their absorption in the intestine. Gelling properties can be tuned or introduced in not naturally gelling BSs by varying ad hoc the hydrophobic/hydrophilic balance of the system or by introducing additional stabilizing forces. The bile salt sodium deoxycholate (NaDC) forms gels upon protonation of the carboxylic groups in water (by lowering the pH) or upon addition of charge screening salts.

L-Phenylalanine is one of the building blocks of life. It is an essential amino acid in humans and its introduction through the diet is crucial for peptide synthesis and for the biosynthesis of tyrosine. As for BSs, it has been shown that specific derivatizations can vary the self-assembly properties of Phe, giving rise to more efficient gelling systems than the precursor.

In the light of the broad interest in NaDC and Phe hydrogels, in this work we couple both building blocks in a new derivative. Ca2+ ions were introduced in the sample for the coordination of the carboxylic heads, allowing thus for an efficient involvement in the assembly of the flexible chains as well. The overall strategy enabled an unprecedented result: the formation of hydrogels that are based concurrently on Phe and NaDC.

The Impact

The gels hold great potential in medicine and biology as drug carriers and models for fundamental self-assembly in pathological conditions.

Summary

Sodium Deoxycholate (NaDC) and Phenylalanine (Phe) are important biological hydrogelators. NaDC hydrogels form by lowering the pH or by increasing the ionic strength. Phe gels form from saturated solution by thermal induction and slow kinetics. Based on this background it was hypothesized that a Phe substituted NaDC could provide a molecule with expanded gelling ability, merging those of the precursors.

We coupled both building blocks in a zwitterionic derivative bearing a Phe residue at the C3 carbon of NaDC. The specific zwitterionic structure, the concurrent use of Ca2+ ions for the carboxyl group coordination and the pH control generate conditions for the formation of hydrogels. The hydrogels were analyzed by combining UV and circular dichroism spectroscopies, rheology, small angle X-ray scattering and atomic force microscopy. The SAXS measurement on the pure β-L-PheDC sample at pH 12 was performed at the MAX II SAXS beamline I911-4.

Self-standing gels form instantaneously at room temperature, in the 10–12 pH range and down to

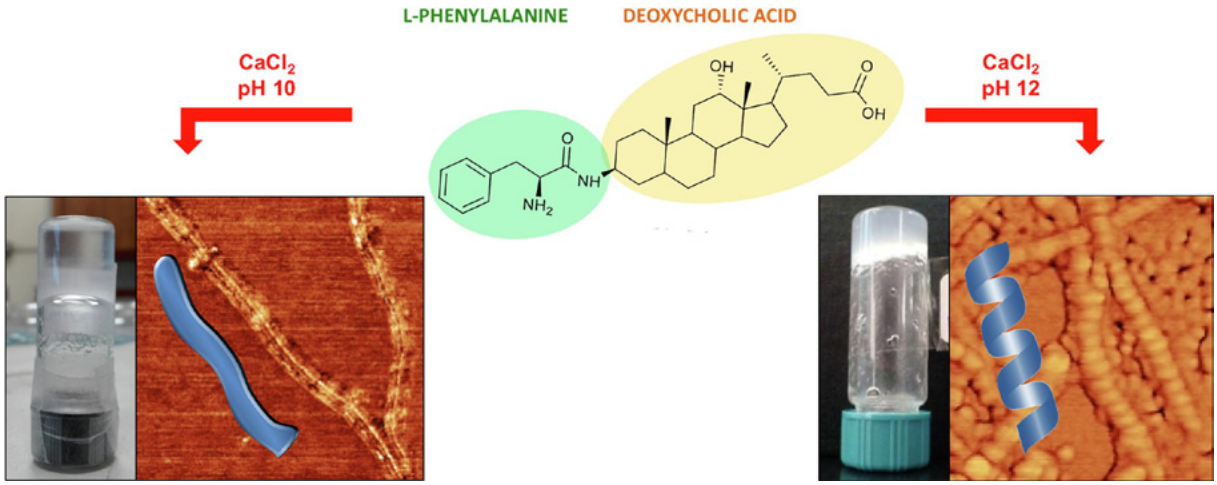

Hydrogels formed in the pH 10–12 range by a combination of L-Phenylalanine and deoxycholic acid.

concentration of 0.17 wt%. Both thixotropic and shake resistant gels can form depending on the derivative concentration. The gels show an uncommon thermal stability in the scanned range of 20–60 °C. The reported system concurrently enriches the hydrogelation properties of two relevant building blocks. We anticipate some potential applications of such gels in materials science where coordination of metal ions can be exploited for templating inorganic nanostructures.

Calcium promoted gelation lets us envision a general ability of the derivative to provide gels at high swelling degree by exploiting metal coordination. This ability with different metals will be investigated in future works.

Funding

The authors thank Sapienza University of Rome and Universidad de Costa Rica for financing the agreement of cultural and scientific cooperation.

Publication

Reprinted from L. Travaglini, M. C. di Gregorio, E. Severoni, A. D'Annibale, S. Sennato, F. Tardani, M. Giustini, M. Gubitosi, A. Del Giudice, L. Galantini, Deoxycholic acid and L-Phenylalanine enrich their hydrogel properties when combined in a zwitterionic derivative, Journal of Colloid and Interface Science, 554, 2019, 453-462 with permission from Elsevier
https://doi.org/10.1016/j.jcis.2019.07.019

Novel ways to understand and achieve efficient Layered Double Hydroxides

The intercalation properties of layered double hydroxides (LDH) have scientific and commercial interest in several fields. This study shows the effects of ultrasonic irridiation on co-precipitated CaFe-layered double hydroxide, an LDH frequently used in water treatment, as drug transporter and as catalyst or catalyst support.

The Science

The output power (30–150 W) and the periodicity (20–100%) of ultrasound emission were varied in a wide range to regulate and improve the crystallization process in the commonly used co-precipitation technique of chloride-intercalated Ca-Fe-layered double hydroxides.

The influence of ultrasound irradiation on the as-prepared materials was studied by X-ray diffractometry, dynamic light scattering, UV–Vis–NIR diffuse reflectance spectroscopy, specific surface area measurement, pore size analysis, ion-selective electrode potentiometric investigations and thermogravimetry. Additionally, structural alterations due to heat treatment at various temperatures were followed in detail by Fourier-transform infrared and X-ray absorption spectroscopies as well as scanning electron microscopy.

The ultrasonic treatment was capable of controlling the sizes of primarily formed (from 19 nm to 30 nm) as well as the aggregated (secondary) particles (between 450 nm and 700 nm), and thus modifying their textural parameters and enhancing the incorporation of chloride anions into the interlamellar space. For the first time, the optical energy gap of CaFe-LDH was reported here depending on the nature of applied stirring (4.18–4.34 eV). The heat-treatment investigations revealed that the layered structure was stabile until 200 °C, even at the atomic level. XAS measurements were performed at I811 (MAX II ring).

The Impact

LDH are a class of ionic solids characterized by a layered structure of metal cations, layers of hydroxide, and layers of other anions and neutral molecules Naturally occurring (i.e., mineralogical) examples of LDH are classified as members of the hydrotalcite supergroup, named after the Mg-Al carbonate hydrotalcite, which is the longest-known example of a natural LDH phase.

The layers of anions in LHDs can, in general, be easily replaced, which has led to an intense interest in using man-made (syntetic) LDHs for advanced applications. Examples are drug delivery, removing agrochemicals from polluted water, in polymer production, in suspensions for self-cleaning of surfaces and as catalysts.

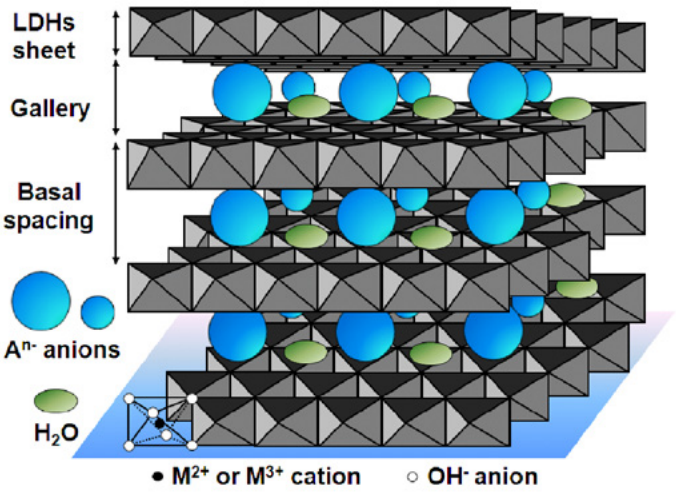

Schematic representation of the structure of layered double hydroxides (LDHs). Source Researchgate.

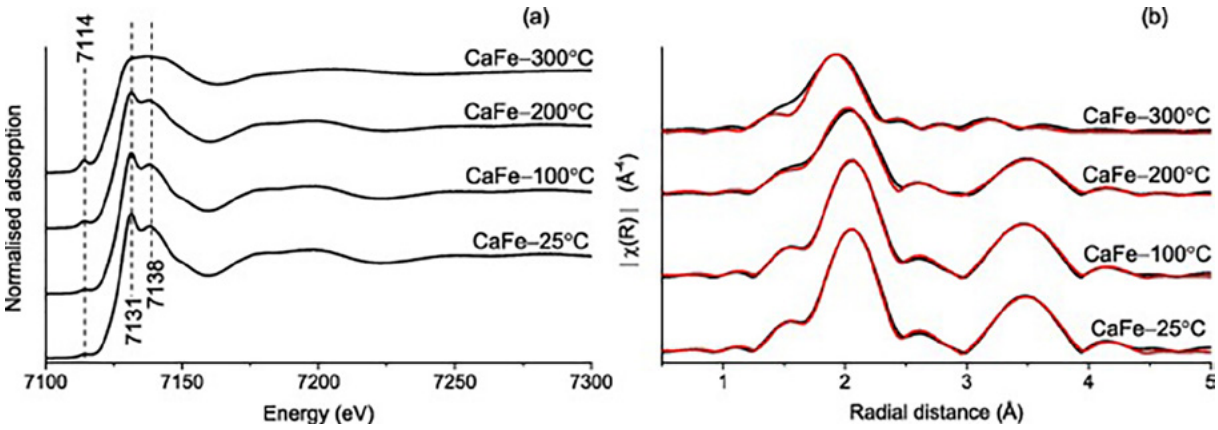

The raw Fe K-edge X-ray absorption spectra (a), the Fourier-transformed and fitted NEXAFS/EXAFS spectra (b) of heat-treated CaFe-LDH samples. The black lines are the experimental data and the red ones are the fitted curves.

Summary

Ultrasonic treatment was applied to regulate the crystallization process of CaFe-layered double hydroxide with chloride interlayer anions. The influences of the output power and the emission periodicity were studied on the size as well as the aggregation, the textural and the optical parameters beside the dissolution and thermal behaviour of LDH particles.

In every case, the application of low-performance (30 W) ultrasonic irradiation proved to be the most beneficial way to prepare well-developed hexagonally-shaped crystallites. At continuous emission, the formation of layered structure was aided by higher crystal thicknesses and enhanced anion intercalation. With discontinuous, 60% radiation periodicity, the porosity and uniform size distribution of particles were developed as well as the aggregation tendency was partially inhibited.

The optical properties of LDHs proved to be tuneable by applying mechanical or ultrasonic stirring. The weathering test revealed an elongated Ca(II) release due to the incorporation of Fe(III) cations.

The knowledge of heat treatment on CaFe-LDHs was broadened by infrared and X-ray absorption measurements revealing that the internal layered structure of CaFe-LDH did not change until 200 °C, while dehydration became remarkable at higher temperatures and long-range ordering was lost on heat treatment above 300 °C.

Funding

This work was supported by the European Union and the Hungarian government through grant GINOP-2.3.2-15-2016-00013 and by the NKFIA K 124265 grant.

Publication

Reprinted from M. Szabados, A.A. Ádám, Z. Kónya, Á. Kukovecz, S. Carlson, P. Sipos, I. Pálinkó, Effects of ultrasonic irradiation on the synthesis, crystallization, thermal and dissolution behaviour of chloride-intercalated, co-precipitated CaFe-layered double hydroxide, Ultrasonics Sonochemistry, 55, 2019, 165-173 with permission from Elsevier.
https://doi.org/10.1016/j.ultsonch.2019.02.024

Increasing light emissions through energy transfer of different, excited spin states

The capacity to extract light energy through conversion of different molecular spin states plays an important role in advancing material chemistry and its applications in organic electronic device. We present a molecular dyad exibiting novel capability for Förster-type triplet-to-singlet energy transfer as a method to increase the rate of light extraction from excited triplet states.

The Science

Förster-type resonance energy transfer (FRET) is a tool used to manipulate electronically excited states of organic molecules.

We demonstate that energy transferal from an excited triplet state – known as phosphorescence – to singlet state, is possible utilizing a donor-bridge-acceptor dyad (DBA) molecule. This result occurred without energy loss in the transfer.

Emission from triplet states is quantum-mechanically forbidden, yet still occurs at a very low rate. The transfer rate from triplet to singlet energy state, however, was found to be 36 times faster than the rate of emission from isolated triplet states.

The Impact

The results bring us a step toward solving how to increase light emission in phosphorescent compounds with triplet states, the most common energy state, which typically supplies low emissions. This knowledge is of practical importance for the development of highly efficient and stable electronic devices such as organic light-emitting diodes (OLEDs).

Summary

The study provides a first example of intramolecular triplet-to-singlet energy transfer. We show that it is possible to transfer excited-state energy through the Förster mechanism (a dipole-dipole interaction) without conserving the spin angular momentum. The results are based on synthesis of a donor-bridge-acceptor dyad (DBA) with donor and acceptor units tightly fixed within the molecular framework.

The DBA molecule makeup includes three major components; donor, acceptor and bridge element. The selected donor was IrIII complex bearing tripodal, facially coordinated phosphite and 2-pyridyltriazolate ligand. This photostable iridium complex has been shown to exhibit blue phosphorescence and been used in state-of-the-art OLEDs that possess deep-blue chromaticity.

Taking into consideration the emission spectrum of the donor, perylene was selected as a suitable acceptor counterpart. Perylene is a well-studied chromophore with a fluorescence quantum yield close to unity and a small Stokes shift. A rigid bridging unit, bicyclo octane, was chosen because it permits free rotation only along the long axis of the molecule offering a stable position for the functional counterparts of the dyad.

X-ray diffraction data of the ligand was collected at BioMAX beamline. Its crystal structure was solved and refined using the SHELXT system.

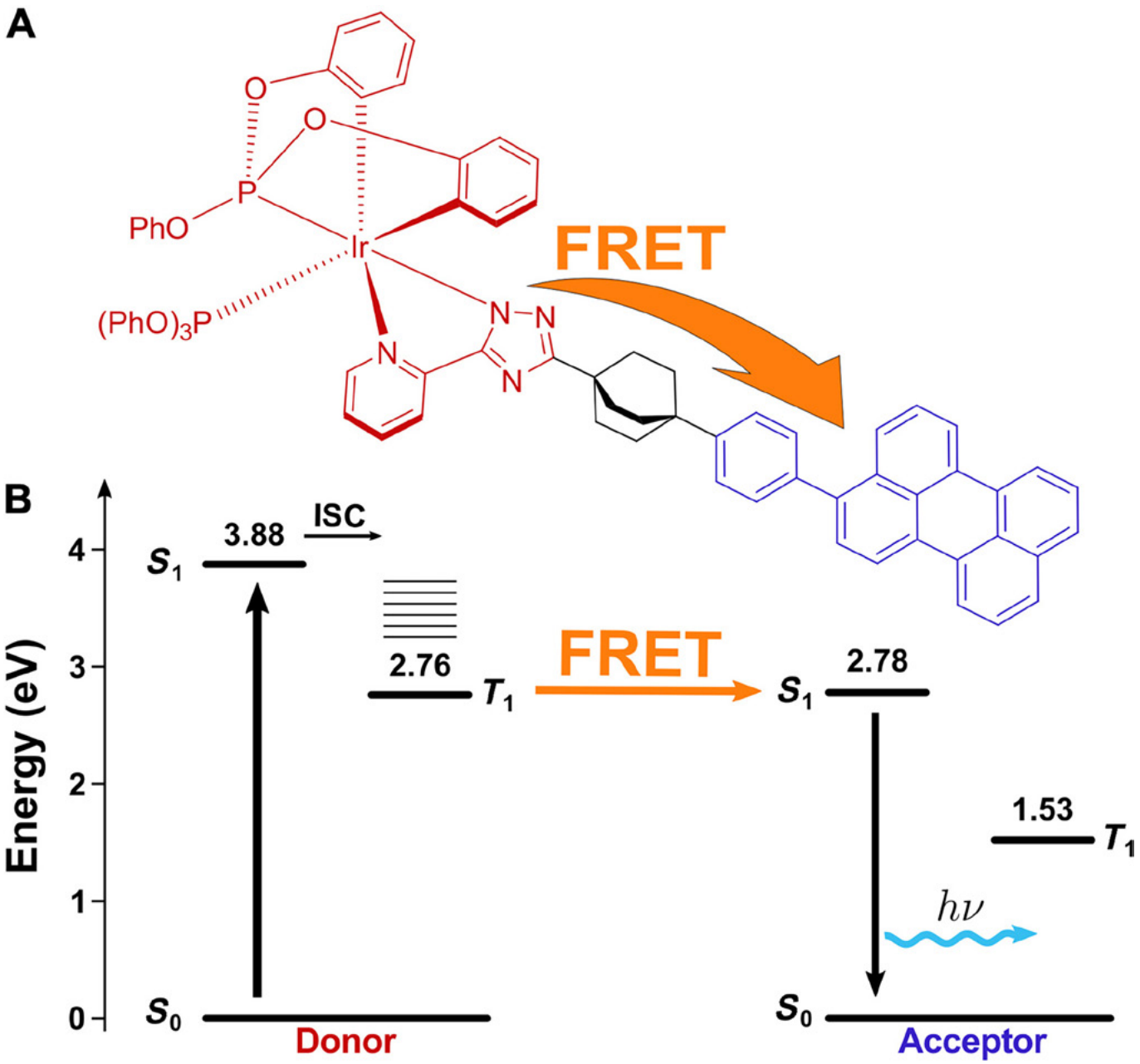

Structure and energy levels of the dyad.

(A) The DBA molecule used in this study.
(B) Jabłoński diagram showing triplet-to-singlet energy transfer via dipole-dipole interactions, i.e., the Förster-type resonance energy transfer (FRET) mechanism.

Funding

The European Research Council (ERC-2017-StG-757733), the Swedish Research Council (2016-03354), and the Swedish Foundation for Strategic Research (ICA14-0018) for financial support.

Publication

A. Cravcenco, M. Hertzog, C. Ye, M. N. Iqbal, U. Mueller, L. Eriksson, K. Börjesson.
Multiplicity conversion based on intramolecular triplet-to-singlet energy transfer
Science Advances, 20 Sep. 2019: Vol. 5, no. 9, eaaw5978.
https://doi.org/10.1126/sciadv.aaw5978
Open Access

Understanding the chemistry in tiny water droplets help climate modeling

The effects of atmospheric aerosols are among the major uncertainties for climate modeling. Due to the small size of atmospheric aerosol particles, surface effects are important for their properties. Evidences have been presented that accumulation of neutral organic compounds in the surface region hamper water evaporation from atmospheric droplets.

The Science

Cloud droplet formation from aerosol particles called cloud condensation nuclei, and heterogeneous reactions at aerosol surfaces are two important examples of these effects. Organic compounds are often surface active, and there is a large variety of oxidized organic compounds present in the atmosphere. Many of these originate from reduced organic compounds with low water solubility, which due to the oxidizing properties of the atmosphere are readily oxidized to substantially more water soluble compounds.

There is very strong evidence that atmospheric particles contain surface active compounds accumulated in the surface region lowering the surface tension. The accumulation of neutral organic compounds in the surface region may also have an impact on transport across the surface region.

The Impact

The results from this study increase the knowledge about the distribution of chemical species in the surface region at and close to the water–air interface, and the transport of chemicals from water to air in open systems. The findings are of particular importance for small water droplets with large surface area:bulk volume ratio in air where dynamic equilibria between air and water drops exist.

Summary

Previous studies have shown that the water–air interface and a number of water molecule layers just below it, the surface region, have significantly different physico-chemical properties, such as lower relative permittivity and density, than bulk water.

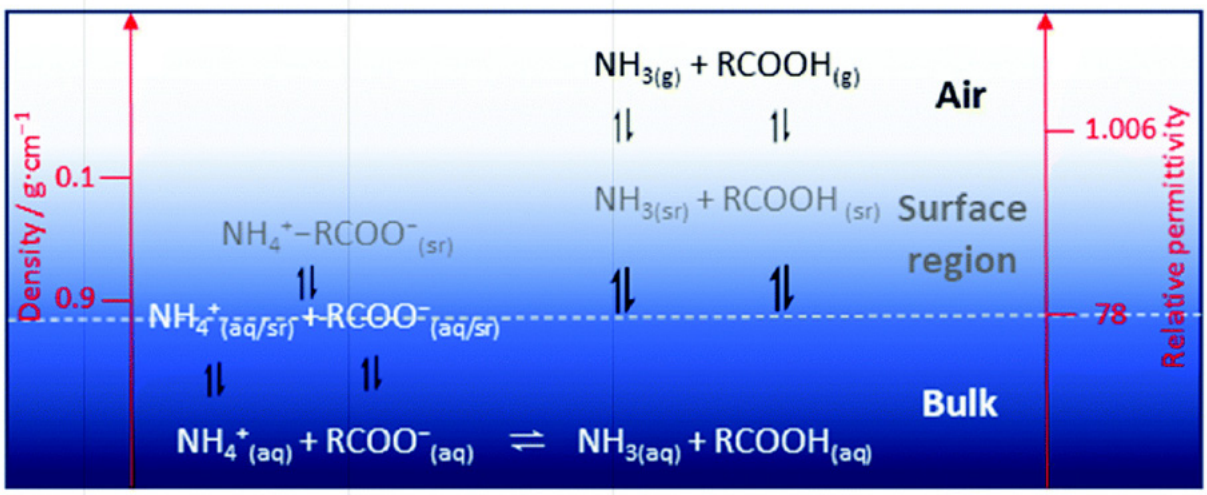

Equilibria of ammonium and carboxylate ions, ammonia and carboxylic acid in the aqueous bulk (bulk), the interface water–air (surface region) and open air. The dashed line represent the border for bulk water properties.

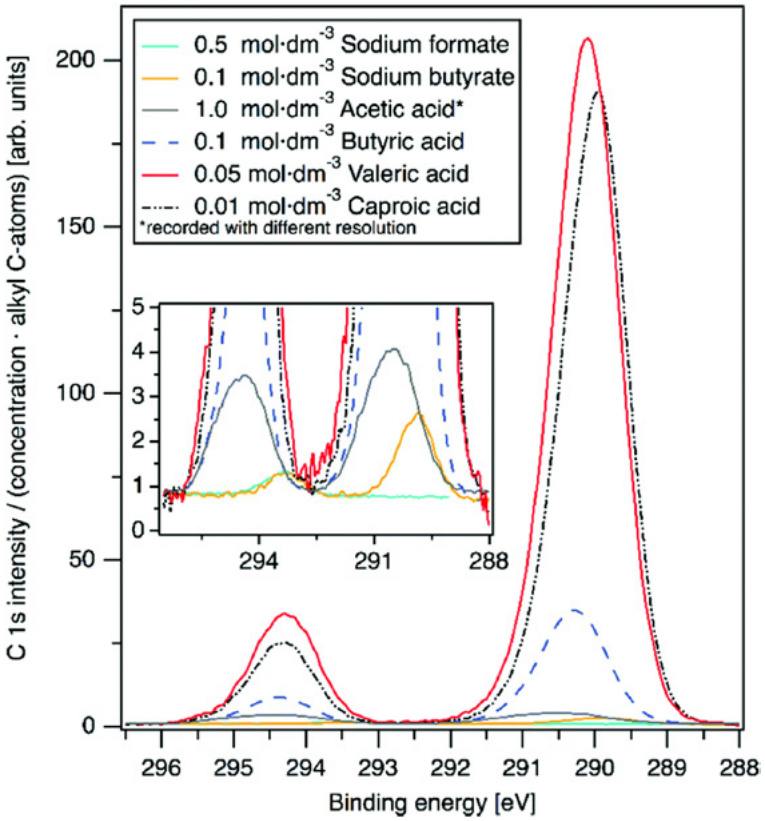

C 1s XPS spectra of sodium formate and butyrate, and acetic, butyric, valeric and caproic acid in aqueous solution measured as a liquid micro-jet and normalized for concentration and number of carbon atoms in the alkyl chain. This normalization causes that the intensity of the peak at 294.3 eV (carboxylic acid or carboxylate carbon) is inverse to the number of carbons in the alkyl chain.

The properties in the surface region of water favor weakly hydrated species as neutral molecules, while ions requiring strong hydration and shielding of their charge are disfavored. In this study the equilibria $NH_4^+(aq) + RCOO^-(aq) \rightleftharpoons NH_3(aq) + RCOOH(aq)$ are investigated for R=C-nH_{2n+1}, n=0–8, as open systems, where ammonia and small carboxylic acids in the gas phase above the water surface are removed from the system by a gentle controlled flow of nitrogen to mimic the transport of volatile compounds from water droplets into air.

It is shown that this non-equilibrium transport of chemicals can be sufficiently large to cause a change of the chemical content of the aqueous bulk. Furthermore, X-ray photoelectron spectroscopy (XPS), conducted at the I411 beamline (MAX II ring) has been used to determine the relative concentration of alkyl carboxylic acids and their conjugated alkyl carboxylates in aqueous surfaces using a micro-jet.

These studies confirm that neutral alkyl carboxylic acids are accumulated in the surface region, while charged species, as alkyl carboxylates, are depleted. The XPS studies show also that the hydrophobic alkyl chains are oriented upwards into regions with lower relative permittivity and density, thus perpendicular to the aqueous surface.

These combined results show that there are several chemical equilibria between the aqueous bulk and the surface region.

The analytical studies show that the release of mainly ammonia is dependent on its concentration in the surface region, as long as the solubility of the carboxylic acid in the surface region is sufficiently high to avoid a precipitation in/on the water–air interface. However, for *n*-octyl- and *n*-nonylcarboxylic acid the solubility is sufficiently low to cause precipitation. The combined analytical and surface speciation studies in this work show that the equilibria involving the surface region are fast.

Funding

For the financial support the Swedish Research Council is gratefully acknowledged.

Publication

Y.S. Blanco, Ö. Topel, É.G. Bajnóczi, J. Werner, O. Björneholm and I. Persson, Chemical equilibria of aqueous ammonium–carboxylate systems in aqueous bulk, close to and at the water–air interface, *Phys. Chem. Chem. Phys.*, 2019, **21**, 12434-12445 https://doi.org/10.1039/C9CP02449B
Open Access

Understanding how paint age gives new ways to preserve and restore old paintings

Paint consists of chemical substances which change with age. Understanding excatly how and why this change occur can help conservation professionals to find new ways of preserving and restoring old paintings.

The Science

This paper presents results from ongoing investigations of soft and dripping oil paint in art works by CoBrA's Karel Appel (1921–2006) and Asger Jorn (1914–1973). The work is part of the PhD-project *Investigation of soft and dripping paint in paintings from 1946–1971* where twenty-four paintings are being investigated. The paintings were chosen to represent a large variety of conditions: some with slightly soft and mainly stable paints, and others with deforming and dripping paints.

All paintings chosen had some paint with uneven fluorescence emitted from specific paint colours. Earlier studies have shown that fluorescence can be an indicator of softening paint. The softening paints and drips on the surface of some of these paintings show similar polarity features with mid-chain functionalized stearic acids and azelaic acid moieties. Our findings show there are several physical and chemical alterations within one degradation symptom that have to be understood when conservation treatments are considered in the future.

The Impact

At present, conservation professionals do not have satisfactory treatment options for long-term preservation of art works with such soft and dripping paints. Focal points of attention for conservators are surface cleaning, removal of drip material, consolidation of delaminations and hardening of soft paint.

A deeper understanding of these problems is required in order to understand in more detail why paint becomes soft again and what the potential behaviour of such paints will be in the future. Documentation and descriptions of the mechanisms behind the range and variations of degradation symptoms are of importance for development of strategies for conservation treatments in the future.

Summary

So far in this project the analysis and investigations into the condition of each painting show that the problem of softness, dripping and change of the paint layers shape or form is consistent for several painters working in the 50's and 60's, but the understanding of the nuances of symptoms and material combinations are more varied than encountered in the earlier studies. The analyses from DTMS, XRD, SEM-EDX, MS and FTIR studies each add their specific information.

MS and FTIR data provide insight into the organic chemistry as they identify organic components in soap structures and the various organic compounds present in paints and drips. Synchrotron X-ray diffraction is now adding information of their organization while at the same time identifying inorganic phases such as multiple calcium phosphate phases in the soft bone black paint.

The mobile drip material has no long-range structure while solid paint has a more "crystalline" order. This information and further insight into the interaction between crystalline phases and organic medium components – especially a developing mobile phase inside paints – will be vital to a further understanding of softening and dripping paints and development of conservation solutions. We know that several of the painters investigated for soft and dripping paint from the years 1950–1970 at one point worked in Paris. However on consideration, it is too early to conclude if this has any importance for the understanding of the problem, but this will be a focus for further studies.

Fig. 1. Details HOS 00007 Le nu bleu, Karel Appel 1960: a: in normal light; b: in UV light. Sample location for synchrotron X-ray diffraction (XRD) marked with X. Scanning electron microscopy energy dispersive X-ray spectroscopy (SEM-EDX) taken from similar locations. Henie Onstad Art Centre Collection. Images: Nasjonalmuseet, Børre Høstland.

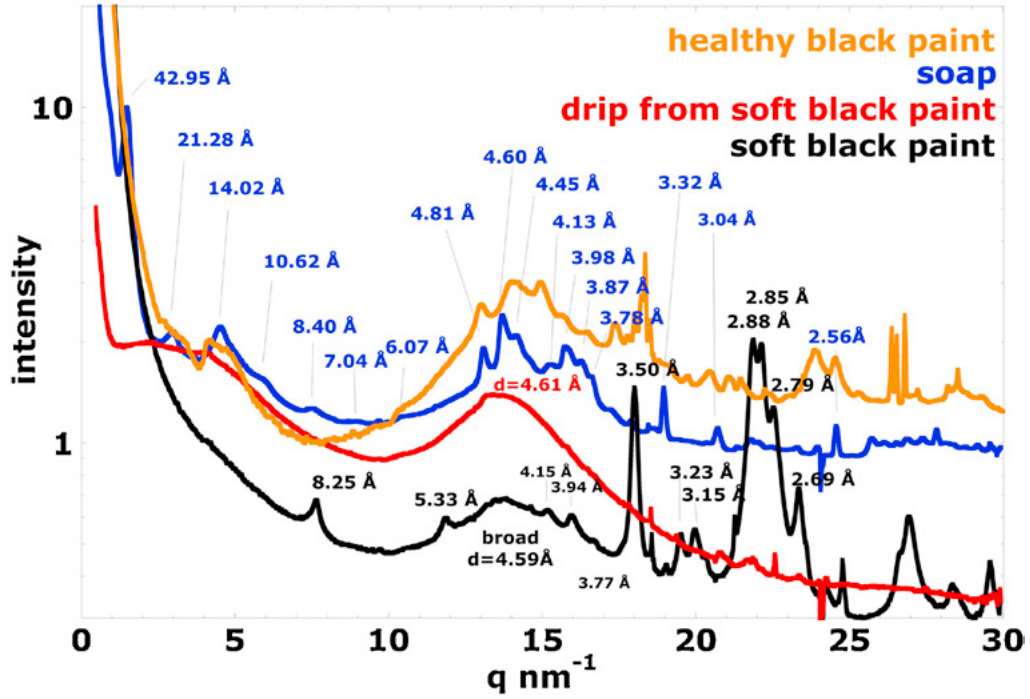

Fig.2. Synchrotron X-ray diffraction (XRD) using the I911 beamline with small angle scattering using a small camera lenght to get the data pattern from paint samples from HOS 00007 Le nu bleu dated 1960 by Karel Appel. Orange: healthy black paint; black: soft black paint; red: drip from soft black paint; and blue: soap. Here, q = 2/d, where d is the d-spacing of the diffraction peak. Image: Robert Corkery.

Funding

This project is funded by Stiftelsen UNI, the Henie Onstad Art Centre and The National museum of Norway.

Publication

Reprinted from publication I.A. Tank Bronken, J.J. Boon, R. Corkery, C.C. Steindal, Changing surface features, weeping and metal soap formation in paintings by Karel Appel and Asger Jorn from 1946–1971, Journal of Cultural Heritage 35, 2019, 279–287 with permission from Elsevier https://doi.org/10.1016/j.culher.2018.09.005

Imaging local electrical properties within single nanostructures

Nanostructures are being developed for future generations of solar cells, displays and electronics. The size of the nanostructures is on the order of ten nanometers, which is about thirty atoms, and this requires very high-resolution techniques for characterization. In electronic and optoelectronic devices, it is very important to be able to study the local electrical properties.

The Science

The advent of nanofocused X-ray beams has allowed the study of strain and composition in single nanocrystals and complete nanoscale devices in a nondestructive manner.

By combining a nanofocused X-ray probe such as NanoMAX with an applied electrical bias as well as electrical current detection, nanodevices can be investigated in more or less realistic operational conditions. In such investigations, the X-rays can be used as a local excitation source generating charge carriers in semiconductor materials with the technique called X-ray beam induced current (XBIC). Conversely, X-rays as a probe can be used to quantify any change in single nanodevices that couple to the crystal lattice using X-ray diffraction (XRD). These methods can be combined, often simultaneously, with scanning transmission X-ray microscopy (STXM) and X-ray fluorescence (XRF), for a multimodal imaging approach.

However, it is technically very challenging to excite and probe currents within single nanostructures. The currents that need to be detected are extremely small, on the order of femtoampere (fA) – equivalent to a flow of only a few thousand electrons per second – which requires very sensitive electronics. The mechanical and thermal stability must also be extremely good. This project has developed a system that makes this possible at the NanoMAX beamline.

The Impact

During the past decade, development in sciences and technologies relies heavily on improving knowledge of materials at the fundamental level. For example, a better understanding of atomic structures and interactions in semiconductor materials significantly enhances the performance of electronic devices. Further development in the field of electronics focuses on promising nanostructured materials, such as nanowires, quantum dots, graphene, etc., which are expected to achieve even better performance. Nanofocused X-ray beams can be used to improve the understanding of these nanostructured materials.

Summary

We designed a special sample holder, compatible with the restricted space at NanoMAX, which was mounted on a piezomotor scanning stage. The standard DIP format makes it possible to use with a wide range of samples. The sample holder is connected to sensitive external electronic equipment, Keysight B2985A, to apply an electrical bias and measure the XBIC. The electronics was connected and operated through the NanoMAX control system (Fig. 1).

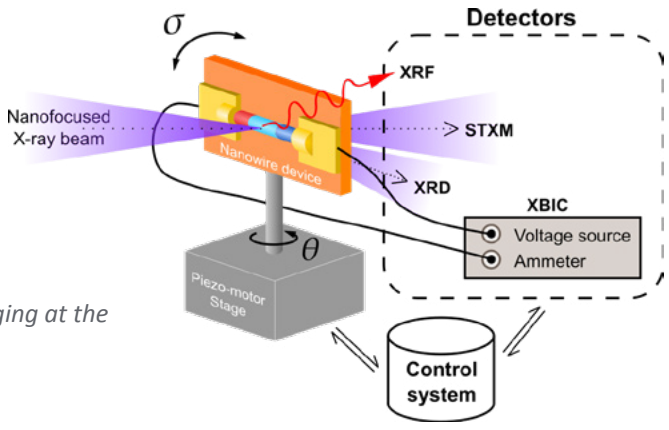

Fig. 1. Measurement system for multimodal X-ray imaging at the NanoMAX beamline.

We first made tests without a sample, which showed a noise floor of about 3 fA (femtoampere). The system was then tested by studying a single contacted p-i-n doped InP nanowire device, which has been developed for the next-generation solar cells at NanoLund, Lund University.

The result from STXM was shown in a differential phase contrast (DPC) image indicating components of the NW device (Fig. 2a). Those components can also be identified using the XRF map because of their different material elements. The blue area on this map is the XRF from indium (In) atoms within the nanowire. The XRF from gold (Au), which can be found in the metal contact, is shown as green areas (Fig. 2b).

The XBIC map sheds light on the underlying carrier collection mechanism of the NW device. The signal is generated in the middle segment (Fig. 2c), approximately corresponding to the depletion region of the solar cells, where there is an electric field to generate a net current. The distribution of the XBIC signal can indicate the effective charge collection area of this nanowire device since the XBIC is proportional to the charge collection efficiency (CCE). At forward bias, which is the relevant operation of solar cells, the XBIC signal reduced, and its area shifted toward n-segment. In contrast, the XBIC signal increased and saturated at reverse bias.

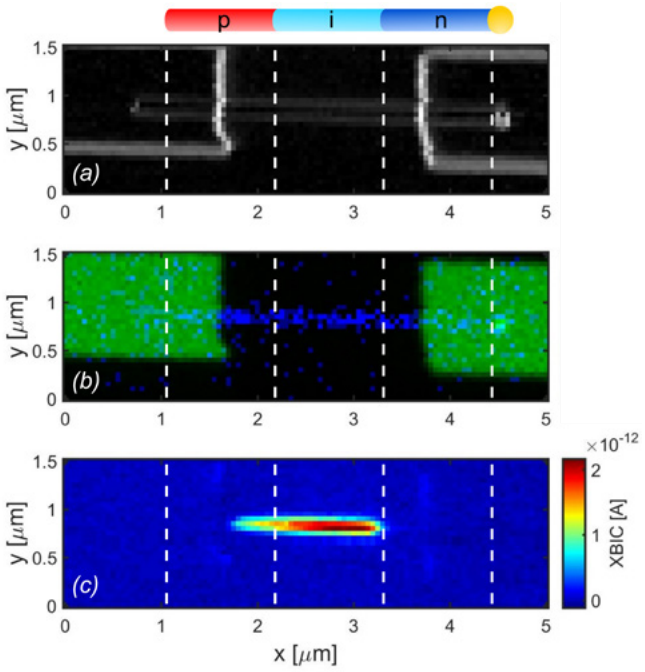

Fig. 2. Multimodal images of a single contacted nanowire device: a) STXM in a differential phase contrast (DPC) mode, b) XRF where blue area is In atoms in the nanowire and green areas are Au atoms in the metal contacts, c) XBIC, which shows that generated charge carriers are collected in the depletion region of the p-i-n junction.

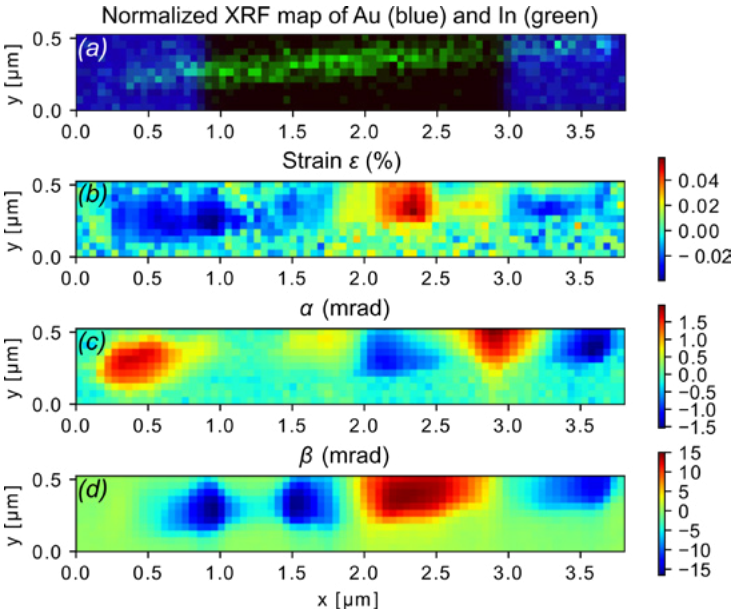

Fig. 3 Strain mapping using scanning XRD: a) XRF map of the nanowire device, as in Fig. 2b, b) strain, c) and d) tilts of the crystal plane around the optical axis and the vertical axis (α, β), respectively.

This variation of the XBIC area is due to an unintentional p-doping in the middle segment revealed by XRF measurement in our previous report.

Finally, the crystal structure of the sample was evaluated by XRD. The XRF map in Fig. 3a was used as a reference for each rotation angle. Reciprocal space mapping using the center of mass of the Bragg peak was used to generate a strain map (Fig. 3b) as well as two tilt maps (Fig. 3c, d), where α and β correspond to the tilt around the optical axis and the tilt around the vertical axis, respectively. The nanowire is strained and strongly tilted, presumably due to stress from the metal contacts. The total range of the strain variation is about 0.1%, but we can distinguish variations on the order of 0.01% (10^{-4}).

Funding

Röntgen-Ångström Cluster, NanoLund, Marie Sklodowska Curie Actions, Cofund, Project INCA 600398, Swedish Research Council grant number 2015-00331, European Research Council (ERC) grant agreement No 801847.

Publication

Chayanun, L., Hammarberg, S., Dierks, H., Otnes, G., Björling, A., Borgström, M.T., Wallentin, J., Combining Nanofocused X-Rays with Electrical Measurements at the NanoMAX Beamline, *Crystals* **2019**, 9(8), 432;
http://doi.org/10.3390/cryst9080432

Properties of copper-based catalyst surfaces

Copper based catalysts could potentially replace more expensive noble metal-based ones. However, a better understanding of the molecular processes on the copper-based catalyst surface is needed. Research performed at beamline HIPPIE gives new insights in the redox properties of two different copper oxide catalyst surfaces.

The Science

Copper and copper oxide-based catalysts show promise for application in several catalytic reactions, such as CO oxidation, the water gas shift reaction, selective oxidation of propylene, methanol dehydrogenation, NO reduction, and photocatalytic water splitting. Efficient noble metal-based catalysts are available for several of these reactions, but scarcity and rising costs make substitution by cheaper and more abundant materials highly attractive. Since copper is both relatively affordable and abundant it constitutes a prime candidate for future replacement of noble metal catalysts.

However, the deactivation of copper-based catalyst through oxidation has hindered its development. Under ambient atmosphere the oxidation of copper proceeds through an initial formation of a thin film of cuprous oxide (Cu2O). Upon further exposure copper will eventually become fully oxidized (CuO). The formation of CuO results in loss of catalytically active Cu+ centers and therefore determines the oxidation and reduction properties of cuprous oxide, critical for the understanding of the deactivation processes of copper catalysts.

The Impact

Intense research efforts are directed toward Cu and Cu_2O based catalysts as they are viewed as potential replacements for noble metal catalysts. However, applications are hampered by deactivation, e.g., through facile complete oxidation to CuO. Despite the importance of the redox processes for Cu_2O catalysts, a molecular level understanding of the deactivation process is still lacking. In order to determine the influence of surface termination and the processes involved in the initial surface oxidation of Cu_2O, single crystals of (100) and (111) terminations were investigated by means of atomic resolution STM and ambient pressure X-ray photoemission spectroscopy (APXPS).

Summary

In the present work we employ in situ XPS and STM to study the redox properties of two facets of Cu_2O, the (100) and the (111) surfaces, under ambient oxygen pressures. The Cu_2O(100) readily hydroxylates by trace impurities in the reaction gas and complete oxidation to CuO occurs already at room temperature. For Cu_2O(111), hydroxylation is not detected on the clean surface and CuO formation only occurs after oxidation at approx. 400 °C in 1 mbar O_2. After CuO is formed, the surface readily hydroxylates at temperatures below 100 °C. These results demonstrate the importance of considering the atomic structure of the terminating surfaces when studying the oxidation and hydroxylation properties.

In the reduction of the hydroxylated CuO phase formed on Cu_2O(100) we observe a gradual removal of hydroxyl groups below 250 °C. The removal of OH groups is directly coupled to additional formation of CuO at the surface through bonding of residual atomic oxygen from the recombinative H_2O desorption process with the substrate.

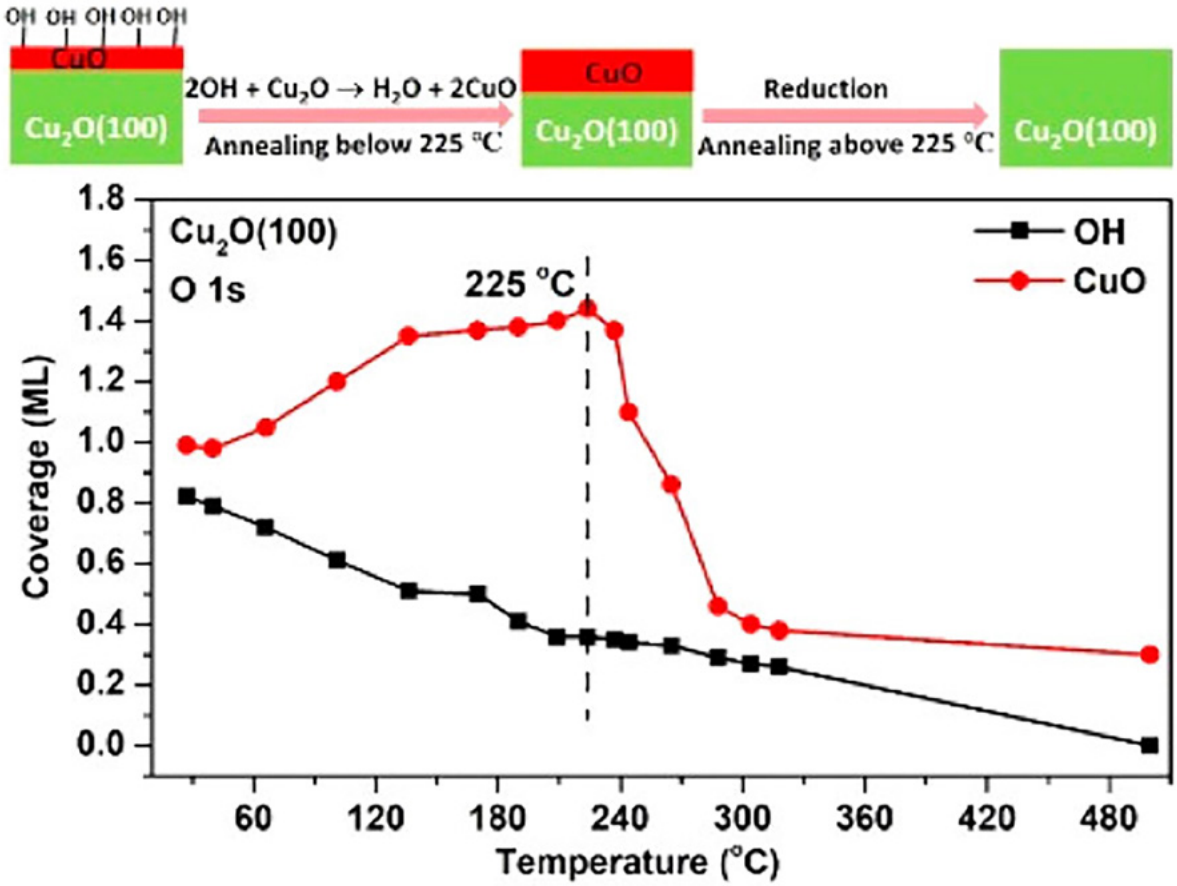

STM was used to correlate the observed changes in surface chemistry with surface morphology, confirming the surface hydroxylation and CuO formation. The STM analysis showed dramatic changes in surface morphology demonstrating a high mobility of the active species under reaction conditions.

This result shows the importance of including corrosion stimulants such as H_2O, which is present under realistic reaction conditions, in the analysis. Above 250 °C a rapid reduction of CuO is observed resulting in formation of a (3,0;1,1) reconstructed $Cu_2O(100)$ at approx. 300 °C. For the reduction of the oxidized Cu2O(111) surface we do not observe OH driven CuO formation. Instead both OH and CuO coverage decrease simultaneously, indicating that both O_2 and H_2O desorption pathways are favourable processes.

Funding

This work was funded by the Swedish Research Council and the Knut and Alice Wallenberg Foundation.

Publication

Reprinted (adapted) with permission from C. Wang, H. Tissot, C. Escudero, V. Pérez-Dieste, D. Stacchiola, and J. Weissenrieder, Redox Properties of Cu2O(100) and (111) Surfaces, *J. Phys. Chem. C* 2018, 122, 50, 28684–28691. Copyright 2018 American Chemical Society. https://pubs.acs.org/doi/10.1021/acs.jpcc.8b08494

Making of a single atom catalyst model system

A novel atomic layer deposition method has been used to synthesise a single atom catalyst system based on iron on a copper oxide support. The system was analysed using X-ray methods as well as microscopy and theoretical calculations. The method used produced an active catalyst for CO oxidation and is promising for further extension to other systems.

The Science

Single-atom catalysts (SACs), with an isolated metal atom anchored on a support, have recently been suggested as a bridge between homogeneous and heterogeneous catalysis.

The objective for growing isolated centers is to combine the benefits of high activity and selectivity in homogeneous catalysts with the advantages in applications by using a heterogeneous catalyst. However, despite a wealth of studies on SACs, including studies on single-atom alloys, atomically dispersed metal oxides, mixed-oxide catalysts, and metal adatoms on single crystals, there is no consensus regarding the nature of the active sites.

Although the SAC seemingly offers a simple system to study reaction mechanisms, the structural complexity of the support hampers analysis at the atomic level. The presence of a reactive gas further complicates the system. The dynamics of the active sites under relevant reaction conditions can only be understood through in situ observations. However, a careful choice of model system may allow for studies of single-site systems by local techniques such as scanning tunneling microscopy (STM), and for well-defined systems with a single-size distribution, laterally integrating techniques such as X-ray photoelectron spectroscopy (XPS) may also provide site specific information.

In the present study, by means of an atomic layer deposition method utilizing the steric hindrance of the ligands, isolated Fe_1O_3 motifs were grown on a single-crystal $Cu_2O(100)$ surface at densities up to 0.21 sites per surface unit cell. Ambient pressure X-ray photoelectron spectroscopy shows a strong metal–support interaction with Fe in a chemical state close to 3+. Results from scanning tunneling microscopy and density functional calculations demonstrate that isolated Fe_1O_3 is exclusively formed and occupies a single site per surface unit cell, coordinating to two oxygen atoms from the Cu_2O lattice and another through abstraction from O_2. The isolated Fe_1O_3 motif is active for CO oxidation at 473 K. The growth method holds promise for extension to other catalytic systems.

The Impact

Single-atom catalysts have recently been subject to considerable attention within applied catalysis. However, complications in the preparation of well-defined single-atom model systems have hampered efforts to determine the reaction mechanisms underpinning the reported activity. We now foresee that the procedures described in this study, using the steric hindrance of the ALD precursor ligands, may be useful in growing single-metal-atom model systems on a wide range of oxide supports.

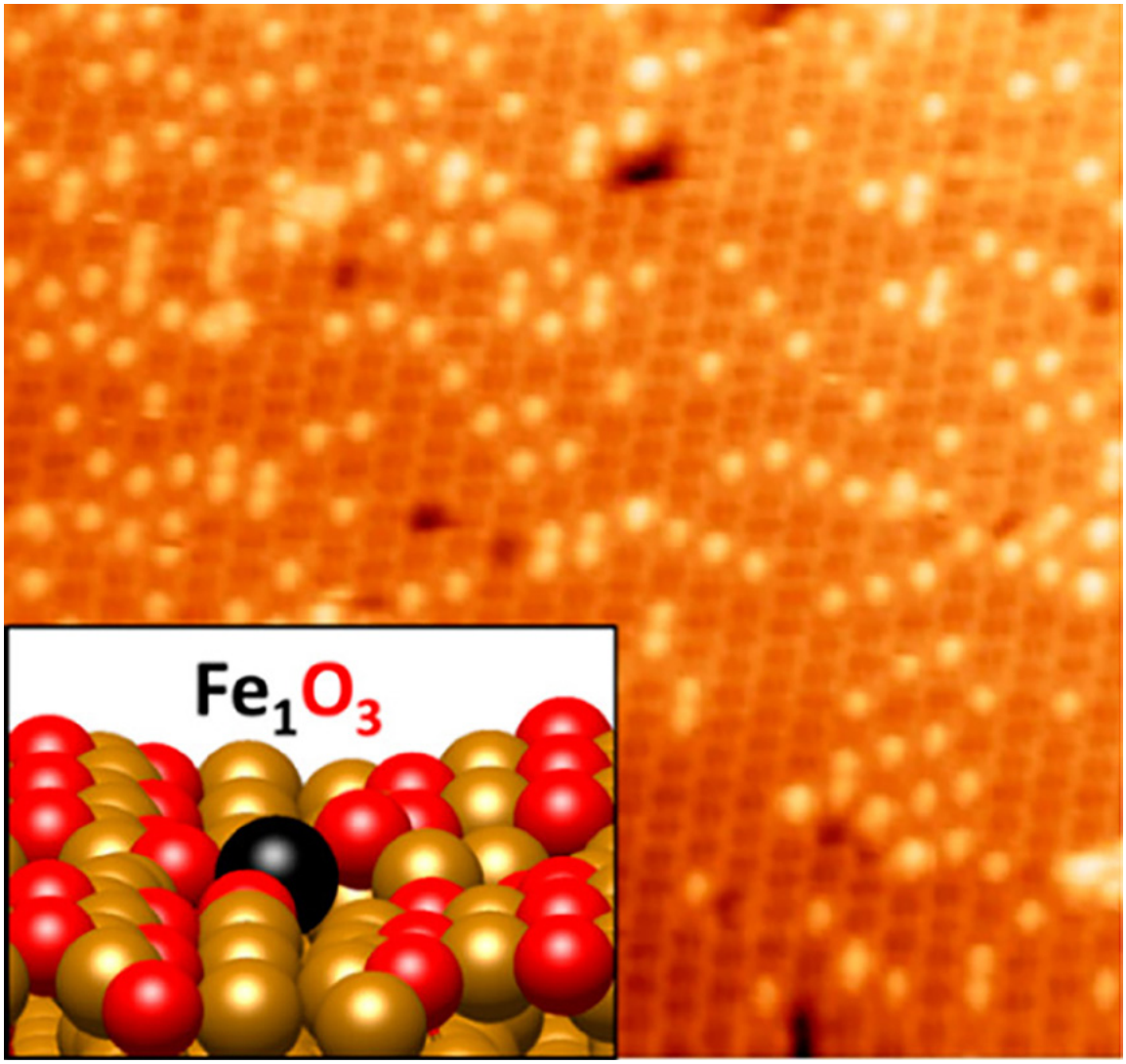

A scanning microscopy image showing the single atom catalyst of iron oxide on a copper oxide surface. Copper atoms are shown in gold, oxygen in red and iron in black.

Summary

A high density of isolated iron atom catalyst with a coverage of approx. 0.21 iron atoms per $Cu_2O(100)$-(3,0;1,1) unit cell was successfully synthesized using a novel ALD method. Steric hindrance of the adsorbed FeCp units facilitates well-separated adsorption sites. XPS results indicate a strong interaction between iron and the $Cu_2O(100)$ surface, and formation of ferric ions renders a stable isolated Fe_1O_3 structure.

An atomic structure with iron coordinating with two oxygen atoms from the $Cu_2O(100)$ lattice and another oxygen atom abstracted from atmospheric O_2 is suggested from the combined analysis by STM, XPS, and DFT. CO oxidation over the model catalyst was investigated by ambient pressure synchrotron-radiation XPS. CO oxidation was only found to occur at 473 K, however with an unfortunate poor stability resulting in the loss of Fe at the surface.

Funding

This work was funded by the Swedish Research Council and the Knut and Alice Wallenberg Foundation. H.T. acknowledges the financial support from the Ragnar Holm foundation, C.W. acknowledges the financial support from Trygger's foundation. S.K. thanks TARLA for the collaborative research afford. J.H.S. acknowledges financial support from the Swedish Nuclear Fuel and Waste management company (SKB).

Publication

Reprinted (adapted) with permission from C. Wang, H. Tissot, J. Halldin Stenlid, S. Kaya, J. Weissenrieder, High-Density Isolated Fe_1O_3 Sites on a Single-Crystal $Cu_2O(100)$ Surface, *J. Phys. Chem Lett.* 2019, 10, 23, 7318-7323. Copyright 2019 American Chemical Society. https://pubs.acs.org/doi/10.1021/acs.jpclett.9b02979

Probing a battery electrolyte drop with ambient pressure photoelectron spectroscopy

To understand and develop rechargeable batteries it is important to be able to probe the surface interaction of the electrodes and the electrolyte. Photoelectron spectroscopy is a powerful method for high resolution surface studies, but usually requires high vacuum. This study performed at beamline SPECIES allows for a liquid electrolyte to be present during Ambient Pressure Photoelectron Spectroscopy measurements.

The Science

Development and implementation of renewable energy sources, together with efficient energy storage solutions are prerequisites for creating a sustainable, fossil fuel-free society. Rechargeable batteries, such as lithium ion batteries (LIBs), currently dominate as portable energy sources in electric vehicles, computers, and mobile phones. Here, it is recognized that the solid-electrolyte interphase (SEI) on the negative electrode plays a vital role for the long-term stability and safety of LIBs, and much research is focused on understanding its formation, composition, and functionality.

Since many crucial reactions in a battery occur at this interface, Photoelectron Spectroscopy (PES) with its surface sensitivity of a few nm and its element and compound sensitivity is one of the most suitable techniques to investigate battery electrodes. The use of high-energy X-rays also allows one to probe the underlying electrode material and its lithiation mechanisms. To date, however, PES has had one severe shortcoming with respect to battery characterization: the need for high vacuum conditions during measurements. Consequently, traditional experimental conditions cannot perfectly mimic the real battery, since they lack the liquid phase.

Luckily, continuous method development has diminished the high vacuum constraint. Today's instruments can measure PES spectra far above the vapor pressure of water, and many other technologically relevant liquids. Ambient pressure photoelectron spectroscopy (APPES) therefore allows one to measure liquid electrolytes and their interactions with the electrode material under more realistic conditions.

The Impact

Operando ambient pressure photoelectron spectroscopy in realistic battery environments is a key development towards probing the functionality of the electrode/electrolyte interface in lithium-ion batteries that is not possible with conventional photoelectron spectroscopy.

Summary

Ambient pressure photoelectron spectroscopy is used to characterize a model electrolyte based on 1M bis(trifluoromethane)sulfonimide lithium salt in propylene carbonate. For the first time, ambient pressure photoelectron spectroscopy data of the electrolyte solvent (propylene carbonate) in the liquid phase is obtained by using the solvent vapor as the stabilizing environment. This choice of ambient conditions leads to a more stable measurement condition for battery electrolyte in APPES. The set of data of the pure solvent is important for analysis of the APPES spectra of the full electrolyte, as it enables the separation of the signals originating from salt and solvent respectively.

The photoelectron spectroscopy characterizations were performed at the SPECIES beamline (MAX II ring). The beamline is equipped with an APPES end station, which allows surface sensitive characterization of solid-liquid interfaces at pressures up to 25 mbar in the energy range of 27–1500 eV. The end station is based on a cell concept, which allows both clean UHV conditions, as well as APPES measurements in a retractable high-pressure cell.

The surface of the electrolyte was characterized using several photon energies, which allows for following changes in electrolyte composition

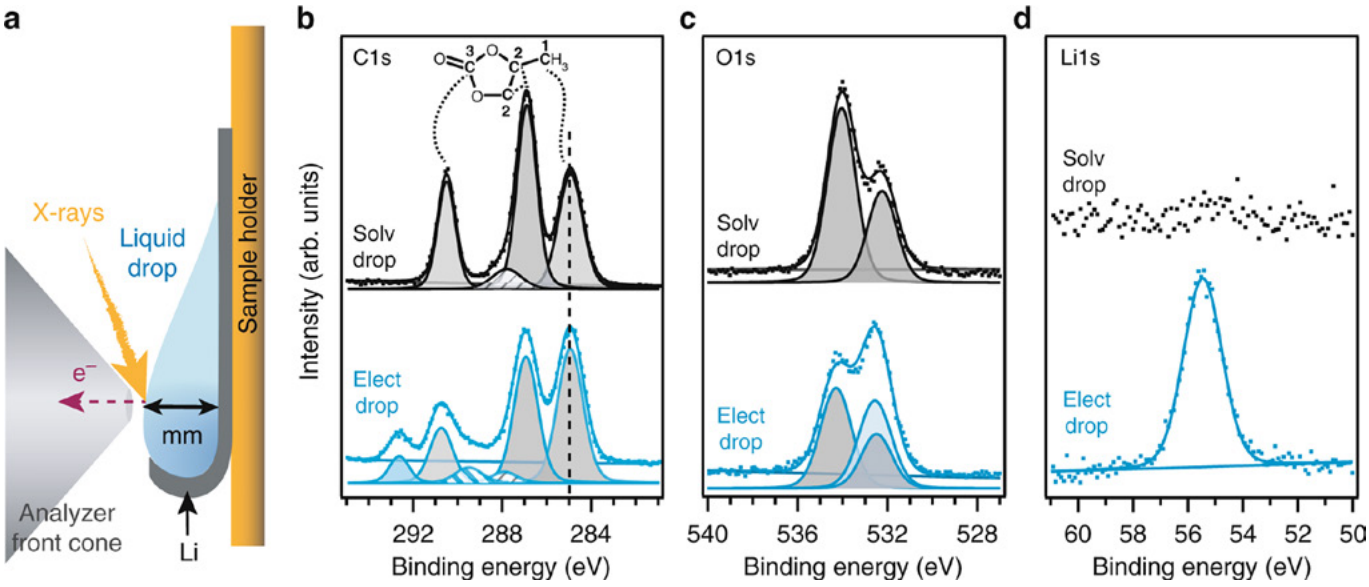

APPES measurements of PC solvent and 1 M LiTFSI in PC electrolyte. Schematic side view representation of the respective liquid droplets on the Li substrate (a). C 1s (b), O 1s (c), and Li 1s (d) PES spectra of Solvent drop (Solv-Drop, top), and Electrolyte drop (Elect-Drop, 1 M LiTFSI in PC, as prepared, bottom)

as a function of probing depth. While the bulk electrolyte meets the expected composition, clear accumulation of ionic species is found at the electrolyte surface.

Recognizing the prospect of future operando APPES measurements, this presents necessary steps in the required methodology development. The results showed that it was possible to measure directly complex liquids such as battery electrolytes, which is an important accomplishment towards true operando studies. From the static droplet experiments, it is concluded that, even without applying any potential to the electrode, adding the liquid phase to the electrode surface increases the complexity of PES studies drastically. A correct interpretation of in-situ and operando APPES battery experiments can only be achieved when we fully understand the behavior of the liquid electrolyte under the given conditions.

Funding

The authors thank for generous sponsoring of this work from the Swedish Research Council (2016-03545, 2012-4681, 2014-6019, 2018-06465), ST and UP for Energy, the Swedish Energy Agency (40495-1), and the Carl Trygger Foundation. In addition, J.M. gratefully acknowledges funding from the German Federal Ministry of Education and Research (FKZ 03XP0131).

Publication

Maibach, J., Källquist, I., Andersson, M. et al. Probing a battery electrolyte drop with ambient pressure photoelectron spectroscopy. *Nat Commun* **10,** 3080 (2019).
https://doi.org/10.1038/s41467-019-10803-y
Open Access

New catalyst for biofuel production

The future of efficient biofuel production from a byproduct of Swedish forestry is within reach. With measurements from the SPECIES beamline a model catalyst has successfully been developed that, once tuned, holds the potential to significantly improve the treatment process for the large-scale manufacture of viable biofuels from the lignin (an organic polymer extracted from a by-product from the pulp and paper industry). Potentially biofuel from lignin can replace 5% of the fossil-based fuel used in Sweden today.

The Science

The catalyst is crucial for making the conversion of lignin to biofuel feasible. The catalyst lowers the amount of energy needed for the reaction to occur, and also makes it possible to steer the reaction to the desired products. Catalytic hydrotreatment processes, which remove oxygen and impurities in the lignin-based feedstock, is vital in the biofuel production.

The Mo-based catalysts have been developed in decades for the petrochemical industry, but have also shown promising results in the biofuel conversion. To tailor the catalyst for lignin-based feedstock, a detailed understanding of the chemical reaction is needed. The catalytic reaction is complex, and to gain insights on the atomistic level into the chemical process, simplified model systems are used.

In our simplified models we have used nanoparticles, which have properties that mimic the industrial catalysts. The nanoparticles were created using a spark discharge method, which is a technique for precisely tuning the properties of the nanoparticles.

The Impact

We have successfully produced model catalyst that can be used to provide detailed information about the catalytic processes that occur in biofuel production. The information is then used by our industrial partners to design and produce new, better catalysts.

However, the catalytic hydrotreatment process has already shown promising results and, within a short time frame, we should be able to fill up our cars with biofuel produced from lignin feedstock. The plan is to make biofuel from lignin commercially available within a couple of years, see Fig 1. To date, most of the research on Mo-based catalysts has been focused on fossil-based feedstocks, and no commercial catalyst specifically developed for biofuel production is available at this time. There are significant differences between renewable and fossil-based feedstock, and by achieving an in-depth knowledge about the catalytic conversion of lignin, the catalysts can be tuned and tailored for a more efficient biofuel production.

Figure 1. Lignin is a byproduct from the pulp and paper industry and can be converted into biofuel, by the use of catalytic hydrotreatment.

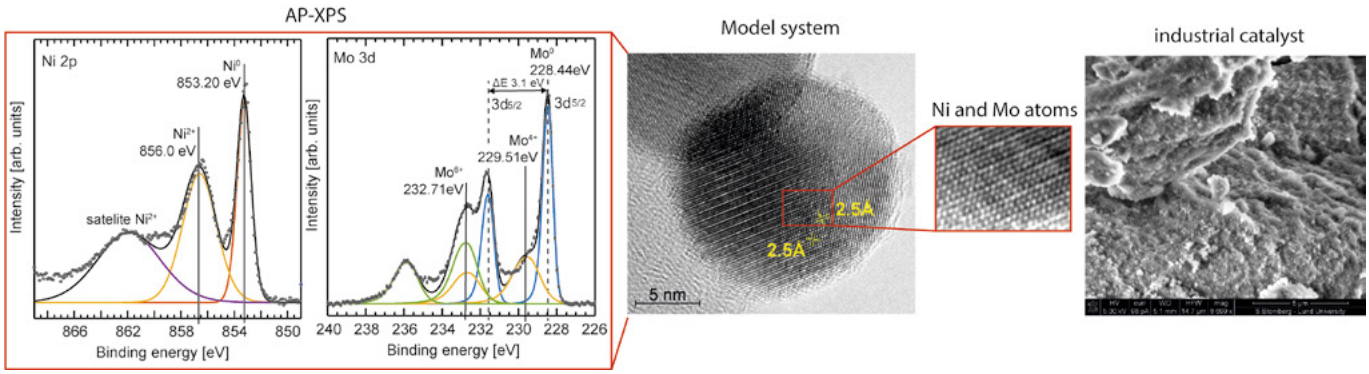

Figure 2. Size-selected bimetallic nanoparticles are used as a simplified model system for the complex industrial catalyst. The nanoparticles are well-defined and studied to achieve detailed knowledge about the catalytic reaction on an atomistic level.

Summary

We have successfully produced bimetallic nanoparticles of nickel-molybdenum (NiMo) with a metallic core and a native oxide shell using a spark discharge method. The technique is both flexible in what material that can be used, and known to produce very clean, size-selected nanoparticles. Our studies revealed that by using this technique, we could tune the Ni and Mo ratio in the nanoparticles in a controlled way. To understand their relevance as model catalysts in the hydrotreating process of lignin, the properties of the nanoparticles have been compared to an industrial NiMo catalyst (NiMo/δ-Al_2O_3).

AP-XPS (Ambient-Pressure Photoelectron Spectroscopy) at the SPECIES beamline has been used to characterize the catalysts in detail. When using AP-XPS the X-rays knock out electrons from the probed material, which carry information about the atoms from which they originate. Because of the very short distance that the electrons travel inside the matter, the technique is extremely surface sensitive, and in the observed signal, it is possible to distinguish if the detected electrons are knocked out from the very first atomic layer or from the atoms in deeper in the bulk. The spectra also reveal chemical information about the surface of the probed catalyst, which is used when the surface interaction with gas molecules is investigated.

The results show that we can produce bimetallic nanoparticles that can be used as a simplified model system for industrial catalysts. In the study, we show that the AP-XPS spectra achieved from the nanoparticles can be used to interpret the results obtained from the industrial catalysts. The results are the first step in the investigation of the biofuel production on an atomistic level and will be used as a platform for future studies where the hydrotreating catalytic reaction is studied using AP-XPS (Fig 2).

Funding

This work has been funded by the Vinnova project *Absorption X-ray Spectroscopy for detailed characterization of NiMo catalysts used for biofuel production* (project nummer 2019-02546) which is a joint project between Lund University, RISE (Research Institutes of Sweden) and SunCarbon.

Publication

S. Blomberg, N. Johansson, E. Kokkonen, J. Rissler, L. Kollberg, C. Preger, S. M. Franzén, M. E. Messing, C. Hulteberg, Bimetallic Nanoparticles as a Model System for an Industrial NiMo Catalyst, *Materials* **2019**, 12, 3727. https://doi.org/10.3390/ma12223727
Open Access

Understanding upconversion particles opens opportunities for better applications

The possibility of tuning chemical and physical properties in nanosized materials has a strong impact on a number of technologies, including photovoltaics, lightning or biomedicine. To understand how dopant concentration, crystallite size, temperature and power density impact such nanosized particles EXAFS at I811 (MAX II ring) was used.

The Science

The up-conversion (UC) phenomenon is a well-known process based on anti-Stokes emission observed in materials doped with luminescent ions. Several factors lead to UC and IR colour changes. Usually, various dopants with emission in whole VIS region are used to change colours.

This paper is focused on the factors that can change the colour of the Yb – Er UC and IR emission. Complex measurements were done in a wide range of temperatures to check the dependence of several factors on Stokes and anti-Stokes emission of the $Lu_2O_3:Er^{3+},Yb^{3+}$ system. It was found that the size of the grains have the highest impact on the spectroscopic properties of the $Lu_2O_3:Er^{3+},Yb^{3+}$. For the smallest particles also Yb/Er concentration ratio, temperature of the measurement and incident laser power have a great impact on both types of the emission colour.

The Impact

Upconversion nanoparticles (UNPs), have evolved as a rapidly growing field and opened up an opportunity for creating new applications in diverse research and commerce fields, such as biological markers, concentrators in photovoltaic cells, markers in security systems, to mention but a few. The use of IR radiation as an excitation source reduces the autofluorescence and scattering of excitation radiation, which leads to the reduction of background in biological experiments. The upconverting nanoparticles offer excellent photostability and are composed of materials that are usually not toxic to organisms.

Summary

This paper investigates the upconversion and IR luminescence properties of $Lu_2O_3:Er^{3+},Yb^{3+}$ under internal (dopant concentration, crystallite size) and external (temperature, power density) factors. Analysing all the results it was found that highest impact of both types of emission have size of the crystallites. Due to large number of defects, high surface to volume ions ratio and surface area small changes in measurement conditions lead to big changes in spectroscopic properties.

All fluctuations of the examined external factors have a significant influence on optical parameters in nanosized $Lu_2O_3:Er^{3+},Yb^{3+}$ therefore it may be utilized in different types of sensors. On the basis of the presented experimental results of Stokes and anti-Stokes emission, it was shown that by modulating Er^{3+}/Yb^{3+} ratio, measurement temperature and excitation power density, it is possible to tune the colour of luminescence.

To obtain materials showing colour shifted to the green a lower concentration of erbium and ytterbium should be used. Also for the smallest grains, an increase in the green emission component that leads to an increase in the GRR ratio, is observed. The temperature and incident laser power should be taken into account during the measurements and analysis of the results, because they have a great influence on the spectroscopic properties of UC materials.

The EXAFS analysis confirms that the increase in concentration of both dopants increases the distance between the Er and the nearest cation. The change in this distance has an impact on the

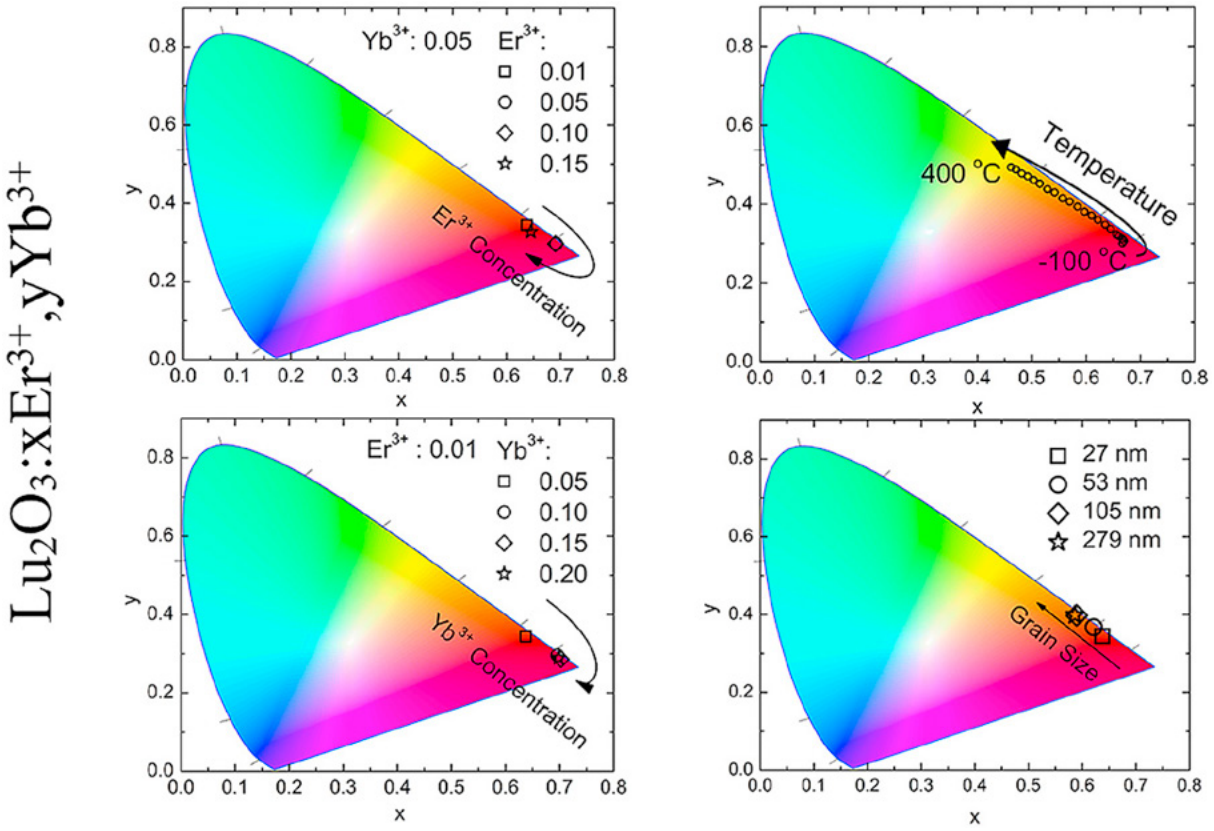

CIE 1931 colour space chromaticity diagrams for the $Lu_2O_3:xEr^{3+},yYb^{3+}$ doped with different concentrations of Er^{3+} (top left) and Yb^{3+} (bottom left).
CIE 1931 colour space chromaticity diagram of Lu_2O_3:1%Er^{3+},5%Yb^{3+} powders as a function of temperature (top right) and with different crystallite sizes (bottom right) and.

GRR ratio in the luminescence. The increase in the Yb^{3+} and Er^{3+} concentrations leads to an increased red component of the emission spectra. The colour of the luminescence may be changed also by the crystallite size of the powder. As the crystallite size increases, the emission becomes orange (higher contribution of the green component). The impact of the temperature on the $Lu_2O_3:Er^{3+},Yb^{3+}$ UC emission was checked in the range from −100 °C to 400 °C. At the lowest temperature, the emission was red and with an increase in the temperature, it becomes green due to the thermal population of the $^2H_{11/2}$ level.

The change of the intensity of the transitions may be utilized in temperature sensing. It can be observed that a decrease in the dopant concentration leads to a sensitivity increase. It was also observed that with the increase in the crystallite size, the sensitivity slightly decreases. The concentration of the dopants as well as the crystallite size have a great impact on the UC order. A higher UC calculated for higher dopant concentration in various temperatures should be considered in terms of the higher probability of the multiphonon nonradiative depopulation of emitting states at higher temperatures. The same effect causes an increase in the UC order for smaller grains. It is also related with the decay measurements where the increase in dopants and the decrease in crystallite sizes lead to decay times shortening. The dopant concentration and crystallite size also have an impact on the Stokes emission where a decrease in the intensity of the $^4S_{3/2} \rightarrow {}^4I_{9/2}$ transition is observed with an increase in dopant concentration (for both ions) and an increase in the crystallite size. This effect suggests that the $^4S_{3/2} \rightarrow {}^4I_{9/2}$ transition is strongly related with the emission from surface ions.

Funding

The research leading to these results has received funding from the European Community Seventh Framework Programme (FP7/2007-2013) CALIPSO under grant agreement noº 312284.

Publication

Reprinted from P. Giuchowski, L. Marciniak, M. Lastusaari, W. Strek, Key factors tuning upconversion and near infrared luminescence in nanosized $Lu_2O_3:Er^{3+},Yb^{3+}$, Journal of Alloys and Compounds, **799**, 2019, 481-494 with permission from Elsevier https://doi.org/10.1016/j.jallcom.2019.05.358

Ionic liquids used as electrolyte in super–capacitors helps store energy more efficiently

Ionic liquids (ILs) are generally defined as molten organic salts with a melting point below 100 °C. These compounds have attracted high interest because of their uncommon physicochemical properties such as low melting temperatures, excellent solvation ability, relatively high thermal stability, low vapor pressure, non-flammability, high electrochemical stability etc. One important application for ionic liquids is as an electrolyte in electrochemical double-layer capacitors (EDLCs), or supercapacitors.

The Science

The three ILs under investigation in the present work are: [$PYR_{1,4}$][TFSI] (1-Butyl-1-methylpyrrolidinium bis(trifluoromethylsulfonyl)imide), [DEME][TFSI] (diethylmethyl (2-methoxyethyl) ammonium bis(trifluoromethylsulfonyl)imide) and [EMIM][TFSI] (1-Ethyl-3-methylimidazolium bis(trifluoromethylsulfonyl)imide) (see structures in Fig. 1.). We use the simplest notation for the ILs, which is based on the cations and anions: [CATION][ANION]. [$PYR_{1,4}$][TFSI] and [DEME][TFSI] are promising ILs for EDLCs, [EMIM][TFSI] has already shown good properties in EDLC, including low cost and high cyclability. Gas phase experiments on ILs are possible, despite the fact that ionic liquids have very low vapor pressures.

In the first approximation, the electrochemical stability window (EW) of ILs is determined by the HOMO and LUMO energies of the ion-pairs they consist of. The upper end of the electrochemical window is usually limited by the oxidation of the anion, and the lower end of the electrochemical window is determined by the reduction of the cation. In the first approximation, the electrochemical stability window (EW) of ILs is determined by the HOMO and LUMO energies of the ion-pairs they consist of. Due to the high importance, we will try to deduce the origin of the HOMO and LUMO states in the vapor of these ionic liquids.

Using similar experimental methods we have previously investigated the valence band photoelectron spectra of simple molecules like CsCl and rubidium halides.

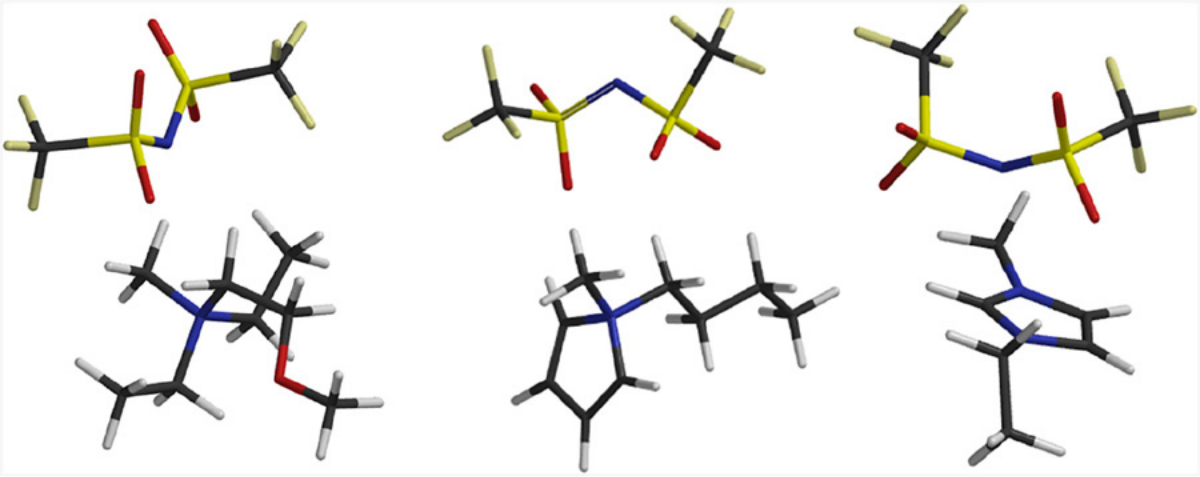

Fig. 1. From left to right: predicted structures of [DEME][TFSI], [PYR1,4][TFSI] and [EMIM][TFSI] gas-phase ion pairs. The different bonds are shown using different colors: gray (hydrogen), black (carbon), blue (nitrogen), red (oxygen), green (fluorine) and yellow (sulfur). The structures have been optimized using the hybrid ωB97X-D functional.

Gas phase experiments on ILs are possible, despite the fact that ionic liquids have very low vapor pressures. We have previously used UPS spectroscopy and ab initio calculations for the study of [EMIM][BF_4] in both vapor and liquid phase and for trimesic acid molecules.

The Impact

To the best of our knowledge, this is the first presentation of the vapor phase UPS spectra of two TFSI based ionic liquids: [DEME][TFSI] and [$PYR_{1,4}$][TFSI]. Liquid phase UPS spectra of these ILs are also not yet available, but there are some theoretical works about [$PYR_{1,4}$][TFSI]. The UPS spectrum of gas-phase [EMIM][TFSI] has already been published by Strasser et al. Their and our independently measured spectra are highly similar, thus confirming their correctness.

The UPS spectrum of liquid [EMIM][TFSI] has already been published by several groups. The liquid and gas-phase spectra of [EMIM][TFSI] are qualitatively highly similar. However, there is quite a substantial shift in binding energy between the corresponding features in the liquid and gas phase spectra. When the comparison between our vapor phase [EMIM][TFSI] UPS spectrum and the liquid phase XPS spectrum of Ikari et al. or Kurisaki et al. is made, the biggest difference is the lack of the inelastic scattering background and less broadening in our gas-phase spectrum

Summary

Gas-phase ion-pairs of [EMIM][TFSI], [DEME][TFSI] and [$PYR_{1,4}$][TFSI] were investigated using valence band photoemission. Although their electronic spectra are similar in their overall shape, the spectral region around 12 eV was sufficiently different. The DFT calculation using the ωB97X-D functional was able to reproduce most of the spectral features. All calculation methods also predict the LUMO to be of cationic origin in all ([DEME|EMIM|$PYR_{1,4}$][TFSI]) ion-pairs. However the HOMO level of all three ILs needs to be discussed separately.

In the case of [DEME][TFSI] all calculation methods agree that the HOMO state of the ion-pair is due to the anion. [DEME][TFSI] is also the most electrochemically stable IL experimentally. [EMIM][TFSI] is electrochemically the least stable of the three ILs studied here and only for this ion-pair the hybrid DFT functionals predict that the HOMO state also involves the π-orbitals of the EMIM cation.

In the case of [$PYR_{1,4}$][TFSI] vapor, the DOS calculated by the hybrid DFT functionals M06 and ωB97X-D agrees with the experimental UPS spectra better than the MP2 calculated DOS.

This seems to validate the hybrid DFT calculation, which predicts that the HOMO of the [$PYR_{1,4}$][TFSI] vapor is due to the TFSI anion. Therefore, all three ILs have a similar low binding energy region (the shoulder to the peak A), thus suggesting initially that the HOMO levels of the ILs are due to the TFSI anion. However, from the calculation results we can add that, in case of [EMIM][TFSI], the HOMO state also involves the cation.

It is also important to point out that the HOMO-LUMO gaps predicted by the hybrid M06 functional are reversed when compared to the experimental electrochemical stabilities. For example, the IL whose ion-pairs have the largest calculated HOMO-LUMO gap ([EMIM][TFSI]) is actually electrochemically the least stable. This seems to verify the claim that the HOMO-LUMO gaps from the calculation should not be blindly used to make conclusions about the anodic or cathodic stabilities.

Therefore, further study of the liquid phase electronic structure and the excited states of the ion-pairs of these ILs is necessary to make final conclusions.

Funding

The authors gratefully acknowledge the financial support by the Estonian Research Council (IUT2-25) and the Estonian Centre of Excellence in Research project “Advanced materials and high-technology devices for sustainable energetics, sensorics and nanoelectronics” TK141 (2014-2020.4.01.15-0011). The research leading to this result has been supported by the project CALIPSOplus under the Grant Agreement 730872 from the EU Framework Programme for Research and Innovation HORIZON 2020.

Publication

Reprinted from I. Kuusik, M. Kook, R. Pärna et al, The electronic structure of ionic liquids based on the TFSI anion: A gas phase UPS and DFT study, Journal of Molecular Liquids **294** (2019) 111580. with permission from Elsevier https://doi.org/10.1016/j.molliq.2019.111580

Investigation of ordering in nanocrystals from renewable materials

Ordering of cellulose nanocrystals as a function of concentration in water was studied at beamline I911-4 at MAX-lab. As convenient alternative to drying the solution on a surface, the experimental method utilizes droplets that levitate in air by acoustic waves. The nanocrystals are interesting as a renewable source for advanced materials in for example photonic applications.

The Science

Assembly of nano-sized building blocks into complex architectures is both a promising route for the fabrication of functional materials and also a design principle in nature. With the significant advances during the last decades in tailoring assembled structures and functionalities of synthetic nanoparticles, there is a rapidly growing interest to utilise nanoparticles from renewable sources in sustainable materials. Nanocellulose is a fibrous nanoparticle that can be readily extracted from wood and other sources (e.g. cotton, ramie and bacteria). Rod-like cellulose nanocrystals (CNC) with a high aspect ratio produced by e.g., sulphuric acid hydrolysis are colloidally stable in aqueous dispersions and form a chiral nematic (cholesteric) liquid crystalline phase at relatively low concentrations.

We have investigated the assembly of sulfonated CNC dispersed in a shrinking levitating aqueous drop using time-resolved small angle X-ray scattering (SAXS). Acoustic levitation of aqueous drops in air is a convenient approach which has been used to study the crystallization and agglomeration of proteins as well as the assembly of nanoparticles. Levitating drops that slowly shrink as the water evaporates constitute a system that does not require the addition of surfactants and allows assembly to be studied without the presence of a solid substrate. The study provides a quantitative tool to study assembly at very high particle concentrations in drops that are sufficien¬tly large to resemble bulk systems, of relevance for fabricating CNC-based photonics.

The Impact

Assembly of bio-based nano-sized particles into complex architectures and morphologies is an area of fundamental interest and technical importance. Nanoscale structural information of CNC assembly up to very high particle concentrations can help to fabricate nanocellulose-based materials by evaporative methods.

Summary

The structural evolution of CNC dispersions during evaporation have been quantified using a substrate-free levitating setup combined with SAXS, covering a very wide concentration range; from 1 vol% up to 38 vol%. SAXS experiments were performed on the beamline I911-4 at MAX-lab.

Analysis of the scaling of the particle separation distance (d) with particle concentration (c) was used to follow the transition of CNC dispersions from an isotropic state at 1–2 vol% to a compressed nematic state at particle concentrations above 30 vol%. Comparison with SAXS measurements on CNC dispersions at near equilibrium conditions shows that evaporation-induced assembly of CNC in large levitating drops is comparable to bulk systems. Colloidal states with d vs. c scalings intermediate between isotropic dispersions and unidirectional compression of the nematic structure could be related to the biphasic region and gelation of CNC.

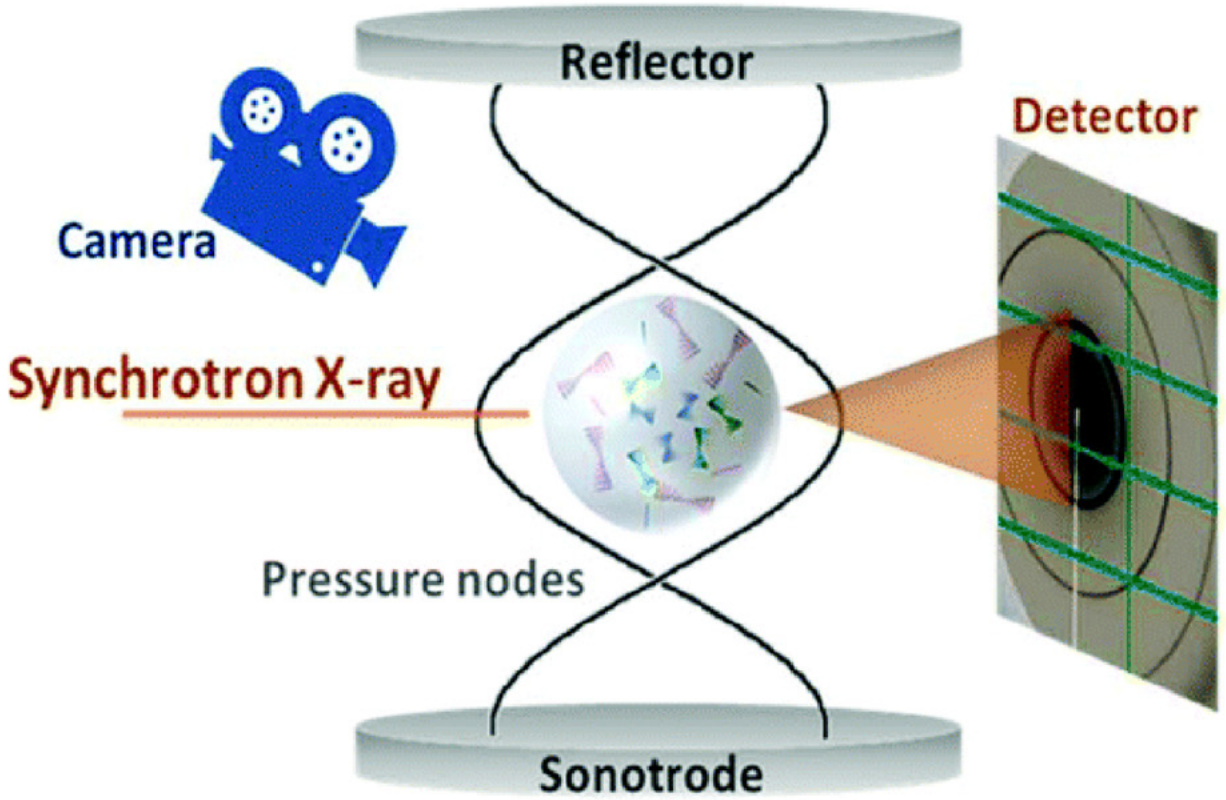

Experimental setup with the droplet suspended by acoustic levitation. The concentration is evaluated from the camera image. The ordering of the nanocrystals is seen by the simultanous SAXS measurement using synchrotron X-rays.

Funding

We acknowledge the Wallenberg Wood Science Center and the Swedish Research Council for funding.

Publication

Y. Liu, M. Agthe, M. Salajková, K. Gordeyeva, V. Guccini, A. Fall, G. Salazar-Alvarez, C. Schütz and L. Bergström, Assembly of cellulose nanocrystals in a levitating drop probed by time-resolved small angle X-ray scattering, *Nanoscale*, 2018, **10**, 18113
https://doi.org/10.1039/C8NR05598J
Open Access

Reassessing the prevalence of topologically non-trivial properties in solid state systems

Realising topological phases in solid state systems is a crucial first step towards the development of applications capable of exploiting the unique properties of electrons populating topologically non-trivial electronic states. The search for systems with topologically non-trivial band structures, and the subsequent drive to understand and exploit them, has thus been among the most dominant areas of research in condensed matter physics for over a decade.

The Science

It all started with the isolation of graphene. The Dirac cones found in graphene's electronic structure are naturally associated with extremely high mobility charge carriers, providing graphene with a lower resistivity than that of elemental metals. Subsequently, topological transitions within electronic band structures were found to drive the existence of spin-polarised Dirac cones at the surfaces of the host compounds, enclosing otherwise insulating materials within a robust, highly conductive outer shell. Although many hosts of Dirac cones have now been found, they belong to scattered subsets of only a few material families.

Through spin- and angle-resolved photoemission (ARPES) and density functional theory (DFT), we establish a set of simple and naturally occurring prerequisites to form ladders of bulk and surface Dirac cones across full families of compounds with otherwise disparate properties and ground states. These 'topological ladders' are formed along a rotationally symmetric axis of the host crystal structure, and entirely within a single-orbital manifold, giving them an inherent robustness against large lattice perturbations. Here we focus on the 1T- and 2H- structured transition metal dichalcogenides (TMDs), which each host as many as five Dirac cones centred at the centre of their surface Brillouin zones.

TMDs are quasi-two-dimensional sheets of MX_2 formula units (M=transition metal, X=chalcogen) separated by van der Waals gaps. This crystal structure provides a natural anisotropy in the energy required for electrons to move within the sheet versus that required to traverse the gaps. For the p-orbital manifold, this natural anisotropy all but guarantees a pair of crossing points along the rotationally symmetric k_z axis of the electronic structure for each the bonding and anti-bonding orbital sets. One crossing point provides a bulk Dirac point (a 3D analogue of those found in graphene), and the second produces a topologically non-trivial (or 'inverted') band gap, enforcing the presence of a Dirac cone at the surface.

The Figure summarises the case of 1T-$PdTe_2$. A highly dispersive antibonding p_z -derived state crosses through the bonding pair of $p_{x,y}$-derived states, producing a tilted bulk Dirac cone and an inverted band gap at $E\text{-}E_F$ = -0.6 and -1.0 eV respectively. A second, larger inverted band gap is produced from the bonding p_z-derived state dispersing from high binding energy and crossing through the lowest of the bonding $p_{x,y}$-derived pair. The DFT slab calculations and ARPES measurements verify the presence of the produced bulk Dirac point and the two surface Dirac cones below the Fermi level. The same mechanism was shown to hold for all five of the other TMDs investigated, including semiconducting 2H-WSe_2 and superconducting 2H-$NbSe_2$.

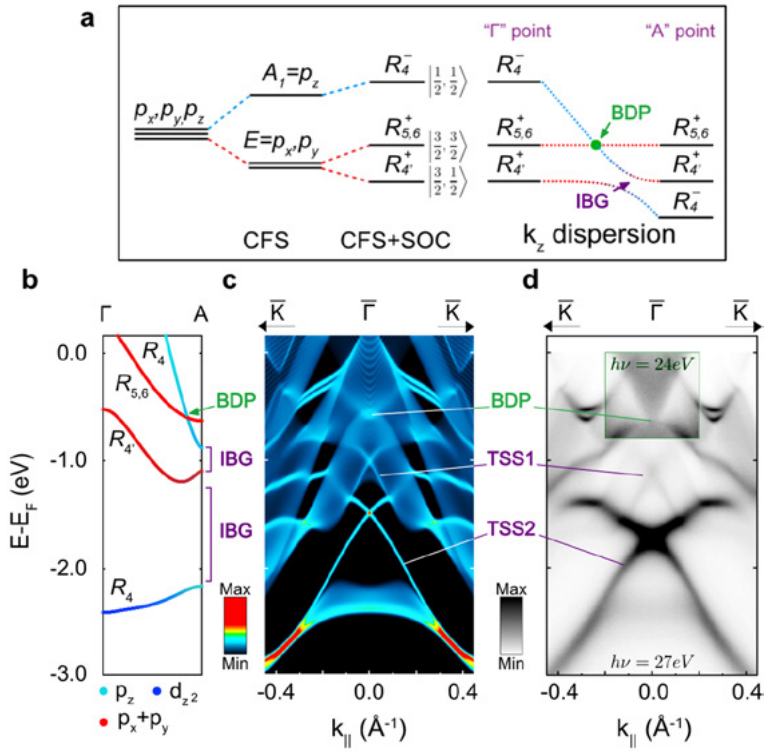

a, Schematic showing the crystal field levels and out-of-plane dispersions which give rise to the topological ladders. b, DFT calculation showing the band structure of $PdTe_2$ along the out-of-plane direction, with the bulk Dirac point (BDP) and inverted band gaps (IBGs) highlighted. The former is evident directly in DFT supercell calculations (c) and ARPES measurements (d), while the later give rise to clearly-resolved topological Dirac surface states (TSSs).

The Impact

The Dirac cone forming mechanism shown in this work is very simple, requiring only a discrepancy in bandwidth along the rotationally symmetric axis of a crystal that is large enough to overcome the splitting of orbital energy levels derived from the combined influence of crystal field and spin-orbit interaction. Topological ladders like the one found in 1T-$PdTe_2$ can therefore be expected to be generic features of band structures in many compounds, even outside of the TMD family. This opens new possibilities for stabilising topological states and phases in combination with a wider array of materials properties than has been possible to achieve to date.

Summary

We find a simple mechanism driving the formation of bulk and surface Dirac cones across full material families and demonstrate its applicability to the transition metal dichalcogenide class. Unlike in the vast majority of examples found to date, the Dirac cones formed via this mechanism are contained entirely within a single-orbital manifold, providing the states with an inherent robustness against large scale perturbations to the underlying bulk band structure. The driving mechanism requires only a disparity in hopping strengths for orbitals along the rotationally symmetric axis of the crystal structure, suggesting a much greater prevalence of topologically non-trivial materials in nature than previously expected.

Funding

This work was supported by The Leverhulme Trust, the Royal Society, the UK EPSRC, JST and JSPS of Japan, Thailand Research Fund, the Research Council of Norway, the NFFA of Italy, and IBS and NRF of Korea.

Publication

Bahramy, M., Clark, O., Yang, B. et al., Ubiquitous formation of bulk Dirac cones and topological surface states from a single orbital manifold in transition-metal dichalcogenides, *Nature Mater* **17**, 21–28 (2018).
https://doi.org/10.1038/nmat5031

Progress in development of a new luminescence setup at the FinEstBeAMS beamline

FinEstBeAMS is a new materials science beamline at the 1.5 GeV storage ring of MAX IV. It has been built based on grazing incidence monochromatization of synchrotron light, which allows to cover a remarkably wide excitation energy range from ultraviolet to soft x-rays (4.5–1450 eV). A new mobile luminescence spectroscopy end station has been commissioned with design benefitting from the advantages of a high flux elliptically polarizing undulator light source.

The Science

The tuneability of synchrotron radiation (SR) in a wide photon energy range and its inherent well-defined time structure makes it particularly well suited for time-resolved luminescence spectroscopy. The history, highlights and future of luminescence spectroscopy at synchrotron facilities have been discussed in several reviews and started with the pioneering work performed at the TANTALUS storage ring in Wisconsin, USA, published in 1970. A high scientific performance has demonstrated an obvious need for dedicated end stations which are specially designed for luminescence studies.

The Impact

Medical applications such as time-of-flight positron emission tomography (TOF-PET) and high luminosity experiments in high energy physics demand novel scintillators, whose characterization requires sub-nanosecond time resolution and high brilliance due to a low intensity of the ultra-fast emissions. The FinEstBeAMS provides a high photon flux in a wide photon energy range, well suited for the studies of the creation and relaxation processes of electronic excitations under excitation in the characteristic energy regions (i.e., valence excitations at the edge of intrinsic absorption, inner shell excitation by high energy photons, etc).

Summary

The Finnish-Estonian Beamline for Atmospheric and Materials Science (FinEstBeAMS) is designed for the studies of the optical and luminescence properties of various types of inorganic solids ranging from classical single crystals to modern nanomaterials and composite compounds.

Its technical configuration allows to study the following characteristics of wide gap materials at temperatures 7-400 K under synchrotron radiation generated by an elliptically polarizing undulator:

i) transmission, reflection and excitation spectra in a wide photon energy range 4.5–1450 eV utilizing a grazing incidence plane grating monochromator for high resolution studies;

ii) polarization and dichroism effects using the ability of the undulator to produce radiation with fully controllable polarization (horizontal, vertical, circular);

iii) emission spectra from UV to NIR spectral range (200–1500 nm); iv) decay kinetics of emission in both standard multi bunch (10 ns interval) and single bunch (320 ns interval) modes of the storage ring.

The beamline contains several end stations installed on the two branch lines. One of these is a compact setup for low temperature luminescence studies, a schematic view of which is presented in Fig. 1. The designed luminescence setup is a mobile end station easily useable at other MAX IV beamlines or operated using external excitation sources. When the luminescence setup is detached, other user-developed experimental stations and instruments can be attached to the FinEstBeAMS beamline instead.

The presented results of the first preliminarily

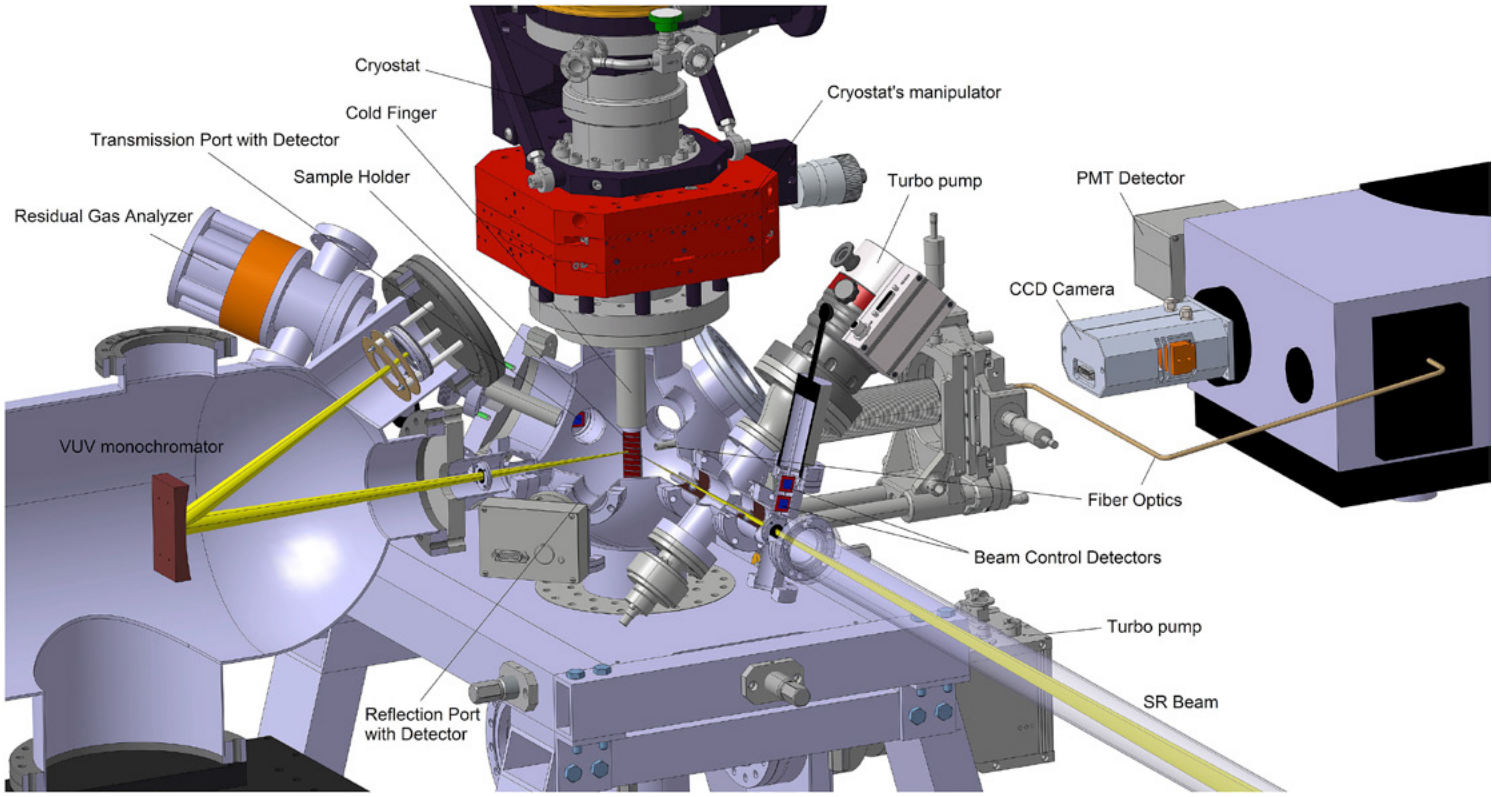

Fig. 1. A scheme of the luminescence setup at the FinEstBeAMS beamline.

commissioning experiments at the FinEstBeAMS beamline, although performed in a relatively small range of excitation energies, demonstrated the high potential of the photoluminescence setup in time-resolved spectroscopic studies of wide gap solids and its ability to attract considerable attention of the scintillator and phosphor research community.

A new sub-nanosecond luminescence registration system is being developed at FinEstBeAMS in a configuration especially suited for the reduced bunch operation mode with 40 ps pulse width and 320 ns interval between bunches. Taking into account the high brilliance of the storage ring this beamline will be especially suitable for the study of fast and weak emissions, which are of great importance for upcoming timing applications.

Further commissioning experiments will determine the weakest phenomena which can be studied. Recently, there has been a strong interest towards an intra-band luminescence, which is due to the transitions between electronic states within the conduction or valence band with a quantum yield of 10^{-4}. So far, the investigations of such weak emissions have been mostly performed using powerful electron beams or lasers. We suppose that, due to the sub-nanosecond time excitation pulses, synchrotrons with high photon flux and free electron lasers can help to reveal the peculiarities of such ultrafast luminescence phenomena.

Funding

The main funding for the FinEstBeAMS beamline has been obtained from the European Union through the European Regional Development Fund (project "Estonian beamline to MAX-IV synchrotron", granted to the University of Tartu) and from the Academy of Finland through the Finnish Research Infrastructure funding projects (FIRI2010, FIRI2013, FIRI2014). The authors also acknowledge the funding contributions of the University of Oulu, University of Turku, Tampere University of Technology, the Estonian Research Council (IUT 2-25, IUT 2-26, PRG-111), as well as the Estonian Centre of Excellence in Research "Advanced materials and high-technology devices for sustainable energetics, sensorics and nanoelectronics" TK141 (2014-2020.4.01.15-0011). The strategic funding of Finnish FIMAX consortium coordinating university, University of Oulu, for beamline personnel is also acknowledged.

Publication

Reprinted in part from V. Pankratov, R. Pärna, M. Kirm, V. Nagirnyi, E. Nõmmiste, S. Omelkov, S. Vielhauer, K. Chernenko, L. Reisberg, P. Turunen, A. Kivimäki, E. Kukk, M. Valden, M. Huttula, Progress in development of a new luminescence setup at the FinEstBeAMS beamline of the MAX IV laboratory, Radiation Measurements **121** (2019) 91-98 with permission from Elsevier
https://doi.org/10.1016/j.radmeas.2018.12.011

CVD Diamond Beam Position Detectors at MAX IV Laboratory

A Diamond XBPM with a four-quadrant single-crystal diamond detector was tested at the NanoMAX beamline at MAX IV. An X-ray nano-beam was used for this experiment with the XBPM placed in the focal plane of the X-ray beam, with a beam size of 62 nm × 61 nm. A precision of the position measurement of 0.6 % of the beam size was demonstrated. This measurement is relevant for applications, where a feedback is used for the position control of the X-ray beams.

The Science

CVD diamond is a radiation resistant solid-state detector material, which is in use in several fields of applications, ranging from beam loss measurements in high-energy physics, in neutron diagnostics for fusion applications, and nowadays for X-ray beam diagnostics, i.e. for position and intensity monitoring at monochromatic experimental beams. Due to the high transparency in combination with ultra-thin gaps in the micrometre range it is a versatile beam monitor for high-precision applications.

The Impact

Measurements with Diamond X-Ray Beam Position Detectors (XBPM) from CIVIDEC Instrumentation XBPM were carried out at MAX IV at the NanoMAX beamline. This was the first investigation of a Diamond XBPM detector with nanometer beams. The position resolution at the smallest available beam size of 60 nm was estimated below 1 nm, which is a precision which was never achieved before.

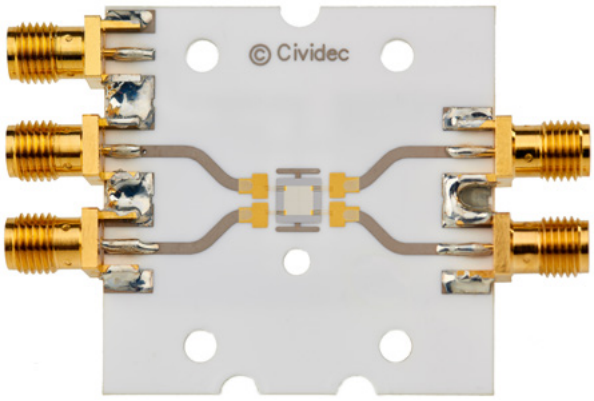

Fig. 1. The sCVD Diamond XBPM Detector.

Summary

Experiments were performed at the NanoMAX beamline at MAX IV with a CIVIDEC Diamond XBPM, as shown in Fig. 1. The single-crystal four-quadrant CVD diamond sensor has a thickness of 20 µm and is metallised with 100 nm titanium electrodes. The four quadrants are separated by 2 µm gaps. The UHV compatible detector has a measurement aperture of 3 mm and a beam pass through 6 mm below.

The NanoMAX beamline [2] provided X-ray beams with a nominal spot size of 70 nm × 70 nm at a photon energy of 13.3 keV. The XBPMs were placed in the focus of the KB optics with a jitter of the piezo positioner of 5 nm.

The detector signals were treated with CIVIDEC C8-Nano electrometer amplifiers and a CIVIDEC readout system. A 1D voltage scan is shown in Fig. 2, where the beam is moved vertically across two quadrants with 25 nm step size. A zoom into 1 µm shows that 25 nm steps are clearly resolvable.

A measurement was performed with the detector centred in the focal plane of the beam with a size of 62 nm × 61 nm. The applied photon energy is 14 keV, and the beam size in the focal plane is 62 nm horizontally and 61 nm vertically. The photon flux in the focus is 7.8×10^{8} photons/s. The nominal detector signal is 1.5 nA and the absorbed power is 2.2×10^{-8} W.

Figure 3 (left) shows individually measured signal currents from two quadrants when the X-ray beam is moved across the face of the detector. The beam position is calculated as ratio of Δ/Σ.

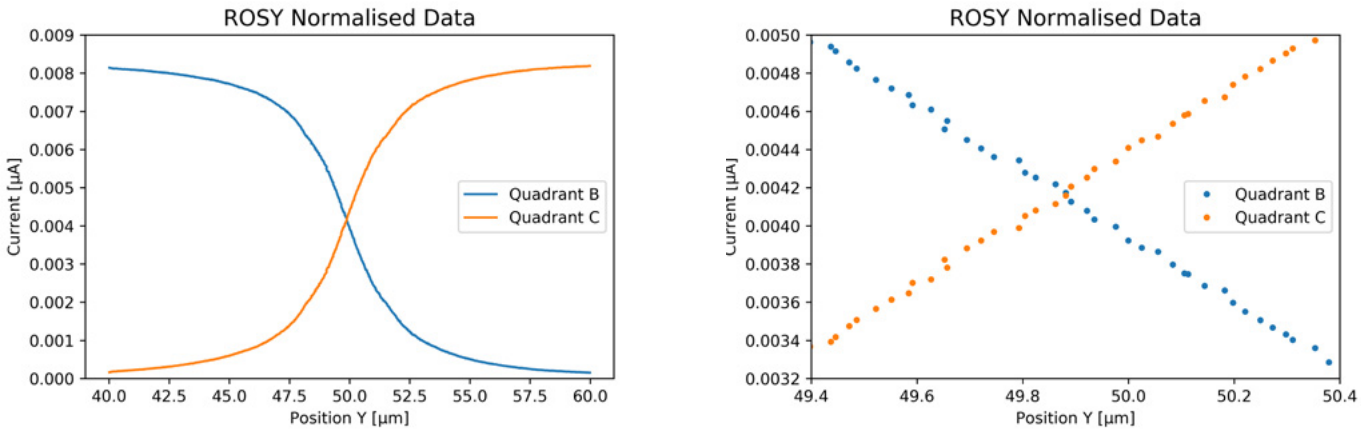

Fig. 2. Vertical 1D scan form quadrant B to C (left), with a zoom of the 25 nm steps (right).

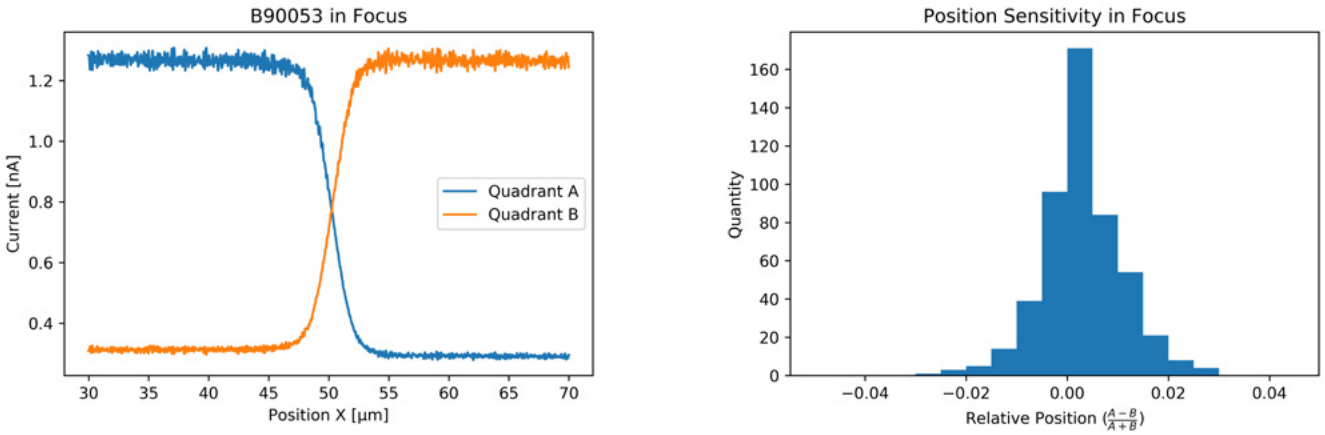

Fig. 3. 1D scan in the focal plane (left). Distribution of position measurement of the centred beam at the Diamond XBPM in the focal plane (right).

When the beam is at a fixed position, the variation of the measurement defines the position resolution relative to the size of the beam. The distribution of the measured beam position is also shown in Figure 3 (right).

The standard deviation of this distribution is 6×10^{-3}, i.e. the beam position can be measured with a precision of 0.6% of the beam size. In this measurement, the beam size is 62 nm, and therefore the precision of the position measurement is 0.37 nm.

The position resolution increases with increasing absorbed power, and from the measurements performed in [1] it is known that it can be improved to better than 1×10^{-3}.

Funding

This project was supported by research funds of CIVIDEC.

Publications

[1] E. Griesmayer, C. Bloomer, P. Kavrigin, C. Weiss, The Use of Single-Crystal CVD Diamond As Position Sensitive X-ray Detector, Proceedings of IBIC2016, Barcelona, Spain, MOPG14, ISBN 978-3-95450-177-9, 2016. https://doi.org/10.18429/JACoW-IBIC2016-MOPG14 Open Access

[2] U. Johansson, U. Vogt, A. Mikkelsen, NanoMAX, A Hard X-ray Nanoprobe Beamline at MAX IV, X-Ray Nanoimaging: Instruments and Methods 2013 Sep. 26 (Vol. 8851, p. 88510L), International Society for Optics and Photonics, 2013. https://doi.org/10.1117/12.2026609

Discoveries map out CRISPR-Cas defence systems in bacteria

Understanding of bacterial immune systems can help us better fight infectious diseases. In this study, it was possible to map and activate an underlying CRISPR-CAS mechanism which bacteria have evolved to defend against invading viruses and other bacteria.

The Science

A cell's adaptive immunity stems from an ability to disable invaders through recognition, targeting, and cleavage of injected foreign DNA and RNA. Structural investigation of the (Sis) Csx1-cOA4 complex of Sulfolobus islandicus has revealed allosteric activation of its ribonuclease activity. This cascade activation is driven by the binding of cyclic oligoadenylate (cOA4), which acts as a second mensseger.

The Type III CRISPR-Cas multi-subunit complex is composed of a trimer of dimers, with each dimer including a cOA4 binding site and a ssRNA catalytic pocket. The cOA4 was observed to undergo a conformational change upon binding in the second messenger binding site activating ssRNA degradation in the catalytic pockets. The binding further catalysed the SiSCsx1 ribonuclease to cleave specific phosphodiester bonds between cytidines. The process is completed with the deactivation of SisCsx1 through cleavage of cOA4 by Ring nucleases.

The Impact

Knowledge of the switch that activates a cell's defence system could be used to diffuse possible attacks from invading genetic material. Reliable control of this process is a step towards understanding the CRISPR-Cas immune system better as well as knowing how to combat bacteria and defend against viruses or potentially, multiple resistance.

Summary

Our research group at the University of Copenhagen analysed how cOA4 influences activation in the Csx1 RNase family of proteins. This was achieved by solving the atomic structures of SisCsx1 in its apo and cOA4 bound forms.

Data was collected from frozen crystals at 100 K with EIGER and PILATUS detectors at beamlines PXI and PXIII at the Swiss Light Source (SLS) in Switzerland, and at BioMAX beamline at MAX IV. Data processing and scaling were accomplished using XDS, POINTLESS and AIMLESS45 as implemented in autoPROC an dthe phase problems was solved using a 4 Å cryoEM map as a model.

Funding

The Novo Nordisk Foundation Center for Protein Research is supported financially by the Novo Nordisk Foundation (grant NNF14CC0001). This work was also supported by the cryo-EM (grant NNF0024386), cryoNET (grant NNF-17SA0030214), and Distinguished Investigator (NNF18OC0055061) grants to G.M., and by National Science Foundation of China (Grant No. 31771380) and the Independent Research Fund Denmark-Natural Sciences (DFF-4181-00274) to Q.S. M.F. was supported by a China Scholarship Council visiting PhD fellowship.

Publication

Molina, R., Stella, S., Feng, M. *et al.* Structure of Csx1-cOA4 complex reveals the basis of RNA decay in Type III-B CRISPR-Cas. *Nat Commun* **10**, 4302 (2019).
https://doi.org/10.1038/s41467-019-12244-z
Open Access

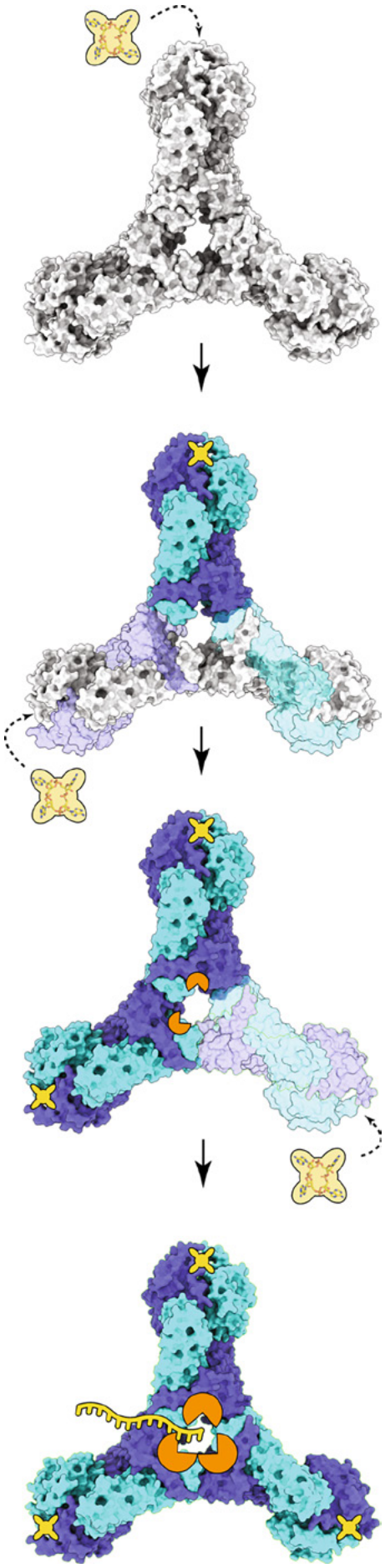

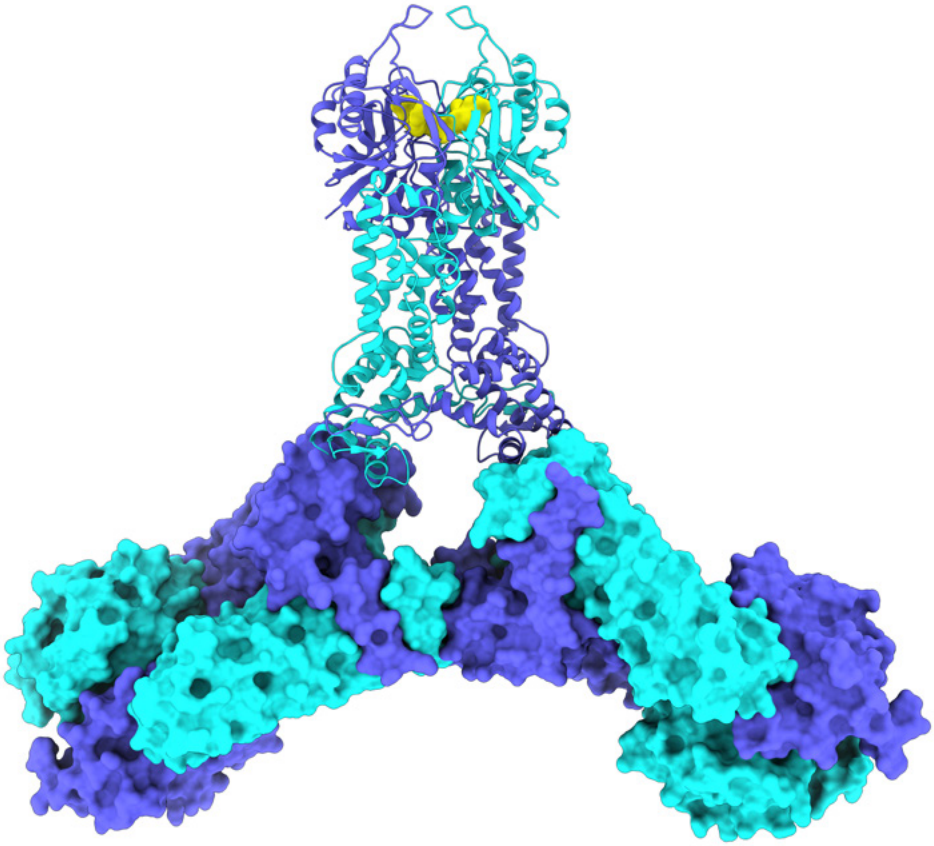

Right Image – Model of the CSX1 protein complex

Left Image – Model for SisCsx1 RNase catalysis activation by cOA4.

The binding of cOA4 (tetralobal shape) by the CARF domains fully activates the first dimer (strong blue and strong sky blue) and induces a conformational change through the HTH to the HEPN domains of two adjacent monomers (light blue and light sky blue) favoring cOA4 binding in any of their available cOA4 binding sites.

The binding of the second cOA4 molecule fully activates the second dimer (strong blue and strong sky blue), promoting some initial RNase activity and triggering conformational changes in the two monomers of the third dimer (light blue and light sky blue) leading to the binding of the third cOA4 molecule and the full RNase activation

Cholera toxin attacks intestinal receptors through secondary binding site

New, lifesaving treatments for cholera will require deeper insight into the mechanisms used by the pathogen *Vibrio cholerae* to attack the human intestines. An important aspect of this work is deciphering how the cholera toxin (CT) binds to host cell receptors. We present evidence elucidating how CT binds through a secondary binding site to fucosylated receptors, histo-blood group antigen Lewis^X (Le^X).

The Science

Many questions remain how the cholera toxin is taken up by human cells. Decades of research describe the binding of CT to primary receptors, through the GMI ganglioside.

Our study is a first to structurally probe the mechanism of CT binding with a different receptor, blood group antigen Lewis^X in non-secretor phenotypes. This phenotype has been found more susceptible to severe disease. It possesses a non-functional Se (FUT2) gene, which results in less fucosylation and an absence of histo-blood group antigens (HBGAs) in bodily secretions.

We show that fucosylated receptors, except fucosyl-GM1, bind solely to a secondary CT binding site. The analysis includes a first CT variant – H18A – with reduced affinity to fucosylated structures, but slightly increased affinity to GM1os. This indicates possible cross-talk between the primary and secondary CT binding sites.

The Impact

Cholera is an acute and severe diarrhoeal disease easily transmitted between humans that, if left untreated, can cause serious dehydration and death within hours. It is a major burden, especially where proper sanitation is lacking, with very high socio-economic costs.

Expanded knowledge of CT binding mechanisms brings us closer to solving how to diminish and eradicate cholera. For example, several groups are actively working on bi-functional polymeric inhibitors to block both toxin binding sites and therefore efficient cell entry, based on our structural results.

Summary

The study explored Lewis^X antigen binding to the secondary binding site of the cholera toxin. To evaluate the CT-ligand interaction, CT receptor binding B subunits were crystallized with the Le^X trisaccharide, L-fucose and the fucosyl-GM1 hexasaccharide (fucosyl-GM1os). Data collection of the crystal structure of CTB complexes with L-fucose or fucosyl-GM1os was performed at the BioMAX beamline, and data collection for the CTB complex with Le^X was done at the ESRF in France.

Le^X and L-fucose occupy the secondary binding sites of the CT, whereas fucosyl-GM1os was found in the primary toxin binding site, binding the CT with the same two-fingered grip as GM1.

Analysis with SPR spectroscopy revealed that Le^X bound more weakly to the CT (CTB and CT holotoxin) than the difucosylated HBGA Le^Y, but still had an affinity typical for many protein-carbohydrate interactions. Several CT variants with mutations in the primary or secondary binding sites were tested. CT variant W88K was chosen to knock out the primary binding site, since Trp88 serves an important role for aromatic stacking interactions with the terminal galactose residue in GM1.

In line with the crystallographic data, primary binding site knock-out hardly affected CT binding to Le^X. In contrast, a mutation in the secondary binding site (H18A) resulted in reduced binding. The toxin variant not only bound more weakly to Le^X, but concomitantly showed enhanced binding to GM1os, suggesting allosteric cross-talk between the two binding sites.

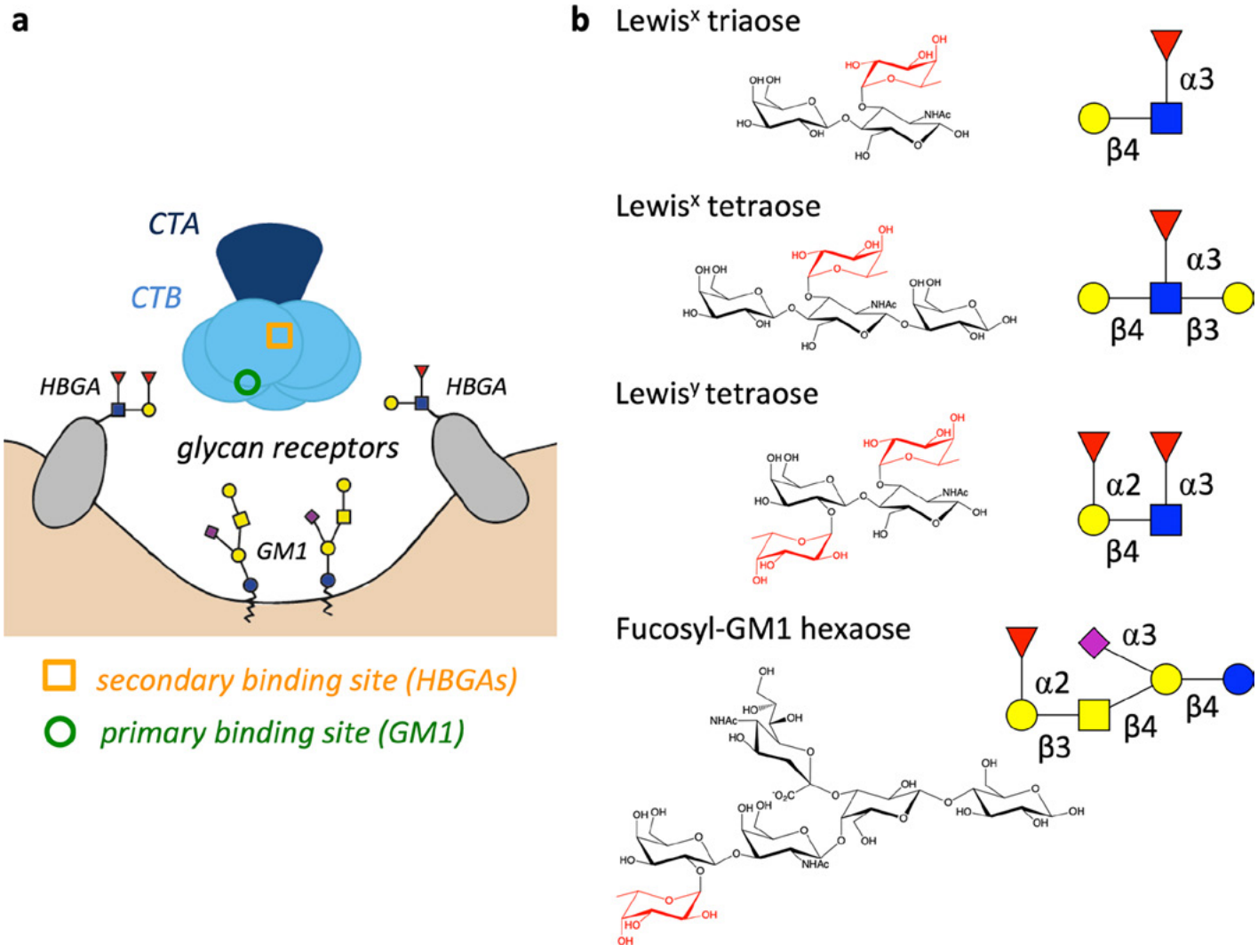

Schematic drawing of CT and its glycan receptors.

(a) Toxin binding to host cell. The AB$_5$ toxin CT consists of one catalytically active A subunit (CTA; dark blue) and a pentamer of the receptor-binding B subunits (CTB; light blue). The toxin's primary and secondary binding sites (for GM1 and HBGAs, respectively) are indicated on one of the five B subunits with a green circle and an orange rectangle, respectively.

(b) Structures of the oligosaccharides Lewis^x triaose and tetraose, Lewis^y tetraose and fucosyl-GM1 hexaose. Fucose residues are highlighted in red. Carbohydrate symbols follow the nomenclature of the Consortium for Functional Glycomics (Nomenclature Committee, Consortium for Functional Glycomics; D-galactose (Gal)–yellow circle, N-acetylgalactosamine (GalNAc)–yellow square, D-glucose (Glc)–blue circle, N-acetylglucosamine (GlcNAc)–blue square, L-fucose (Fuc)–red triangle, N-acetylneuraminic acid (Neu5Ac)–purple filled diamond.

Funding

The University of Oslo and the Norwegian Research Council (Grant 247730). Further support was by iNEXT and the Norwegian Graduate School in Biocatalysis (BioCat).

Publication

Heim, J.B., Hodnik, V., Heggelund, J.E. *et al.* Crystal structures of cholera toxin in complex with fucosylated receptors point to importance of secondary binding site. *Sci Rep* **9**, 12243 (2019). https://doi.org/10.1038/s41598-019-48579-2 Open Access

Exploring the fundamental role of entropy in drug design

The challenges of modern drug design largely involve the ability to interfere with and control molecular recognition or signals, through the binding of synthetic ligands, in a given pathway, with high affinity and specificity for their target proteins. Binding thermodynamics play a fundamental role in these desired outcomes.

The Science

Structural design of ligands by computational means demands knowledge of the molecular conformations as well as the entropic contributions to the free energy of protein-ligand binding. Specifically, we performed a comparative analysis of the protein galectin-3C in complex with two diastereomeric ligands (S and R) to determine the role of entropy in ligand binding.

The Impact

Molecular recognition is fundamental to biology in that it governs signaling within and between cells, with prominent examples provided by the immune system, hormonal control of distant organs in higher organisms, and specificity of enzyme reactions. Modern medicine is to a large extent based on the possibility to interfere with and control molecular recognition by the design of synthetic ligands or effectors that bind to a specific protein in a given signaling pathway. Drug design aims to generate such protein ligands that have high affinity and specificity for the target.

Summary

We have carried out a comparative analysis of ligand binding to galectin-3C using two diastereomeric ligands and a range of experimental techniques combined with computational methods.

This approach has the important advantage that any differences in the thermodynamics of the two binding processes can be related to the bound state, while the contributions from the free states are expected to cancel – as borne out by the present results. Thus, on the basis of this experimental design, we were able to dissect the thermodynamics underlying the difference in ligand affinity.

The two ligands exhibit closely similar free energies of binding, as might be expected for diastereomers. However, the pair exhibits enthalpy–entropy compensation, so that the two complexes still manifest meaningful differences in both binding enthalpy and entropy that we investigated to pinpoint the driving forces underlying the thermodynamic signatures of binding.

Our results highlight an interplay between the protein and solvent degrees of freedom. NMR relaxation experiments and molecular dynamics (MD) simulations show that galectin-3C in complex with S has greater entropy than it has in the R-complex. We also analyzed the MD trajectories to determine the distribution of water molecules around the ligand-binding site, and found that the S-complex has greater solvation entropy than the R-complex, but this entropy difference is smaller than that originating from the protein.

Thus, conformational entropy dominates over solvation entropy in determining the difference in binding entropy between the two stereoisomers.

The combination of high-resolution crystal structures, analyzed by ensemble refinement, NMR relaxation data, and MD simulations enabled us to examine the structural origin of the thermodynamic differences.

Differences in the interactions involving the hydroxyl group at the stereocenter of the diastereomers apparently lead to conformational strain and more pronounced conformational fluctua-

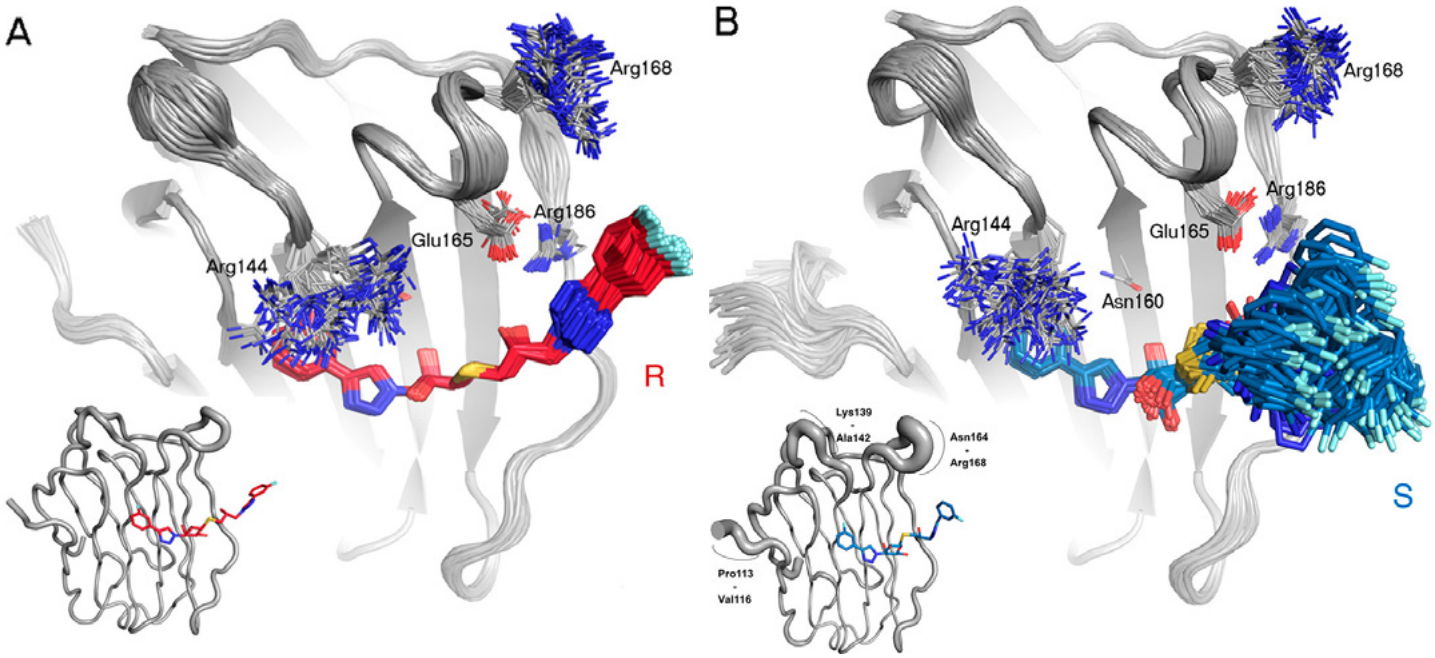

Ensemble refined X-ray crystal structures.

Overlay of the 100 structures with the lowest R_{free} generated by ensemble refinement for (A) R-galectin-3C (red ligand) and (B) S-galectin-3C (blue ligand).
Insets: The protein backbone is displayed as a tube with a diameter corresponding to the ensemble RMS fluctuations for all atoms of that residue (the ligand is shown in its crystal structure conformation).

tions in the S-stereoisomer at the right-hand side of the binding site, which couple with increased fluctuations of the surrounding protein. These results reinforce the notion that structure-based ligand design, when guided solely by static X-ray structures, addresses only one part of the picture and might be misleading.

In a broader perspective, improved knowledge about the sensitive interdependence of solvent entropy and protein conformational entropy adds to our understanding of molecular recognition. The phenomenon indicates both opportunities and challenges in rational drug design. On the one hand, contributions from solvation entropy to the free energy of binding are well-known, and the present results reiterate the concept of targeting individual water sites to achieve increased binding affinity.

On the other hand, efforts to design ligands that perturb the solvent structure around the binding site might not achieve the expected result due to changes in conformational entropy of the ligand and protein, as exemplified herein.

Funding

The Knut and Alice Wallenberg Foundation (KAW 2013.022), the Swedish Research Council (project 2014-5540 to UR), and the European Spallation Source (ERIC; UR and DL)

Publication

M. L. Verteramo, O. Stenström, M. M. Ignjatović, O. Caldararu, M. A. Olsson, F. Manzoni, H. Leffler, E. Oksanen, D. T. Logan, U. J. Nilsson, U. Ryde, and M. Akke. Interplay between Conformational Entropy and Solvation Entropy in Protein–Ligand Binding. *J. Am. Chem. Soc*. 2019, 141, 5, 2012–2026.
https://doi.org/10.1021/jacs.8b11099
Open Access

A novel protein tool for immunity determination in pandemic occurrences

A noble goal of scientific discovery lies in the control of pandemic-calibre diseases. Based on human and animal trials, our investigation found the novel HA tri-stalk protein to be an effective tool to measure immunity levels, and a potential, cost-effective component for a universal influenza vaccine. A focus on elucidation of virus particle surfaces is key to successful vaccine construction.

The Science

With annual epidemics causing 3 to 5 million cases of severe illness and up to 650,000 deaths per year, human influenza virus remains a significant health and economic burden worldwide. The introduction of novel virus variants from the zoonotic pool via antigenic shift can result in viruses capable of initiating future human pandemics similar or beyond the likes of the 1918 influenza, and avian influenza strains such as H5N1, H7N9 and H6N1.

Long alpha helix (LAH) from influenza virus hemagglutinin (HA) stem or stalk domain is one of the most conserved influenza virus antigens. We observed that expression of N-terminally extended LAH in E. coli leads to assembly of α-helical homotrimer which is structurally nearly identical to the corresponding region of post-fusion form of native virus HA. This novel tri-stalk protein was able to differentiate between group 1 and 2 influenza in ELISA with virus-infected mice and human sera. It was also successfully applied for enzyme-linked immunospot assay to estimate the number of HA stem-reactive antibody (Ab)-secreting cells in mice and, with ELISA, determine HA antibodies in a human population with direct occupational contacts to swine.

Our results demonstrate that the novel HA tri-stalk protein, which comprises of the HA LAH region, can be applied in various immunological assays to determine HA stem-specific humoral responses in both clinical and animal samples. The conserved feature of LAH domain makes the HA tri-stalk protein a promising tool for assessment of pre-existing or cross-reactive immunity to a newly emerged influenza viruses.

The Impact

Development of a universal vaccine demands fundamental understanding of how virus particle surfaces function in the viral mechanism. Immunity determination mapped to physiological response to disease is an important step in this work. Applications of the specified HA stem region long alpha helix (LAH) may render the much sought-after universal influenza virus antigen for such a vaccine.

Summary

The tri-stalk protein encoding HA amino acids 403–474 of the pandemic strain A/Luxembourg/43/2009(H1N1) was PCR-amplified and cloned in the pETDuet-1 vector (*Novagen*) using *Nco*I and *Bsp*TI restriction sites. The construct was expressed in *Escherichia coli* BL21 (DE3) cells. For purification of the antigen, the cells were disrupted in lysis buffer A containing 20 mM Tris HCl, pH 8.0, and 100 mM NaCl (6 mL of buffer per 1 g of cells) by sonication. The soluble fraction was isolated by centrifugation. Purified HA tri-stalk protein was crystallized. Datasets were collected at the beamline I911-3 at MAX-lab.

An in-house indirect ELISA was developed using the HA tri-stalk protein as immobilized antigen to evaluate HA stem-specific Ab levels in mice and human sera. In addition, tri-stalk protein was successfully used in an enzyme-linked immunospot (ELISPOT) assay to estimate numbers of HA stem-reactive Ab-secreting cells in mice.

To examine the level of pre-existing antibodies in a human population, our ELISA was used to test a *homo sapiens* sera pool collected in Luxembourg from 211 persons with direct occupational

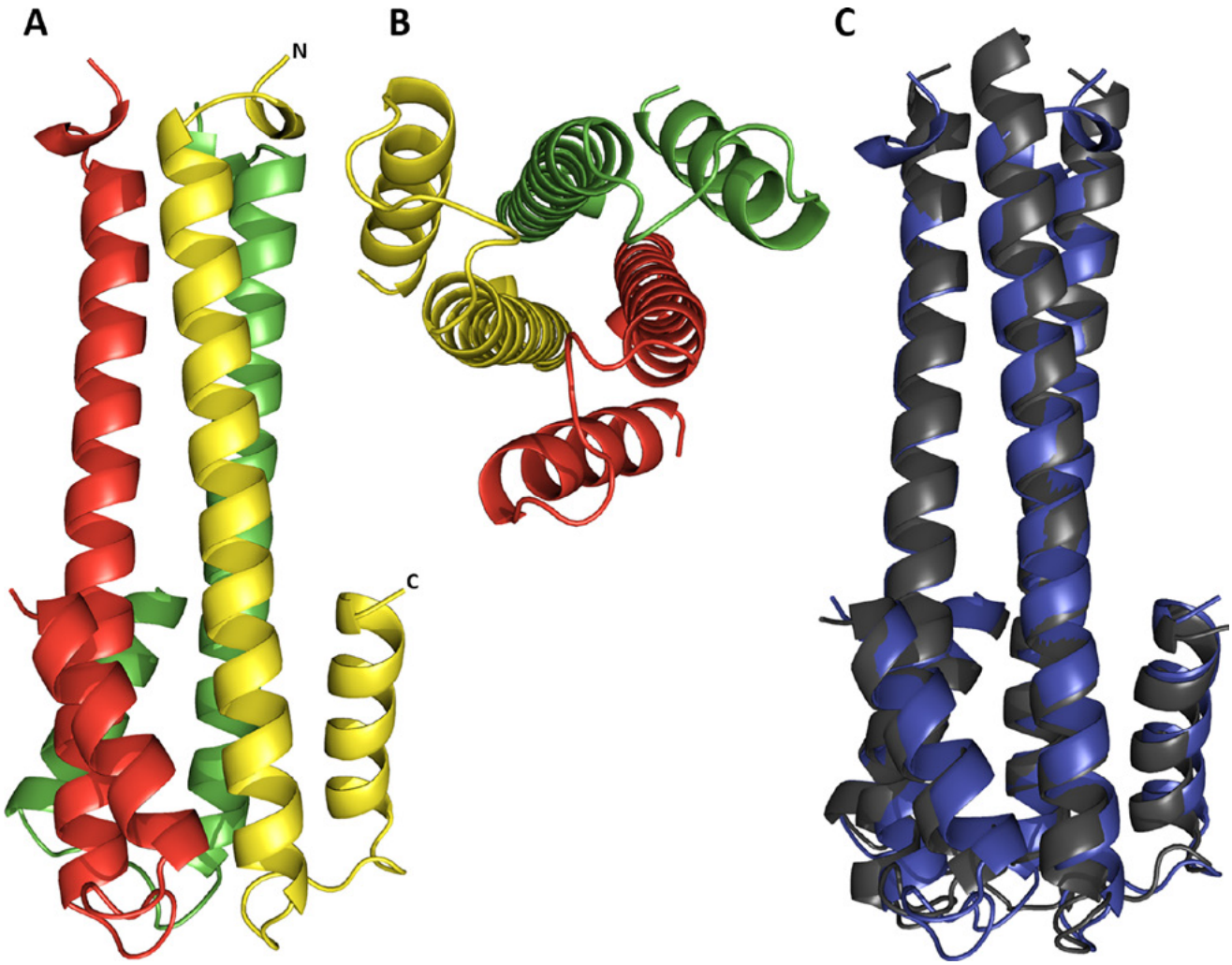

Side (A) and top (B) view on tri-stalk protein. Individual monomers are colored in red, green and yellow. (C) Structural alignment of HA tri-stalk protein (blue) with the corresponding stem fragment of native post-fusion HA (grey) (PDB code 1HTM, residues 63 to 127). Only matching sequence length is shown for clarity.

contacts to swine before the pandemic H1N1/09 virus had spread to Western Europe. Our results show that 70 % of these pre-pandemic sera are positive for group 1 HA stem-specific Abs. In addition, the levels of HA stem-specific Abs have positive correlation with the corresponding IgG titers and neutralizing activities against pandemic H1N1/09 virus.

Funding

The research has received funding from the European Union Seventh Framework Programme for research, technological development and demonstration under grant agreement 602437 (all authors) and from European Regional Development Fund project 1.1.1.1/16/A/054 (AKi, KT and AKa).

Publication

I-N. Lu, A. Kirsteina, S. Farinelle, S. Willieme, K. Tars, C. P. Muller, A. Kazaks, Structure and applications of novel influenza HA tri-stalk protein for evaluation of HA stem-specific immunity, PLoS ONE 13(9): e0204776
https://doi.org/10.1371/journal.pone.0204776
Open Access

In pursuit of an enzymatic dissociation mechanism in cellulose deconstruction

Cellulose is degraded to simple sugars by cellulase enzymes. Strong enzymatic binding is needed to overcome the recalcitrant nature of cellulose, but also leads to unproductive enzyme binding. Their ability to dissociate from the surface to attack new sites limits the degradation rate. Our study compares potential dissociation mechanisms responsible for the limiting action in cellulose degradation.

The Science

Processive enzymes known as cellulases catalyse cellulose deconstruction, accelerating cellulose hydrolysis by more than 17 orders of magnitude, play critical roles in global carbon cycling, and are being harnessed for multiple industrial uses, including biofuel production. Because these enzymes function as biocatalysts, they hold biotechnological interest for use in the nascent lignocellulosic bioeconomy. Cellobiohydrolases (CBHs) are cellulases capable of liberating many sugar molecules in a processive manner without dissociating from the substrate. Within the complete processive cycle of CBHs, dissociation from the cellulose substrate is rate limiting.

This study investigated two plausible mechanisms via Hamiltonian replica exchange molecular dynamics of the model fungal CBH, *Trichoderma reesei* Cel7A. We established the molecular mechanism ''dethreading'' for dissociation from cellulose as the dominant candidate. With this mechanism, the enzyme gradually backs up and slides off the cellulose chain while its substrate-binding tunnel remains closed. A comparative investigation of the "clamshell" mechanism posits that the substrate-enclosing loops open sufficiently to release the cellulose chain without backing up. Computational rate estimates indicate that stepwise cellulose dethreading from the binding tunnel is 4 orders of magnitude faster than a clamshell mechanism, indicating that it is the predominant mechanism in action.

We also present the crystal structure of a disulfide variant that covalently links substrate-enclosing loops on either side of the substrate-binding tunnel, which constitutes a CBH that can only dissociate via stepwise dethreading. Biochemical measurements indicate that this variant has a dissociation rate constant essentially equivalent to the wild type, implying that dethreading is likely the predominant mechanism for dissociation.

The Impact

Knowledge of a dominant mechanism for dissociation may be broadly relevant to processive enzymes of wide-ranging functions and substrates and provides a context for enzyme design efforts. Processive enzymes catalyse modification of many biopolymers, including DNA, RNA, proteins, chitin, and cellulose.

Summary

Dethreading of a cellulose chain from the catalytic domain of *Trichoderma reesei* Cel7A was sampled along 4 discrete steps 1 cellobiose unit at a time as the leading glucose moves between the −1, −3, −5, and finally, −7 states – the last is regarded as dissociated. We also studied the leading glucose transition from the +2 position to the −1, which constitutes partial dethreading immediately after processive motion without hydrolysis. Simulation progress along the reaction coordinate is driven by Hamiltonian replica exchange umbrella sampling (REUS) along a contact collective variable (CV) to ensure sampling along the transition path to compute the free energy.

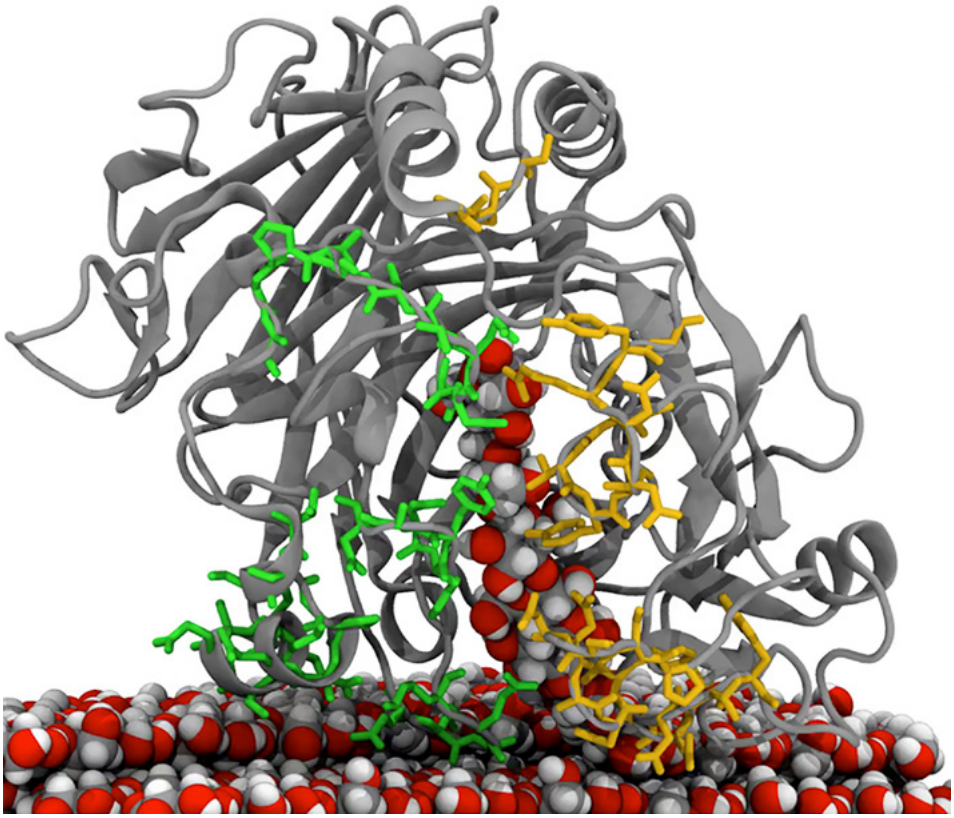

Snapshot from MD simulation of the dissociation of wildtype TrCel7A catalytic domain from a cellulose chain engaged in the active site tunnel. The cellulose is shown in space-filling representation, the protein backbone as cartoon, and residues in loops on opposite sides of the tunnel as sticks. The loops in green are, from top to bottom, A4, A3, A2 and A1, and in yellow B4, B3 and B2.

The system setup for the clamshell mechanism was similar. The 7 reactant-binding sites (−7 through −1) are filled, while the product sites (+1, +2) are empty. This is the state of the enzyme immediately following hydrolysis and product expulsion prior to processivity. The kcat values reported for Cel7A are much higher than koff values suggesting the prevalent complex within the inner processive cycle is a non-productive complex, and therefore, koff reflects the dissociation of the cellulose chain from the substrate- binding sites (−7 through −1). REUS is again used to estimate the free energy profile, although 2 CVs are needed for this mechanism: a quantitative measure of protein–protein contacts across the binding tunnel to describe opening the CBH clamshell structure, and a substrate–enzyme coordinate to describe the exit of the cellulose strand from the Cel7A- binding tunnel.

We utilized equilibrium (5 µs of TrCel7A wild type [WT], 1 µs of TrCel7A variants) and nonequilibrium (101-µs aggregate) molecular dynamics (MD) simulations to directly estimate and compare the dissociation rate constant (koff) for these 2 candidate dissociation mechanisms.

To experimentally test the simulation prediction of dethreading as the dominant CBH dissociation mechanism, we used CBH variant T246C/Y371C (Cel7AS-S), which was designed to introduce a disulfide bond between the tips of loops A3 (Y371C) and B3 (T246C) and thus, effectively abolish the ability of the CBH to open, precluding the clamshell mechanism. X-ray diffraction data for the CBH variant was collected at 100K on beamline I711 at MAX-lab. The crystal structure of Cel7AS-S, refined at 1.64-Å resolution and Rwork/Rfree of 0.13/0.17, unambiguously demonstrates the formation of the disulfide bond between the introduced cysteines

Collectively, our data reveals the molecular mechanism of the rate-limiting step for this critical class of enzymes.

Funding

Funding was received from US DOE, Office of Energy Efficiency and Renewable Energy (EERE), Bioenergy Technologies Office, Estonian Science Foundation Grant PUT1024, Extreme Science and Engineering Discovery Environment, supported by NSF Grant ACI-1548562, via allocation MCB-090159 (to G.T.B.) at the Texas Advanced Computing Center (Stampede2), NREL Computational Sciences Center supported by DOE Office of EERE Contract DE-AC36-08GO28308, and the Early Science program on Eagle.

Publication

J.V. Vermaas, R. Kont, G.T. Beckham, *et al*, The dissociation mechanism of processive cellulases, PNAS, 2019, 116, (46), 23061-23067
https://doi.org/10.1073/pnas.1913398116
Open Access

A MET-targeted antibody engineered to inhibit cancer progression

Aberrant signaling of the Met oncogene is linked to cancer progression. We investigated use of a monovalent anti-Met antibody with a second binding site that recognizes an unrelated, highly expressed antigen on the tumor surface. The MM-131 antibody is monovalent for Met and EpCAM. It strongly inhibits Met signaling in tumor cells by blocking HGF binding and inducing receptor down-regulation.

The Science

MET is an established oncogene that drives tumorigenesis, metastasis, and resistance to therapy. Antibody therapeutics targeting Met have thus far eluded successful clinical development. This study outlines the design and preclinical development of a purely antagonistic anti-Met antibody MM-131 that potently blocks both ligand-dependent and ligand-independent signaling by exploiting the concept of avidity.

MM-131 is a bispecific antibody that is monovalent for Met, but exhibits high avidity by concurrently binding to the tumor-specific antigen EpCAM, and thus exhibits greatest potency in EpCAM-rich cells. Evaluation of Met, EpCAM, and Met ligand, hepatocyte growth factor (HGF) levels in human tumor samples reveals that EpCAM is expressed at high levels in a wide range of Met-positive tumor types, suggesting a broad opportunity for clinical development of MM-131.

Our results show that MM-131 inhibits proliferation in Met-driven cancer cells, inhibits HGF-mediated cell migration, and inhibits tumor growth in HGF-dependent and independent mouse xenograft models.

The Impact

The design of MM-131 provides a solution to the challenges of using monovalent antibodies, which typically lack potency to down-regulate MET, at the same time as it excludes bivalent antibodies known to promote dimerization and activation in MET. Application of clinically-approved MM-131 antibodies may provide a future therapeutic treatment option for cancer patients with MET-amplified, Met-overexpressed, or Met-positive/HGF-positive tumours that also express EpCAM.

Summary

MM-131 was engineered with three components: a monovalent, human anti-Met Fab that binds to the Sema domain of human Met; a stability-engineered IgG1/IgG4 backbone; and a single-chain antibody fragment (scFv) that targets EpCAM.

To generate a bispecific antibody, an asymmetrical Fc region was introduced with knob-into-hole mutations, rendering it heterodimeric. To improve antibody homogeneity, we tested different antibody isotypes for the Fc region (IgG1, IgG4, a hybrid generated by combining the IgG4 CH2 domain with the IgG1 CH3 domain), as well as different hinge sequences (IgG1, IgG4), the addition of a flexible linker (of varying lengths) between the Fc regions, alternative knob-into-hole mutation (Y407T/T366Y), and addition of disulfide bonds. The resultant antibody variants ranged from ~55% to ~90% non-aggregated. Stability assays showed that the IgG1/IgG4 hybrid backbone was more stable. A data set for the peptide-linked Fc was collected at beamline I911-3 of the MAX II ring.

A panel of fully human anti-Met antibodies was generated using a yeast-based antibody display platform and binned by epitope. For the anti-Met portion of MM-131, the selected Fab demonstrated low aggregation properties, high thermal stability, and high expression yields in CHO cells.

We stabilized moc31 onto different antibody

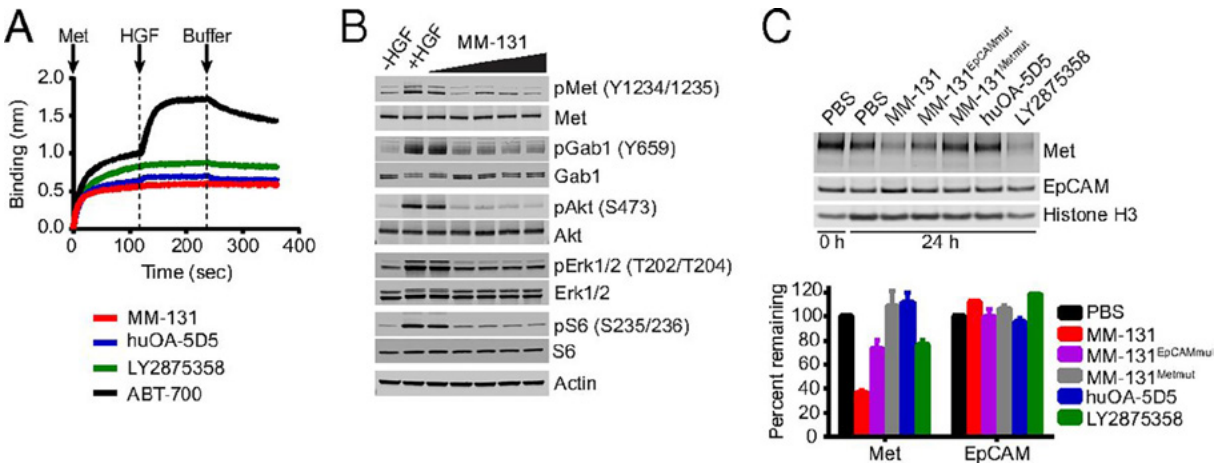

MM-131 inhibits HGF-dependent and HGF-independent Met signaling by antagonizing HGF binding to Met and inducing down-regulation of Met. (A) MM- 131 blocks HGF binding to Met. (B) MM-131 inhibits HGF-induced Met signalling in a dose-dependent manner. C) MM-131 down-regulates total Met levels.

frameworks, tested different orientations of the VH-VL domains, and screened for developability, including the percentage monomer after initial purification. We removed a potential site of deamidation on CDR-L1 to improve homogeneity of the scFv. This change reduced the affinity of the resulting scFv, shifting its equilibrium Kd from ~3 nM to 10 nM.

To assess the effects of MM-131 on downstream signalling, as well as to determine how different levels of Met and EpCAM affect MM-131 activity, we built a mechanistic model of Met signalling comprising ordinary differential equations.

To determine whether the inhibition of Met signalling by MM-131 has phenotypic consequences, we examined the ability of MM-131 to inhibit cancer cell proliferation in cell lines with HGF-dependent or HGF-independent Met activation. Given the role of HGF/Met signalling in tumour invasion and metastasis, we also examined the ability of MM-131 to inhibit HGF-mediated cancer cell migration in a wound-healing assay.

We probed whether antiproliferative activity of MM-131 observed in vitro translates to similar activity in vivo, by evaluating MM-131 in several xenograft models. We examined whether EpCAM targeting is critical for the inhibition of tumour growth by stably knocking down EpCAM in NCI-H441 lung and MKN-45 gastric cancer cells by RNAi (shEpCAM) and evaluated MM-131 in NCI-H441 and MKN-45 shEpCAM and shControl xenografts. Treatment with MM-131 resulted in a marked reduction of tumour growth in shControl xenografts.

Funding

Internal funding

Publication

J.B. Casaletto, M.L. Geddie, A.O. Abu-Yousif, *et al*, MM-131, a bispecific anti-Met/EpCAM mAb, inhibits HGF-dependent and HGF-independent Met signaling through concurrent binding to EpCAM
PNAS, 2019 116 (15) 7533-7542;
https://doi.org/10.1073/pnas.1819085116
Open Access

The key role of resting state for neurotransmitter receptors

Deeper insight into the form and function of major neurotransmitter receptors may open paths of intervention for neurological inhibition. Our study outlines the key role of the resting state in the gating behaviour of alternatively-spliced (i.e. flip/flop) AMPA receptors bound by TARP auxiliary proteins. We elucidate a mechanism whereby motions in the AMPA receptor N-terminal domain are regulated by long-range allosteric control of the flip/flop cassette which is located in the ligand-binding domain.

The Science

Alpha-amino-3-hydroxy-5-methyl-4-isoxazole-propionic acid (AMPA)-type of ionotropic glutamate receptors (iGluRs) mediate most fast-excitatory neurotransmission in the mammalian brain. The receptors are implicated in numerous central nervous system (CNS) disorders. Consequently, greater knowledge of structural and functional aspects of AMPA receptor signalling holds significant value for clinical development.

This study addresses the role of the resting (apo) state in neurotransmitter signalling. We show that nanoscale mobility of resting AMPA receptors predetermines responsiveness to neurotransmitter, allosteric anions and TARP auxiliary subunits. Mobility at rest is regulated by alternative splicing of the flip/flop cassette of the ligand-binding domain, which controls motions in the distant AMPA receptor N-terminal domain (NTD).

Flip variants promote moderate NTD movement, which establishes slower channel desensitization and robust regulation by anions and auxiliary subunits. In contrast, greater NTD mobility imparted by the flop cassette acts as a master switch to override allosteric regulation. In AMPA receptor heteromers, TARP stoichiometry further modifies these actions of the flip/flop cassette generating two functionally distinct classes of partially and fully TARPed receptors typical of cerebellar stellate and Purkinje cells.

The Impact

We demonstrate that the resting state holds a central role in priming the neurotransmitter receptors prior to activation and dictates its responsiveness to channel activators, allosteric modulators, and auxiliary proteins. This may have far-reaching implications for our grasp of the inner workings of many types of signalling proteins, such as other ion channel families, G-protein-coupled receptors (GPCRs), transporters, and kinases.

Summary

We identified a novel allosteric anion-binding pocket at the alternatively spliced flip/flop cassette that modifies NTD motions in the resting state prior to agonist binding and regulates channel gating in the presence and absence of auxiliary subunits. Ser775 of the GluA2flip isoform (GluA2i) renders AMPA receptors sensitive to anion modulation, whereas Asn775 of the GluA2flop isoform (GluA2o) almost eliminates the effects of anions on the NTD and channel gating.

Imaging by atomic force microscopy (AFM) reveals that the NTDs of GluA2o receptors are more mobile than those of GluA2i receptors, indicating differences in the intrinsic conformational flexibility of their resting states. This behaviour is interchangeable via a single amino acid, the Ser775 residue, that operates as a molecular switch between flip and flop isoforms.

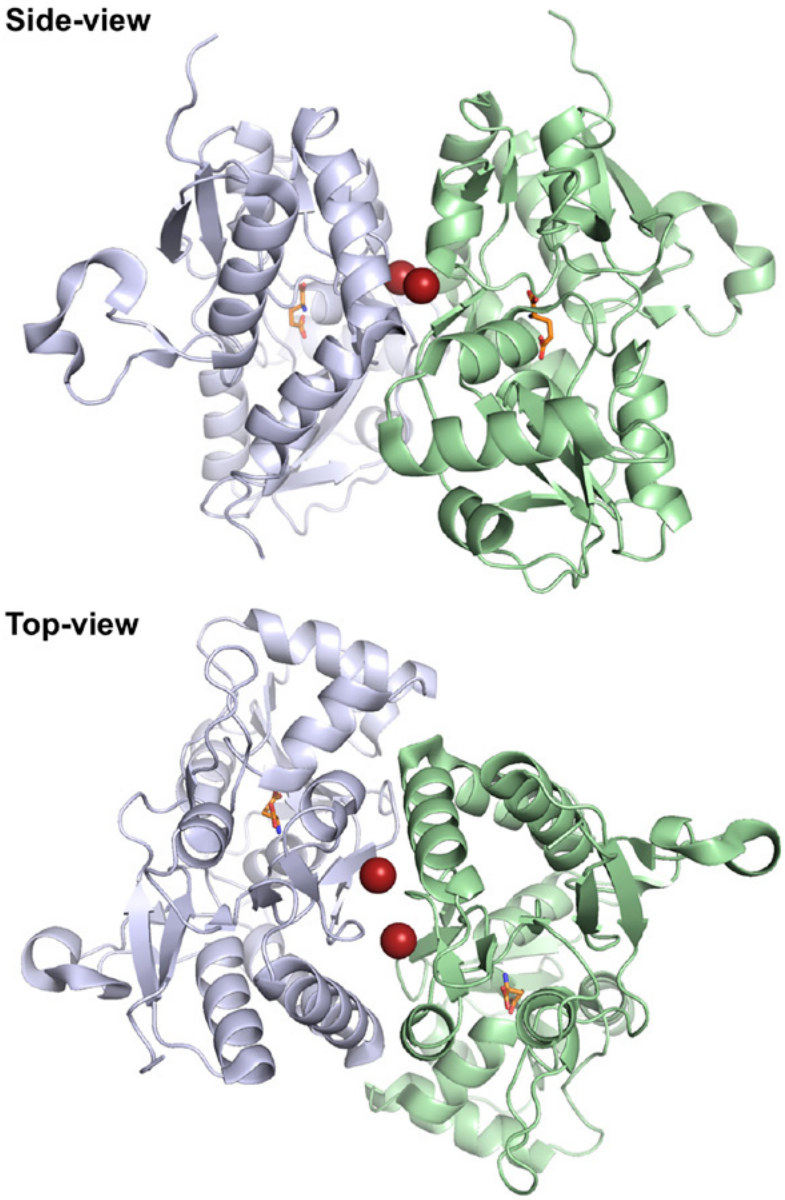

Structure of the ligand-binding domain of GluA2 (flip-like) with glutamate in the binding site and two bromide ions located at the dimer interface. The two GluA2 subunits are shown in cartoon representation in light blue and light green. Glutamate is shown with carbon atoms in orange and the two bromide ions are shown as red spheres. Nitrogen atoms are blue and oxygen red.

TARP stoichiometry further modifies these actions of the flip/flop cassette on AMPA receptor heteromers, generating two distinct classes of partially and fully TARPed GluA1/A2 receptors that match the functional profile of native AMPA receptors expressed by cerebellar stellate and Purkinje cells, respectively.

For investigations of the anion-binding pocket, X-ray diffraction data on GluA2-LBD crystals were collected at the MAX-Lab beamline I911-3 at 100 K.

Funding

This work was funded by operating grants from CIHR, the Lundbeck Foundation, Danscatt, and Biostruct-X, the Biotechnology and Biological Sciences Research Council, and Newton-Picarte grant DPI-20140080, NSERC and FRQS masters fellowships, NSERC doctoral fellowships, scholarship from the Islamic Development Bank, and CONICYT-Chile Cambridge Scholarship.

Publication

Reprinted in part from G.B. Dawe, Md. F. Kadir, R. Venskutonytė, *et al*, Nanoscale Mobility of the Apo State and TARP Stoichiometry Dictate the Gating Behavior of Alternatively Spliced AMPA Receptors, Neuron, 102, 5, 2019, 976-992 with permission from Elsevier
https://doi.org/10.1016/j.neuron.2019.03.046

A potent AMPA receptor potentiator for neurotransmitter signalling

Ionotropic glutamate receptors (iGluRs) such as AMPA receptors play an important role in fast excitatory synaptic transmission. This study presents 7-phenoxy-3,4-dihydro-2*H*-1,2,4-benzothiadiazine 1,1-dioxide as an interesting scaffold to develop new powerful AMPA receptor potentiators, which enhance AMPA receptor signalling.

The Science

Alpha-amino-3-hydroxy-5-methyl-4-isoxazole-propionic acid (AMPA) receptors are considered an attractive target for the discovery of cognitive enhancers and a potential therapeutic tool in the management of Alzheimer's disease. AMPA receptor positive allosteric modulators (AMPA-pams) fine-tune AMPA receptor signals through their binding at allosteric sites of the receptors in the presence of endogenous glutamate.

This study focused on the 7-phenoxy-3,4-dihydro-2*H*-1,2,4-benzothiadiazine 1,1-dioxides, exploring the influence of monosubstitution of the phenoxy group introduced at the 7-position. We developed a synthetic pathway giving access to the preparation of 15 compounds. Particular attention was paid to the study of the binding mode of the new compounds.

We highlight the high potency of compound **11m** via a calcium flux experiment. In vitro activity was found to be the highest in comparison with our previous lead structures. The activity curves obtained for the new compounds shared a much lower Hill coefficient than the curves obtained with reference compounds from our library. Considering this activity profile, attention was thus focused on the characterization of the binding mode of the most active compound **11m** in the series via complementary SAXS, NMR, and crystallography.

The Impact

AMPA receptor positive allosteric modulators increase response or activation of receptors in synaptic signalling. Upregulation of these AMPA receptors could possibly lead to cognition enhancement to combat neurological diseases. The AMPA receptor potentiator **11m** is the first benzothiadiazine dioxide AMPApam to reach the nanomolar range, furthering our knowledge of AMPA receptor biology in neurotransmitter complexes.

Summary

The 7-phenoxy-substituted 3,4-dihydro-2*H*-1,2,4-benzothiadiazine 1,1-dioxides **11** series were synthesized from the corresponding intermediates **10** through a Chan–Lam coupling reaction with the appropriate phenylboronic acid in the presence of copper(II) acetate in dichloromethane.

A set of 15 compounds was evaluated in vitro as AMPA receptor potentiators using a fluorescence-based calcium assay performed on HEK293 cells stably expressing the AMPA receptor GluA2(Q) in order to evaluate the effect of the compounds on the glutamate-evoked channel opening. For each compound, the pEC50 (negative logarithm of the modulator concentration responsible for 50% of the glutamate maximal effect at 1 mM) value was determined.

Exploration of the nature of the substitution of the phenoxy moiety showed that a methyl group seemed to have the same impact on activity as a methoxy group. In the 4-cyclopropyl series, the methoxy group surprisingly exerts a drastic change of the activity profile when positioned in the meta position of the phenoxy moiety (see **11m**, EC_{50} = 2.0 nM vs **11j**, EC_{50} = 46.1 nM). This led to the most powerful AMPA receptor potentiator ever

designed in our series, namely compound **11m**.

SAXS data first corroborated the high affinity of **11m** and confirmed that this compound occupies only one site per dimer interface, contrary to most benzothiadiazine dioxides developed as AMPA receptor potentiators. Crystal structure determination of the ligand-binding domain of GluA2 (GluA2-LBD) in complex with glutamate and **11m** confirmed that only one molecule of **11m** binds at the dimer interface. The structure was determined at 2.00 Å resolution. Compound **11m** primarily occupies subsites A and C. The binding mode of the highly potent compound **11m** was analysed, and especially how the larger substituent in the 7-position is located in the binding site. Results obtained with NMR spectroscopy were found to be consistent with the X-ray and SAXS data.

From these observations, compound **11m** behaves as two molecules of the reference compound **5**, since **11m** is able to recreate the interaction observed after two molecules of compound **5** binds into the allosteric pocket. Altogether, the data confirmed that compound **11m** belongs to a singular subclass of the benzothiadiazine dioxides developed so far.

In addition, the GluA2-LBD-L504Y–N775S was crystallized with the reference compound **3**. The structure was determined at 1.78 Å resolution. The binding mode of compound **3** was characterized using SAXS and crystallography. Compound **3** binds in two copies per dimer interface and occupies subsites C within the allosteric pocket. A chlorine–fluorine interaction between the two neighbouring molecules was found. X-ray diffraction data was collected at beamline I911–3 at MAX-lab at a cryogenic temperature (100 K).

Funding

This work was funded by the Fonds pour la Recherche Scientifique (F.R.S.-FNRS) Incentive Grant for Scientific Research [F.4510.14], Fonds Leon Fredericq, University of Liège [Fonds Speciaux], Lundbeck Foundation, Danish Council for Independent Research, Novo Nordisk Foundation, GluTarget, Danscatt, CoNeXT, BioStruct-X, and NIH (NS085239 and GM068935). CHESS is supported by the NSF and NIH/NIGMS via the NSF award DMR-1332208, and the MacChess resource is supported by the NIGMS award GM-103485.

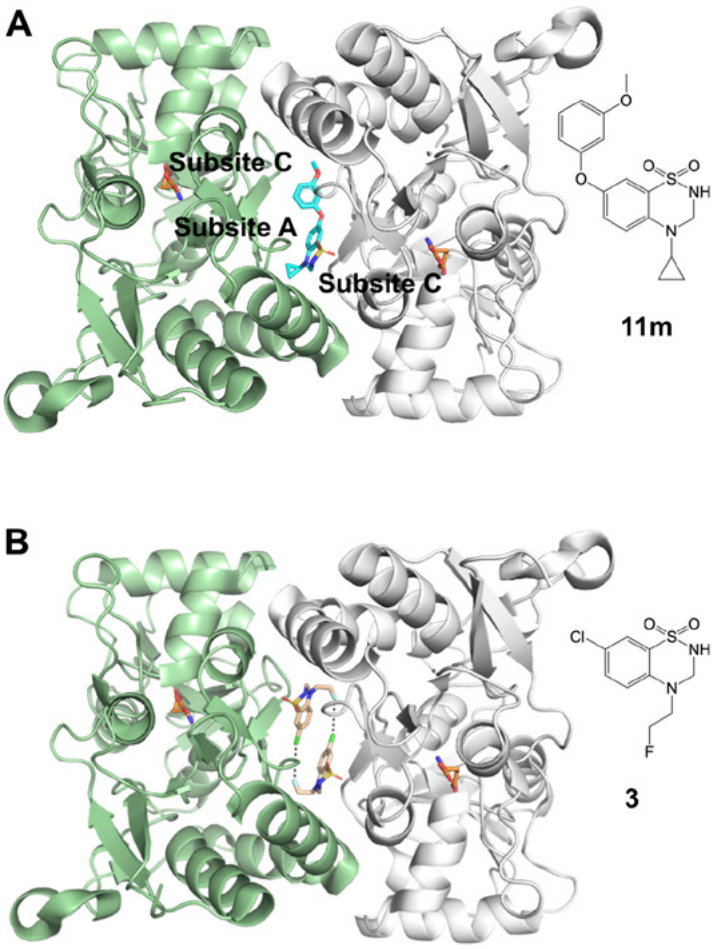

Structures of GluA2-LBD in complex with glutamate and the AMPA receptor potentiator **11m** *and* **3**, *respectively. (A) Cartoon representation of the GluA2-LBD dimer (chain A in green and chain B in grey) with glutamate shown with carbon atoms in orange and* **11m** *with carbon atoms in cyan. (B) Cartoon representation of the GluA2-LBD dimer with glutamate and* **3** *(carbon atoms in beige). Black dashed lines illustrate chlorine-fluorine interactions. Nitrogen atoms are blue, oxygen red, and sulfur yellow.*

Publication

Reprinted in part with permission from Goffin E., Drapier T., Larsen A.P., *et al*, 7-Phenoxy-Substituted 3,4-Dihydro-2H-1,2,4 benzothiadiazine 1,1-Dioxides as Positive Allosteric Modulators of alpha-Amino-3-hydroxy-5-methyl-4-isoxazolepropionic Acid (AMPA) Receptors with Nanomolar Potency, *J. Med. Chem*. 2018, 61, 1, (251–264) Copyright 2018 American Chemical Society
https://doi.org/10.1021/acs.jmedchem.7b01323

A design tool for high specificity in glutamate receptor ligands

Glutamate (Glu) is a major neurotransmitter linked to certain CNS disorders. Glu is mediated by G protein-coupled metabotropic receptors and ionotropic receptors (iGluRs). This study provides insight into factors determining selectivity among iGluRs and identifies the hydroxy-1,2,3-triazole moiety as a novel tool for development of ligands with specificity for singular iGluR subtypes.

The Science

iGluRs are ligand-gated ion channels that are divided into three major classes according to amino acid sequence identity and to their respective activation by the agonists N-methyl-D-aspartic acid (NMDA), (S)-2-amino-3-(3- hydroxy-5-methyl-isoxazol-4-yl)propionic acid ((S)-AMPA, 2), and kainic acid (kainate, KA). Large number of ligands showing selectivity among the three classes of iGluRs have been disclosed, but few ligands have been developed with specificity for the individual receptor subtypes within the classes, presumably due to high sequence identity among the subunits within each class.

To explore the selectivity toward iGluRs, we use a hydroxy-1,2,3-triazole scaffold to bioisosterically replace the distal carboxylic group of glutamate. We describe the synthesis and extensive pharmacological characterization at native and recombinant iGluRs of the Glu analogues 6a–c and 7a–c and the aspartate analogue 8 along with X-ray crystallographic studies of compounds 6b and 7a bound in the GluA2-ABD.

The Impact

This new series of glutamate and aspartate analogues build on the availability of ligands highly specific for individual iGluR receptors, a key receptor type for the neurotransmitter, glutamate. Our observations demonstrate specific, novel features that arise when employing a hydroxytriazole moiety as a bioisostere for the distal carboxylic acid in glutamate receptor agonists.

Summary

Four analogues showed selectivity among AMPA receptors, most pronounced with compound 6b that shows moderate binding affinity toward GluA2 but an order of magnitude lower affinity toward GluA1 and GluA4. This selectivity profile is not mediated by differences in amino acid residues in direct contact with the ligand. The only sequence difference in the orthosteric site that mediates the selectivity of Cl-HIBO is a tyrosine in GluA1/2 that is a phenylalanine in GluA3/4.

The X-ray structure of 6b in GluA2-ABD shows a weak electron density for Met729 in GluA2, indicating that 6b binding results in increased flexibility of this residue in GluA2-ABD compared to other ligands for which crystal structures exist. This could reduce the entropic cost of binding to GluA2-ABD and thereby explain the higher affinity toward GluA2-ABD compared to other subtypes. The structure of 7a shows that substituents larger than a methyl group cannot be accommodated, which is in line with the observed lack of activity of compounds 7b and 7c. X-ray data of the GluA2-ABD in complex with 6b and 7a was collected at BioMAX beamline at MAX IV laboratory in Lund, Sweden, at a wavelength of 0.9800 Å.

The use of the hydroxy-1,2,3-triazole in aspartate analogues leads to compound 8, which shows activity among NMDA receptor subtypes. Most notable is the ability of compound 8 to activate both the GluN1 and GluN2 subunits that harbour the Gly and Glu binding sites, respectively, of the NMDA receptor.

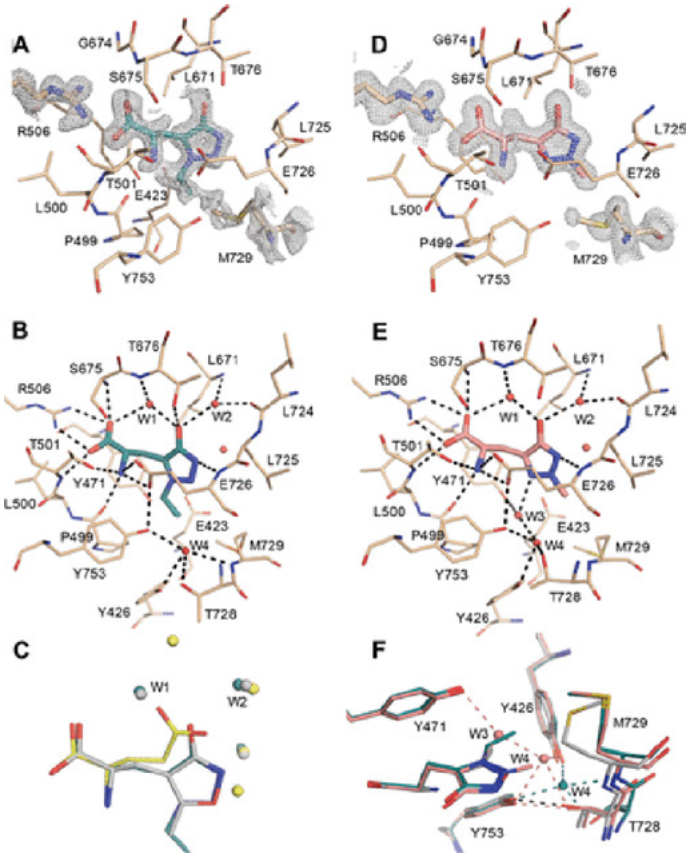

Structures of GluA2-ABD with 6b and 7a. (A) Simple PHENIX omit 2Fo–Fc map around 6b, Arg506, and Met729, carved at 1.6 Å and contoured at 1 sigma (chain A). GluA2-ABD residues within 4 Å of 6b are shown in beige stick representation. Molecule 6b is shown in cyan stick representation. (B) Hydrogen-bonding network (up to 3.2 Å; black dashed lines) among binding-site residues, 6b, and water molecules (red spheres). (C) Comparison of binding modes of 6b (chain A), AMPA (grey, chain A), and Glu (yellow, chain A). The structures were overlaid on lobe D1 residues. Only water molecules (within 4 Å of the ligands) are shown for clarity and coloured according to the respective ligands. (D) Simple PHENIX omit 2Fo–Fc map around 7a, Arg506, and Met729, carved at 1.6 Å and contoured at 1 sigma (chain A). Molecule 7a is shown in salmon stick representation. (E) Hydrogen-bonding network among binding-site residues, 7a, and water molecules. (F) Zoom on the hydrogen-bonding network of W3 and W4 in the GluA2-ABD structures with 6b (cyan), 7a (magenta), and AMPA (grey).

Since compound 8 also activates the Glu site, the hydroxy- 1,2,3-triazole moiety is the first bioisostere capable of enabling the simultaneous activation of the Glu and Gly sites. It seems probable that the bioisostere of compound 8 is recognized in two different states: negatively charged in the Glu binding pocket and neutral in the Gly binding pocket. This would be enabled by the pKa of the bioisostere being close to 7.

Funding

This work was funded by the University of Turin, Ricerca Locale 2016/2017 (grant nos LOLM_RILO_17_01, BOSD_RILO_17_01), Ministero dell'Istruzione, dell'Università e della Ricerca PRIN 2015 (LOLM_- PRIN_2015_16_01), the Lundbeck Foundation, Danscatt, and by the NIH (GM103546 and NS097536).

Publication

Reprinted in part with permission fram Sainas S., Temperini P., Farnsworth J.C., *et al.* Use of the 4-Hydroxytriazole Moiety as a Bioisosteric Tool in the Development of Ionotropic Glutamate Receptor Ligands *J. Med. Chem*. 2019, 62, 9, 4467–4482

https://doi.org/10.1021/acs.jmedchem.8b01986

Structure and binding of PAMs to glutamate receptor splice variants

Positive allosteric modulators (PAMs) play a regulatory role in the active phase of ligand-gated ion channel activity in the presence of the neurotransmitter glutamate. This study structurally characterizes new dimeric positive allosteric modulators, TDPAM01 and TDPAM02, and their binding to alpha-amino-3-hydroxy-5-methyl-4-isoxazolepropionic acid (AMPA) receptor, GluA2.

The Science

Positive allosteric modulators are important drug candidates and valuable compounds for studying receptor function. PAMs bind and stabilize a receptor in the activated form, delaying either deactivation of the receptor or its entrance into a desensitized state where the channel is closed. Ionotropic glutamate receptor GluA2 is the most studied of the AMPA receptors. The receptor exists in two splice variants, the flip and flop isoforms.

This study reports a detailed structural characterization of dimeric PAMs, TDPAM01 and TDPAM02, with nanomolar potency at GluA2. We show that the two PAM binding sites at the GluA2-LBD dimer interface can host one molecule of the dimeric modulator TDPAM02, occupying the positions of two separated monomeric PAMs. TDPAM01 and TDPAM02 were capable of crystallizing with different variants of the GluA2-LBD: flop, flip-like, and flip-like preformed dimer as well as both the L-glutamate bound and L-glutamate unbound forms. Thus, we conclude, in the synapse the TDPAMs might bind to different states of the receptor and stabilize it in a compact conformation ready for activation by L-glutamate.

The Impact

Structural knowledge of how positive allosteric modulators TDPAM01 and TDPAM02 bind with GluA2 receptors splice variants is one piece of the puzzle to explain typical ligand-gated processes in synaptic transmission. This information is valuable in future design and synthesis of PAMs for development of medical treatments of glutamate receptor-related diseases in the central nervous system.

Summary

We synthesized two highly potent dimeric PAMs of the AMPA receptors, TDPAM01 and TDPAM02. Via calcium flux experiment on HEK293 cells expressing GluA2 flop (Q), the potency of TDPAM01 and TDPAM02 was determined to 13.4 and 1.4 nM, respectively. Using X-ray crystallography, TDPAM01 and TDPAM02 were crystallized in the ligand-binding domain of the GluA2 flop isoform, the flip-like mutant N775S, and the preformed dimer L504Y-N775S.

First, TDPAM01 was successfully co-crystallized with the GluA2-LBD flop. To establish the binding mode of TDPAM02, we crystallized the modulator in complex with the ligand-binding domain of the GluA2 flip-like N775S (GluA2-LBD flip) and L-glutamate. GluA2-LBD flop crystallized with TDPAM02 as a dimer with an expanded orthosteric binding cleft. We also crystallized TDPAM02 in complex with the preformed dimer of GluA2-L504Y-N775S (GluA2-LBD predimer) to investigate if TDPAM02 was capable of binding to this receptor form. As expected, GluA2-LBD predimer crystallized as a dimer, and the structure is very similar to the structure of GluA2-LBD flip. X-ray diffraction data was collected at BioMAX beamline.

In all structures, one modulator molecule binds at the dimer interface with two characteristic hydrogen bonds being formed from the modulator to Pro515. Whereas the GluA2 dimers and modulator binding mode are similar when crystallized

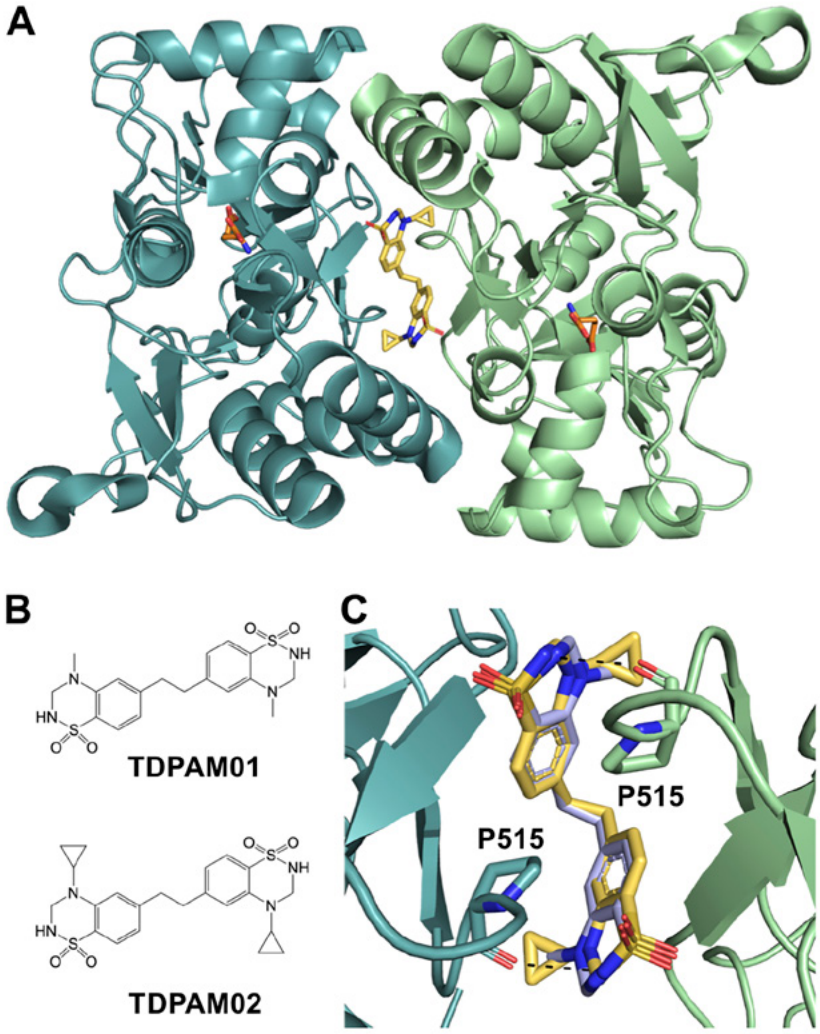

Dimeric structure of GluA2-LBD (flip-like) in complex with TDPAM02. (A) Top-view of the GluA2-LBD dimer in cartoon representation (dark green for chain A; light green for chain B), showing that TDPAM02 (carbon atoms in beige) binds at the dimer interface. L-Glutamate is shown with carbon atoms in orange. (B) Structures of TDPAM01 and TDPAM02. (C) Overlay of the structures of GluA2-LBD (flip-like) with TDPAM01 (carbon atoms in light blue) and TDPAM02, showing that the two compounds bind in a similar way. Hydrogen bonds between TDPAM02 and Pro515 of each protein molecule are shown as black dashed lines. Nitrogen atoms are shown in blue, oxygen in red and sulfur in yellow.

in the presence of L-glutamate, the shape of the binding site differs when no L-glutamate is present. TDPAM02 has no effect on domain closure in both apo and L-glutamate bound GluA2 dimers compared to structures without modulator.

Five structures of GluA2-LBD were determined, which yielded evidence for a 10-fold better potency of TDPAM02 over TDPAM01 and showed that TDPAM01 and TDPAM02 can bind to both the GluA2 flop and flip variants as well as to a preformed dimer of GluA2. In addition, we show that TDPAM02 can bind to both the L-glutamate bound and unbound (apo) structures.

Funding

This work was funded by Independent Research Fund Denmark FNU– Natural Sciences, Danscatt, and Fonds National de la Recherche Scientifique (F.N.R.S.).

Publication

Reprinted in part with permission from Laulumaa S., Hansen K.V., Masternak M., et al. Crystal Structures of Potent Dimeric Positive Allosteric Modulators at the Ligand-Binding Domain of the GluA2 Receptor, *ACS Med. Chem. Lett.* 2019, 10, 3, 243–247

https://doi.org/10.1021/acsmedchemlett.8b00369

Activation mechanism of protein complex with a role in DNA repair

The study aims at understanding the structure and activation of the Prp19 protein complex. The protein has a role in diverse processes from pre-mRNA splicing to the DNA damage response. One part of the study was performed at the I911-4 SAXS beamline at MAX II.

The Science

The Prp19/nineteen complex (NTC) is a multifunctional protein complex involved in very diverse biological processes, including pre-mRNA splicing and the DNA damage response (DDR). In humans, NTC consists of a conserved core and the proteins CTNNBL1, AD002, and Hsp73. The NTC core contains Prp19 (Pso4/SNEV), SPF27 (hSnt309), cell-division-cycle-5-like (CDC5L/hCef1), and the pleiotropic regulator 1 (PLRG1/hPrp46).

The study shows that Prp19 is an autoinhibited ubiquitin ligase and determine its crystal structure. The work provides insight into how several splicing-factors associate with Prp19 and convert it into an active conformation, thereby enabling ubiquitination of RPA during DNA damage response.

The Impact

By employing an integrated approach consisting of X-ray crystallography, protein-protein crosslinking, homology modelling, and functional assays in vitro and in vivo, we show that Prp19 alone is an autoinhibited E3 ubiquitin ligase and define the molecular basis of its activation.

Future structural studies may clarify whether the role of coiled coils as a platform for structural transitions, as observed for Prp19, might be extended to ligases from other classes.

Summary

Human nineteen complex (NTC) acts as a multimeric E3 ubiquitin ligase in DNA repair and splicing. The transfer of ubiquitin is mediated by Prp19—a homotetrameric component of NTC whose elongated coiled coils serve as an assembly axis for two other proteins called SPF27 and CDC5L.

We find that Prp19 is inactive on its own and have elucidated the structural basis of its autoinhibition by crystallography and mutational analysis. Formation of the NTC core by stepwise assembly of SPF27, CDC5L, and PLRG1 onto the Prp19 tetramer enables ubiquitin ligation. Protein-protein crosslinking of NTC, functional assays in vitro, and assessment of its role in DNA damage response provide mechanistic insight into the organization of the NTC core and the communication between PLRG1 and Prp19 that enables E3 activity.

This reveals a unique mode of regulation for a complex E3 ligase and advances understanding of its dynamics in various cellular pathways.

SAXS was employed to study the overall structures of ctPrp19^{core}, the ctPrp19^{WD40} and the full-length ctPrp19 in solution. The two former constructs were measured at the EMBL beamline P12 of the Petra-3 storage ring, DESY, Hamburg, Germany on a Pilatus 2M detector. The latter construct was measured at the I911-4 beamline (MAX II ring)

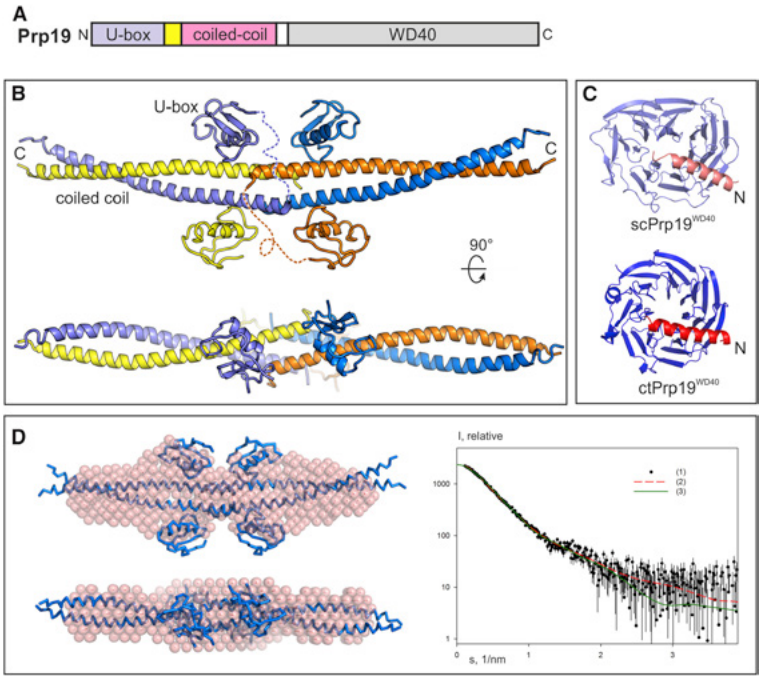

Structure of Prp19
A) Domain composition. The yellow and white boxes indicate linker regions between the flanking domains,
B) and C) Crystal structures of the ctPrp19 stalk (B) and the WD40 domains (C).
D) The ab initio model from SAXS (transparent beads) superposed with the crystal structure of the ctPrp19stalk (Ca trace, left panel).
The right panel presents the fit to the SAXS experimental data (black dots with error bars) by the scattering from the ab initio model (red; discrepancy of the fit $\chi 2$ = 1.02) and that calculated from the crystal structure (green; discrepancy $\chi 2$ = 1.47). The scattering intensity is displayed as a function of the momentum transfer $s = 4\pi \sin(\theta)/\lambda$, where 2θ is the scattering angle and λ is the X-ray wavelength.

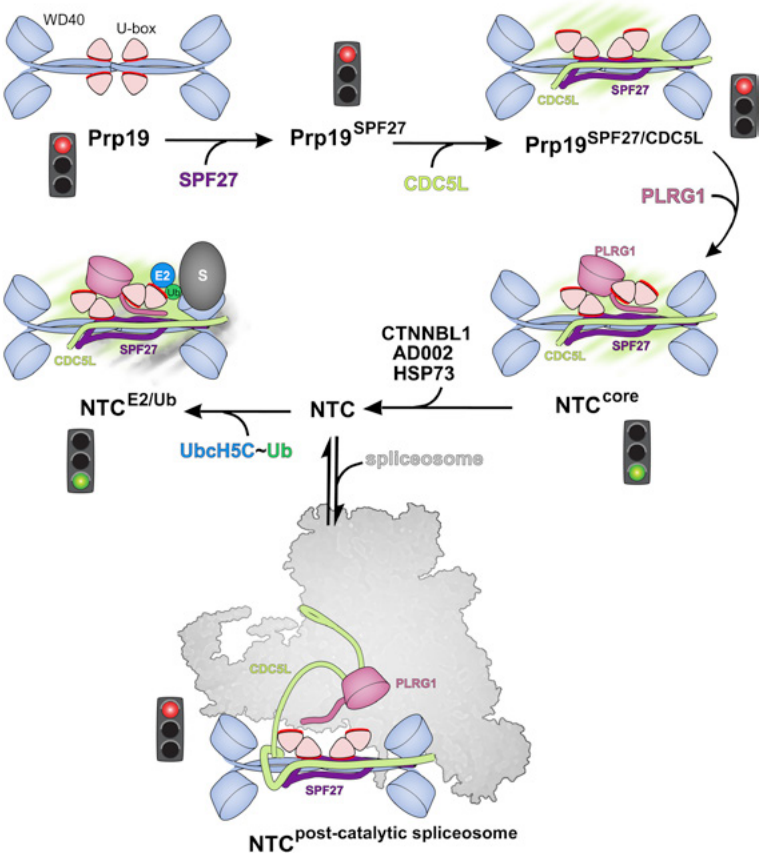

Schematic Model of the Working Prp19 Complex. The E2-interacting surfaces of the Prp19 U-box domains are depicted in red.
The large N-terminal region of CDC5L is only illustrated within the spliceosome. Streetlight symbols indicate the E3 ubiquitin ligase activity of Prp19 (red light, inactive state; green light, active state). Prp19 undergoes several structural reorganizations upon assembly of the NTC components, and these convert it from an autoinhibited state to an active state, enabling the E2 to transfer ubiquitin to the substrate.

Publication

Reprinted in part from R. de Moura Tales, S. Mozaffari-Jovin, C.Z.K. Szabo, et al. Prp19/Pso4 Is an Autoinhibited Ubiquitin Ligase Activated by Stepwise Assembly of Three Splicing Factors, Molecular Cell 69, 6, 2018, 979-992 with permission from Elsevier
https://doi.org/10.1016/j.molcel.2018.02.022

Funding

This work was supported by the DFG grant PE 2079/1-1 (T.R.d.M., J.S., and V.P.) and SFB 860 (R.L. and H.U.)

Studying the dynamics of microtubule filaments at room temperature

Biological filaments are dynamic systems. Their function and formation play an important role in everything from muscles and bacteria to neuro-degenerative diseases such as Alzheimer's and Parkinson's diseases. X-ray free electron lasers offers the ability to study the dynamics of these systems at biologically relevant temperatures and conditions. In this study microtubule solutions were imaged to a resolution of 2 nanometers.

The Science

In the study we demonstrate the potential of single-molecule imaging of dynamic biological systems at biologically relevant temperature and conditions. X-ray imaging data were collected at the LCLS (an X-ray free electron laser in California) and were complemented by X-ray scattering data recorded at MaxLab.

X-ray crystallography has revolutionized the biological sciences with atomic-level information on DNA, proteins and other components of living cells. X-ray crystallography, however, requires that the biological samples form well-ordered crystals. Growing good enough quality crystals from most classes of biological filaments is difficult. Therefore, the current knowledge of the structure of biological filaments largely stems from other methods such as cryo electron microscopy, which usually require that the sample is static and frozen.

Microtubules are biological filaments found in the cytoskeleton that gives structure to cells. Microtubules are hollow cylinders with a diameter of 24 nm and are built up of tubulin dimers approximately 4 nm in size. Understanding the dynamics of microtubule growth and shrinkage requires new methods that are capable of imaging biological filaments at biologically relevant temperatures and conditions.

X-ray free electron lasers (XFELs) offers short, intense and coherent pulses in the femtosecond regime. With extremely intense and short pulses it is possible to collect data before the biological molecule being examined is destroyed. It is therefore not necessary to work at cryogenic temperatures. XFELs thus create new possibilities for coherent X-ray diffraction imaging, but for large biological particles such as viruses, the current resolution is limited to tens of nanometers. Biological polymers such as microtubule represent an intermediate step between a 3D crystal and single molecules since their structure is repeated along the transitional axis, giving them 1D helical symmetry.

We injected a solution of microtubules across an XFEL beam and collected 2D diffraction patterns. By using data analysis software adapted from cryo electron microscopy we were able to recover the structure of the microtubule with a resolution of 4 nm. This opens a path towards imaging dynamical biological samples at relevant temperatures and conditions.

The Impact

Biological filaments are essential to cell structure, muscle fibers or bacterial flagella. Amyloid fibrils, a class of biological filaments, are involved in several neurodegenerative diseases such as Alzheimer's and Parkinson's diseases. Coherent diffraction imaging at X-ray laser sources open up a route towards imaging biological filaments without the need of crystallisation or cryogenic approaches. In the future, these methods should allow new structural insights into their dynamics since data can be recorded at biologically relevant temperatures.

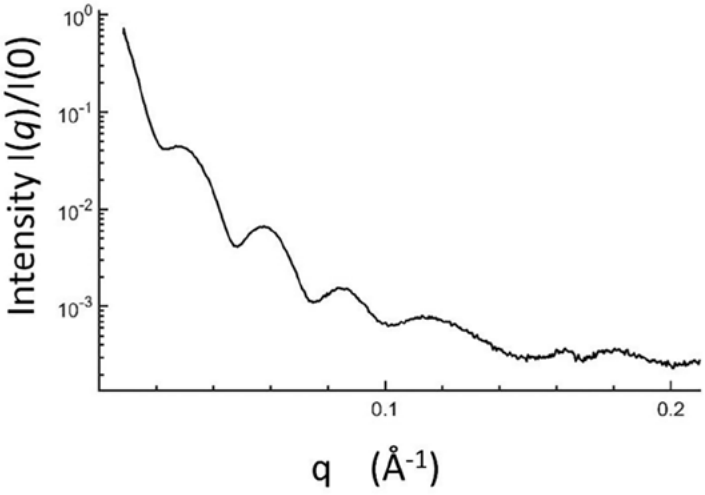

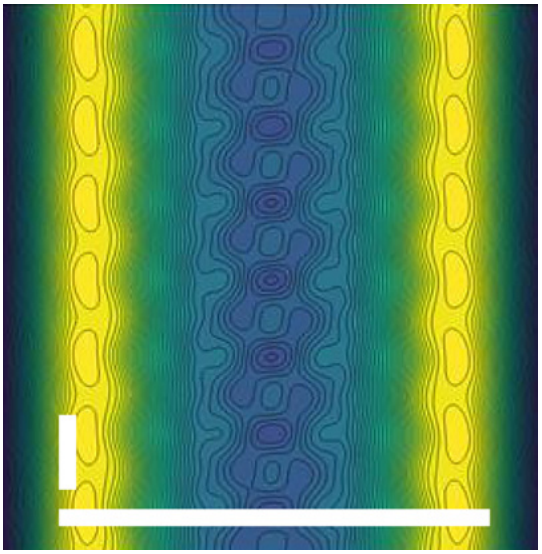

Figure 1 (left) Characterization of microtubules at MAX II beamline I911-4. Small-angle X-ray scattering data of microtubules were collected at 17 °C using X-ray exposures of 2 seconds. Normalized intensities are plotted on a logarithmic scale.
Figure 2 (right) Projection images of microtubules recovered by iterative phase retrieval. This 2D projection image was recovered after 100 cycles of iterative phase retrieval from class-averaged data. Both the average microtubule diameter of approximately 25 nm and sub-structures of 4 nm become visible. White bars indicate 25 nm in the horizontal direction and 4 nm in the vertical direction.

Summary

X-ray free electron lasers (XFELs) offer coherent X-ray pulses at a femtosecond timescale. This have led to new opportunities in studying dynamical biological objects using the coherent X-ray diffraction imaging method. In this study we studied the biological filament microtubule at an XFEL. The resulting X-ray scattering images were sorted into class averages and merged into a diffraction pattern with a resolution extending to 2 nm. We could resolve details such as the 4 nm tubulin monomer in the reconstructed image.

Funding

Use of the Linac Coherent Light Source (LCLS), SLAC National Accelerator Laboratory, is supported by the U.S. Department of Energy, Office of Science, Office of Basic Energy Sciences under Contract No. DE-AC02-76SF00515. Parts of the sample delivery system used at LCLS for this research was funded by the NIH Grant P41GM103393, formerly P41RR001209. R.N. acknowledges funding from the Knut and Alice Wallenberg Foundation (Grant Numbers KAW 2012.0284, KAW 2012.0275 and KAW 2014.0275), the Swedish Research Council (Grant Numbers 2015-00560 and 349-2011-6485) and the Swedish Foundation for Strategic Research (Grant Number SRL10-0036). We are grateful for support from the Helmholtz Association through project-oriented funds to DESY. R.C.R. was supported by A*STAR (Agency for Science, Technology and Research), Singapore. PHZ was supported by the National Institutes of Health (NIH) under Award R01GM109019.

Publication

Brändén, G., Hammarin, G., Harimoorthy, R. et al. Coherent diffractive imaging of microtubules using an X-ray laser. *Nat Commun* **10**, 2589 (2019). https://doi.org/10.1038/s41467-019-10448-x
Open Access

A method for using H_2 to functionalise graphene

Hydrogen atoms adsorbed to graphene change the material properties and opens up a path to interesting applications from spintronics to hydrogen storage. This study proposes a route for functionalisation using hydrogen gas H_2 instead of the more studied atomic hydrogen.

The Science

The controlled chemical functionalization of graphene is of broad interest for modifying its chemical, optical, mechanical, and electronic properties. The adsorption of a single H atom onto the graphene lattice induces magnetic moments in the sheet enabling the development of spintronic devices. At a higher hydrogen coverage, manipulation of the global electronic structure is possible, and in some systems a tunable band gap can be obtained, which is of interest for the use of graphene in electronic applications. A complete hydrogenation of graphene by H atoms yields graphane, which has been proposed as a hydrogen storage material.

The interaction between graphene and its substrate is a crucial factor for the reactivity of graphene and thus for its chemical functionalization. Several experimental and theoretical studies have shown that hot atomic hydrogen can chemisorb onto the basal plane of graphite, free-standing graphene, and graphene on metal and semiconductor substrates. While functionalization of graphene with atomic H is well established, functionalization using H_2 molecules is less explored and is in general energetically unfavourable due to the high stability of the H_2 molecule.

We have demonstrated a route to graphene functionalization using vibrationally excited H_2 molecules. The functionalization occurs in a highly ordered manner and is therefore a viable tool for band gap engineering of graphene. The functionalization route exploits the finding that graphene can mediate the catalytic activity of an underlying metal substrate resulting in reduced dissociative adsorption barriers for molecular hydrogen on graphene. Furthermore, the described mechanism exhibits an avalanche effect where the first dissociative adsorption event leads to reduced barriers for subsequent dissociative adsorption.

The Impact

This study is not only an important proof of concept, but the essential insight provided by the mechanism, where nucleation is the most energetically expensive step for the graphene hydrogenation, provides an approach toward the detailed control of graphene and its properties, through chemical functionalization.

Summary

Here we present combined scanning tunneling microscopy (STM), high-resolution electron energy loss spectroscopy (HREELS), and X-ray photoemission spectroscopy (XPS) data to demonstrate that highly vibrationally excited H_2 molecules can functionalize gr/Ir(111), yielding highly ordered nanopatterned graphene, via dissociative adsorption reactions. Ambient pressure XPS (APXPS) excludes the possibility of graphene hydrogenation through direct dissociation of H_2 molecules on the Ir(111) surface. The experimental observations are supported by density functional theory (DFT) calculations showing that the dissociation barrier is lowered substantially by the graphene-mediated catalytic effect of the Ir substrate.

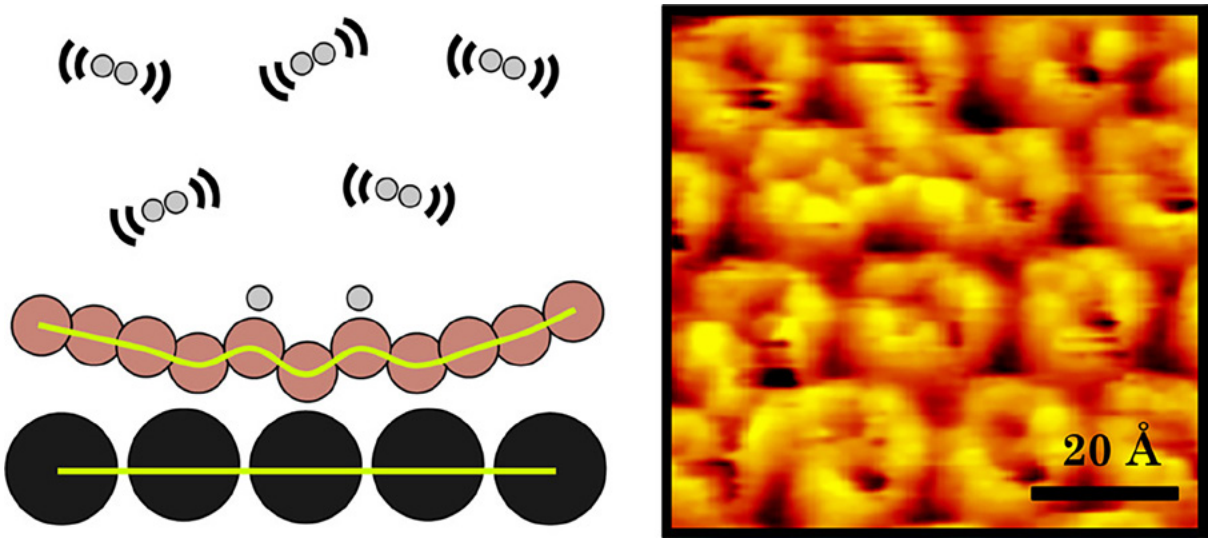

Excited H_2 molecules over a graphene sheet on Iridium and a scanning tunnelling microscopy image showing the H_2 molecules adsorbed on graphene.

Moreover, the barrier to adsorption continues to decrease for further addition of H_2 at sites adjacent to adsorbed molecules due to local distortion effects. Consequently, an avalanche of H_2 dissociation and H-addition reactions becomes possible, providing an efficient route toward hydrogenation.

Funding

The authors acknowledge financial support from The Danish Council for Independent Research (grant no. 0602-02566B and grant no. 0602-02265B), Innovation Fund Denmark (NIAGRA), The European Research Council (CoG GRANN), Villum Foundation via Villum Centre of Excellence for Dirac Materials (Grant no. 11744).
H.B. acknowledges support by the Director, Office of Science, Office of Basic Energy Sciences, and by the Division of Chemical Sciences, Geosciences and Biosciences of the U.S. Department of Energy at LBNL under contract no. DE-AC02-05CH11231. The Advanced Light Source is supported by the Director, Office of Science, Office of Basic Energy Sciences of the U.S. Department of Energy at LBNL under contract no. DE-AC02-05CH11231.

Publication

L. Kyhl, R. Bisson, R. Balog, M.N. Groves, E. Leonhard Kolsbjerg, A.M. Cassidy, J. Holm Jørgensen, S. Halkjær, J.A. Miwa, A. Grubišić Čabo, T. Angot, P. Hofmann, M. Alif Arman, S. Urpelainen, P. Lacovig, L. Bignardi, H. Bluhm, J. Knudsen, B. Hammer, and L. Hornekaer, Exciting H2 Molecules for Graphene Functionalization, *ACS Nano* 2018, 12, 1, 513-520, https://doi.org/10.1021/acsnano.7b07079
Open Access

Combination of experimental methods for exploring bone fracture across length scales

Bone is a complex material with specific structure on several different length scales. Understanding how and why it fractures requires the possibility of combining a number of experimental methods with in-situ tensile testing. Experiments carried out at beamline I911-4 shows how strains depend on the local structure across hierarchical levels.

The Science

The incidence of fragility fractures is expected to increase in the near future due to an aging population. Therefore, improved tools for fracture prediction are required to treat and prevent these injuries efficiently. For such tools to succeed, a better understanding of the deformation mechanisms in bone over different length scales is needed.

In this study, an experimental setup including mechanical tensile testing in combination with digital image correlation (DIC) and small/wide angle X-ray scattering (SAXS/WAXS) was used to study deformation at multiple length scales in bovine cortical bone. Furthermore, micro-CT imaging provided detailed information about tissue microstructure. The combination of these techniques enabled measurements of local deformations at the tissue- and nanoscales.

The study clearly shows the potential of combining these different experimental techniques concurrently with mechanical testing to gain a better understanding of bone damage and fracture over multiple length scales in cortical bone.

The Impact

To understand the pathophysiology of bone, it is important to improve our knowledge about the deformation and fracture mechanisms in bone. In this study, we combine several recently available experimental techniques with mechanical loading to investigate the deformation mechanisms in compact bone tissue on several length scales simultaneously.

The experimental setup included mechanical tensile testing in combination with digital image correlation, microCT imaging, and small/wide angle X-ray scattering.

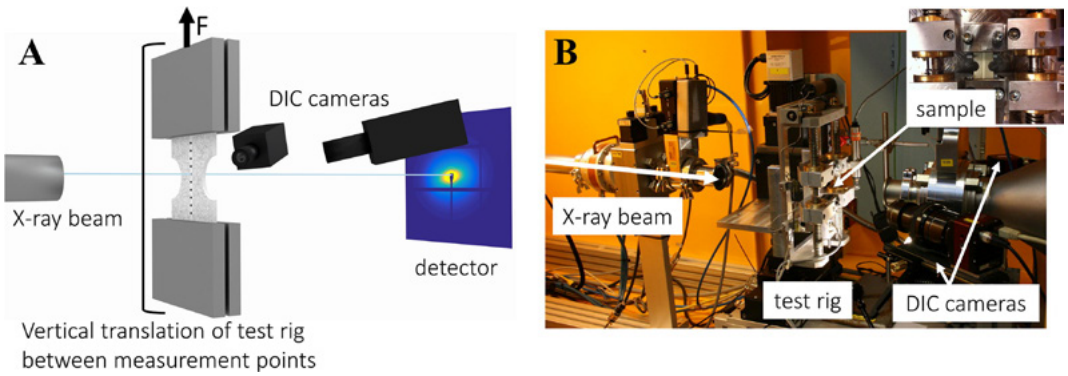

Experimental setup. (A) Schematic illustration of a sample tested in tension and simultaneously monitored with DIC and SAXS or WAXS at 10 discrete vertical positions in the horizontal-centre of the sample. The sample is subjected to continuous tensile loading in the test rig and the whole rig is translated vertically to move the sample between the measurement points inside the beam. (B) Photograph of the experimental setup at the I911-4 beamline

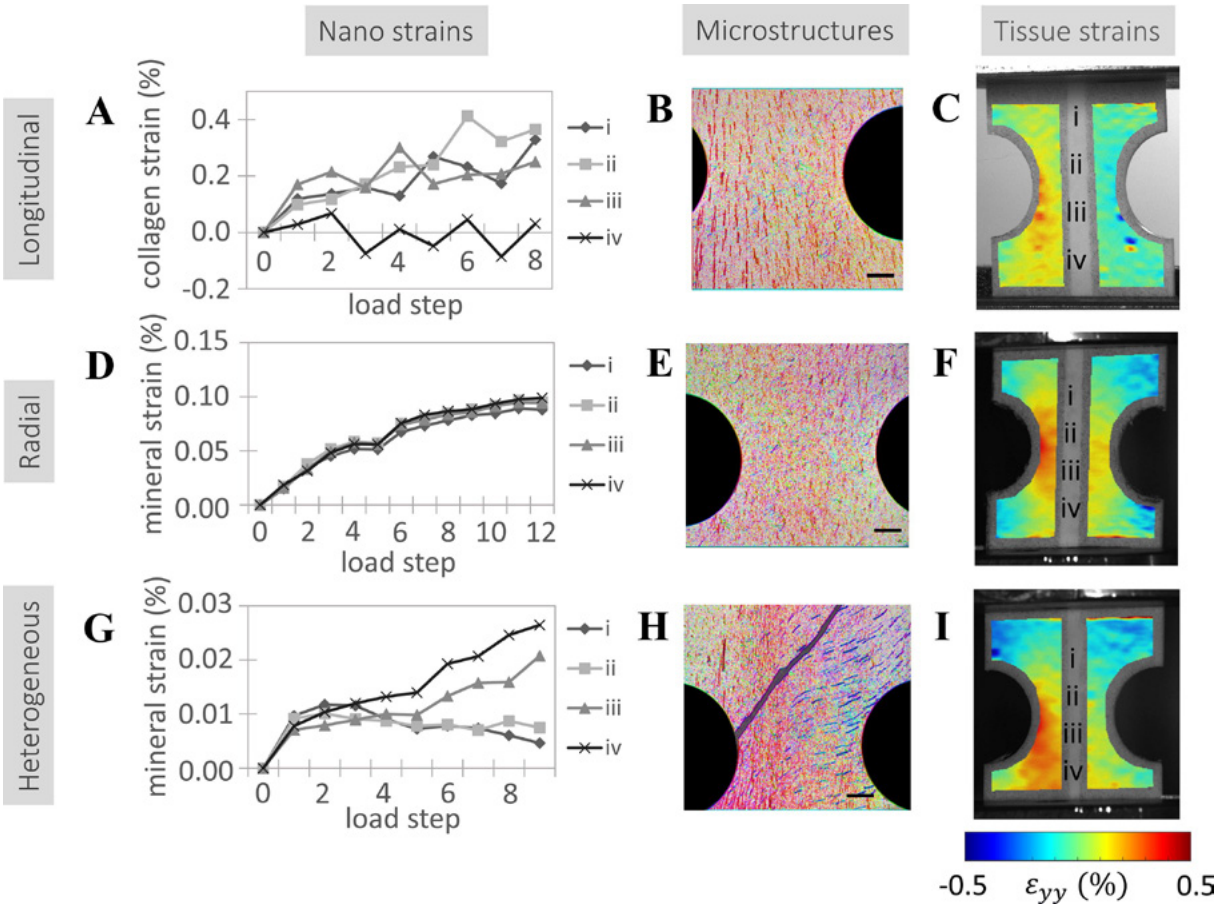

Local deformations at the nano- and tissuescale compared to microstructure. Typical in situ measurements from SAXS and WAXS showing strains in collagen (A) and minerals (D and G) at each load step, to be compared with the microstructural orientations (B, E, H) and the tissuescale surface strains (C, F, I) analyzed with DIC at the last load step before fracture. Collagen and mineral strains in (A, D, G) are given at four points (i–iv) and their approximate locations are marked on the samples in (C, F, I). The nano strain values are calculated as average values between two neighboring measurement points. Scale bars in the micrographs (B, E, H) represent 2 mm.

The combination of techniques enabled measurements of local deformations at the tissue- and nanoscales. The study clearly shows the potential of combining different experimental techniques concurrently with mechanical testing to gain a better understanding of structure-property-function relationships in bone tissue.

Summary

An experimental method combining in situ SAXS/WAXS with DIC and mechanical testing was adopted to study deformations over several length scales simultaneously and compare these to the microstructural orientation visualized with high resolution micro-CT. The results indicate that strains on both tissue- and nanoscale depend on the microstructure and illustrate its loadbearing function in cortical bone. Perhaps most importantly, this study demonstrates the potential of an experimental setup where different measurement techniques are combined to enable mapping of local deformations at several hierarchical levels to improve our understanding of multiscale deformation in cortical bone. The research was carried out at the I911-4 beamline at MAX II, the predecessor of MAX IV.

Funding

This work was supported by the Swedish Foundation for Strategic Research [IB2013-0021] and Academy of Finland [project 286091].

Publication

Gustafsson A., Mathavan N., Turunen M.J., Engqvist J., Khayyeri H., Hall S.A., Isaksson H., Linking multiscale deformation to microstructure in cortical bone using in-situ loading, digital image correlation and synchrotron X-ray scattering, Acta Biomaterialia 69, 2018, 323-331.
https://doi.org/10.1016/j.actbio.2018.01.037
Open Access

The journey to real-time PET molecular imaging gets “faster”

Researchers from different institutions came to MAX IV to study timing performance of scintillators, materials employed in medical imaging applications such as cancer diagnosis. At FemtoMAX an exceptional instrumental time resolution of 38 picoseconds was achieved, providing superior conditions for studies of ultrafast processes.

The Science

The technological challenge imposed by the time resolution essential to achieve real-time molecular imaging calls for a new generation of ultrafast detectors. In this contribution, we demonstrate that CdSe-based semiconductor nanoplatelets can be combined with standard scintillator technology to achieve 80 ps coincidence time resolution on a hybrid functional pixel.

This result contrasts with the fact that the overall detector light output is considerably affected by the loss of index-light-guiding. Here, we exploit the principle of 511 keV energy sharing between a high-Z, high stopping power bulk scintillator, and a nano-scintillator with sub-1 ns radiative recombination times, aiming at a breakthrough in the combined energy and time resolution performance. This proof-of-concept test opens the way to the design and study of larger size sensors using thin nanocomposite layers able to perform as efficient time taggers in a sampling detector geometry of new generation.

The Impact

One important application of scintillating materials is in time-of-flight positron emission tomography (TOF-PET), a crucial technique in fields such as cancer diagnosis. The timing performance of scintillators used nowadays in TOF-PET is one of the bottlenecks to reach real-time molecular imaging for cancer diagnosis

In a TOF-PET scanner, scintillator crystals detect the energy emitted by a radioactive radiotracer inside the tissue and transforms it into visible light.

The next step in the evolution of TOF-PET technology revolves around improving the time resolution of the scanner to achieve real-time molecular imaging. Having real-time information on how tumorous cells behave within the human body would revolutionize the way we diagnose, monitor, and treat cancer.

One way to improve time resolution of TOF-PET scanners and get closer to real-time imaging is by implementing faster scintillators with better timing performance, such as the ultrafast CdSe-based nanoplatelets studied in this work. A TOF-PET scanner detects pairs of photons emitted in coincidence from the tissue in opposite directions. The difference in the time these two photons take to reach opposite scintillator crystals (t2 – t1) defines the location of radioactive decay event. The better is the time resolution, the more accurate is the location measurement and the better the image we can obtain from a TOF-PET scan.

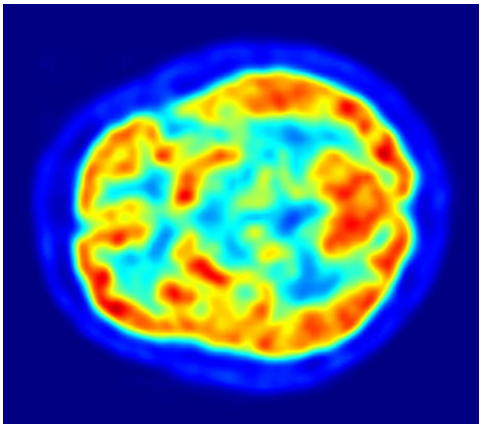

This is a transaxial slice of the brain of a 56 year old patient (male) taken with positron emission tomography (PET). Author: Jens Maus. Source: wikipedia.org

Summary

In this paper, we start from the luminescence properties of individual CdSe/CdS nanoplatelets under laser and X-ray excitation, which revealed red-shifted biexcitonic RL at room temperature. We follow-up with a study of the light emission features of a more complex system, in which nanocrystals are either drop-casted on LYSO or forming a nanocomposite. The drop-casting technique using LYSO as direct substrate has been chosen to understand and demonstrate the timing capabilities potential of CdSe under 511 keV gamma excitation, as this method is capable of using the standard scintillator as a waveguide, transporting light to the photodetector. However, this compromises the performance of the heavy scintillator needed for the detector's energy resolution, so we follow-up with a nanocomposite approach, where CdSe/CdS nanoplatelets are mechanically stabilized on a host matrix, as this is key for real detector applications.

Time-resolved ultrafast decay kinetics of a first generation CdSe-based nanocomposite under 100-fs X-ray excitation is shown together with first light output measurements obtained by X-ray attenuation and cross-checked by spectrally-resolved pulsed cathodoluminescence.

We present first time results on the characterization of a sampling scintillating pixel, where standard LYSO 200 µm-thick plates are combined with CdSe/CdS nanoplatelets for 511 keV gamma detection. The promising results on the decay kinetics and time resolution obtained with a still non-optimized CdSe-LYSO sampling pixel are pushing for developing reproducible and scalable methods to produce CdSe-based built-up transparent nanocomposite layers at least 100 µm thick in order to substitute the drop-casted films in the hybrid pixel geometry. The ultimate goal of TOF-PET development is to achieve 10-picosecond time resolution. To obtain a scintillator that fulfills this goal, its scintillation decays have to be studied with comparable precision. Our paper shows that FemtoMAX is among the first tools that can achieve such precision, opening new possibilities in research of ultrafast scintillators.

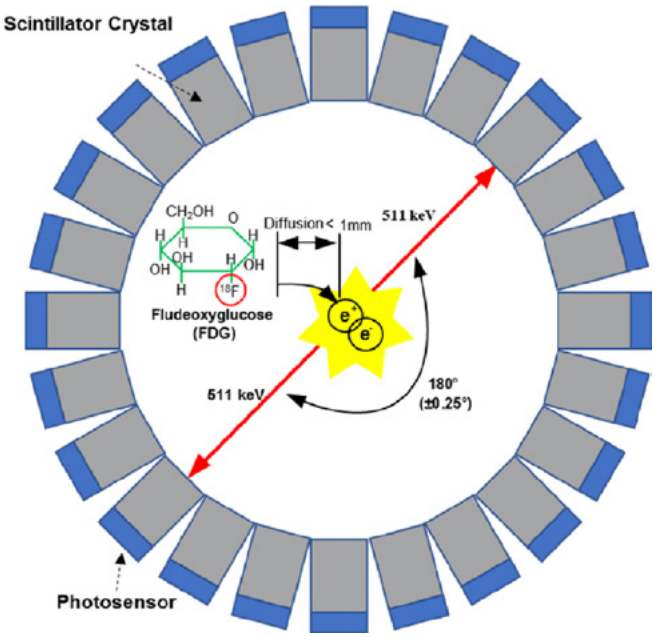

The basic principle of a positron emission tomography (PET) system: A PET detector ring detects a pair of gamma photons with an energy of 511 keV (red arrows) which results from the annihilation of an electron with a positron emitted by the radiotracer (FDG). Source: Sensors for Positron Emission Tomography Applications – Scientific Figure on ResearchGate.

Funding

This work was supported by the ERC Advanced Grant no. 338953 (TICAL), the ERC Starting Grant no. 714876 (PHOCONA), and Estonian Research Council (projects PUT1081, IUT2-26). A partial financial support from the Estonian Centre of Excellence TK141 by the EU through the European Regional Development Fund (TK141, project no. 2014-2020.4.01.15-0011) is gratefully acknowledged. The research have been developed in the frame of the Crystal Clear Collaboration and the Cost Action FAST TD1401.

Publication

R.M. Turtos, S. Gundacker, S. Omelkov. et al.
On the use of CdSe scintillating nanoplatelets as time taggers for high-energy gamma detection.
npj 2D Mater Appl **3**, 37, 2019.
https://doi.org/10.1038/s41699-019-0120-8
Open Access

High quality ZrB_2 film characterized by X-ray spectroscopy

ZrB_2 was epitaxially grown on a heated Al_2O_3 substrate by sputtering of a compound target. The resulting film was confirmed to have high quality and atomic order by several different X-ray methods. The result shows promise for growth and characterization of this technologically important material and others of similar structure.

The Science

Zirconium dibromide (ZrB_2) can be grown as a film on top of other materials. The method investigated in this study is to sputter a target of ZrB_2 using argon gas over an aluminum oxide substrate at 900ºC. The uniformity of the film may be affected by contamination of oxygen and carbon. Four different X-ray based methods were used to examine the resulting film. It has a high uniformity with a low oxygen and carbon content as compared to the ZrB_2 sputtering target and a bulk α-Zr reference sample.

The Impact

ZrB_2 is of interest for technological applications such as metal cutting, aerospace or electronics. This is because of its high melting point, high hardness and good corrosion resistance. These properties arise from the ZrB_2 crystal structure and chemical bonding. Therefore, it is important to be able to grow high quality uniform films and understand the chemical bonding in detail.

Summary

A ZrB_2 film was grown epitaxially on an Al_2O_3(0001) substrate using sputtering of a ZrB_2 compound target. ZrB_2 has a crystal structure in which B atoms form graphite-like sheets between hcp Zr layers. The epitaxial film grows as columns which are up to a few tens of nm wide on the substrate. Contaminants in the ZrB_2 film may interrupt the film growth resulting in grains or amorphous material.

The film was characterized using the X-ray based methods extended X-ray absorption fine structure (EXAFS), X-ray absorption near-edge spectroscopy (XANES) and X-ray Photoelectron Spectroscopy (XPS). The EXAFS and XANES measurements were conducted at the beamline I811 of MAX II. The XANES and EXAFS measurements give information about the chemical bonding in the film. XPS is used to quantify the amount of impurities and XRD is used to determine the crystal structure.

The film grown had a low contamination level around 5 at. % C and 2 at. % O. It has a high quality and atomic order as shown by XANES and EXAFS of the of the Zr K-edge (1s). The experiment setup also shows promise for use on other types of materials with a similar structure as ZrB_2 (Strukturbericht C32).

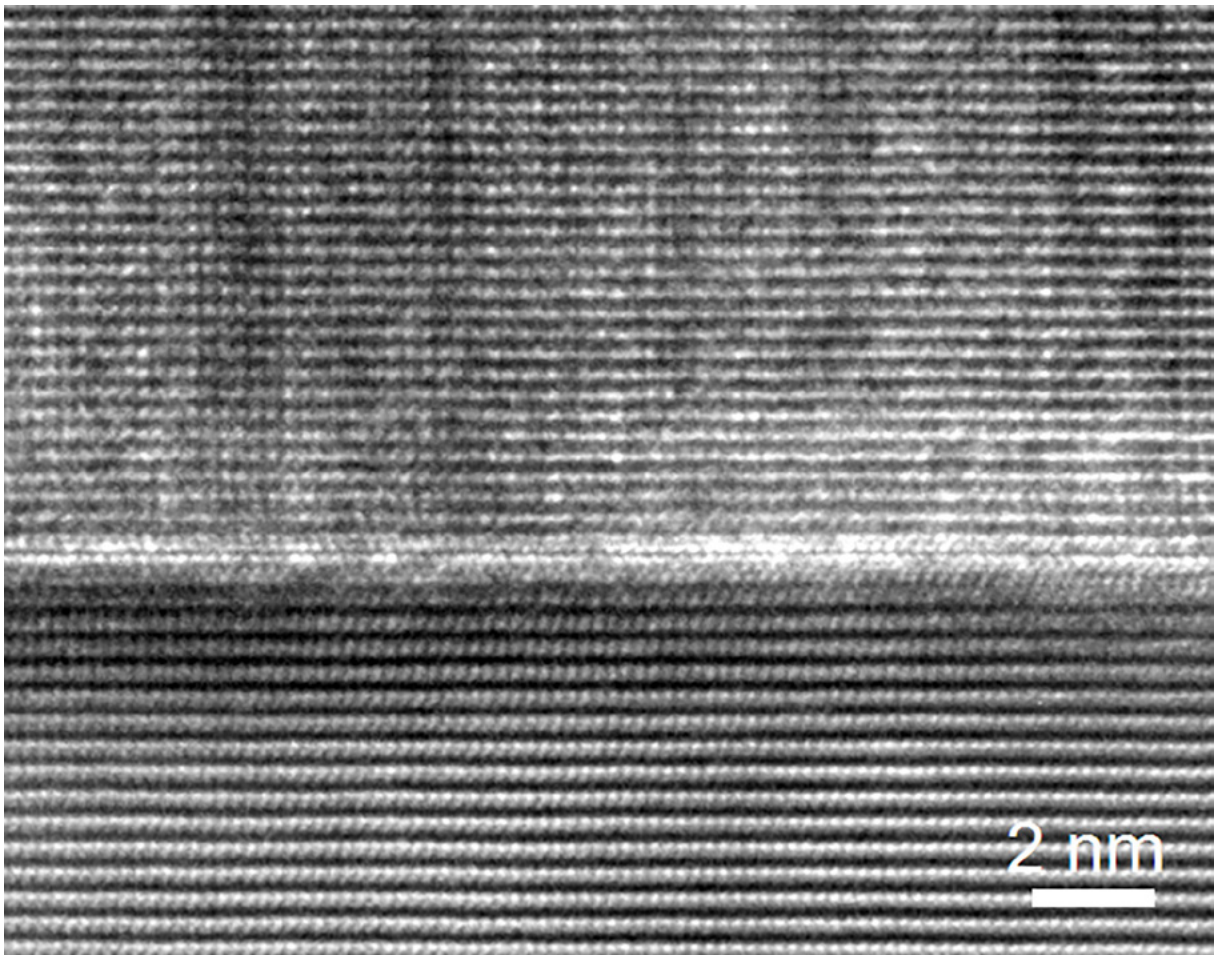

Cross-sectional transmission electron spectroscopy (TEM) of an epitaxial ZrB_2 film deposited on a Al_2O_3(0001) substrate by DCMS from a ZrB_2 compound target 99.5% purity from Kurt J. Lesker Company, Clairton, PA, USA using a laboratory scale ultrahigh-vacuum deposition system. The film was grown to a thickness of ~1100 nm at a substrate temperature of 900 °C with a sputtering power of 400W on the three-inch circular sputtering source and in an argon plasma (99.9997%) held at a 0.53 Pa.

Funding

MM acknowledges financial support from the Swedish Energy Research (no. 43606-1), the Swedish Foundation for Strategic Research (SSF) (no. RMA11-0029) through the synergy grant FUNCASE and the Carl Trygger Foundation (CTS16:303, CTS14:310). LT acknowledges the Swedish Research Council (VR) through the contract 621-2010 3921. GG thanks the Knut and Alice Wallenberg Foundation Scholar Grant KAW2016.0358, the VINN Excellence Center Functional Nanoscale Materials (FunMat-2) Grant 2016-05156, and the Åforsk Foundation Grant 16-359.

LH and HH acknowledge financial support from the Swedish Government Strategic Research Area in Materials Science on Functional Materials at Linköping University (Faculty Grant SFO-Mat-LiU No. 2009-00971).

Publication

M. Magnuson, L. Tengdelius, G. Greczynski, L. Hultman, H. Högberg, Chemical bonding in epitaxial ZrB2 studied by X-ray spectroscopy, Thin Solid Films 649, 2018, 89-96, https://doi.org/10.1016/j.tsf.2018.01.021

The actual electronic band structure of a rubrene single crystal

Organic light emitting diode (OLED) is available on the market and shows that organic molecules can serve as material for fascinating printable and flexible electronic devices. To be able to develop other devices, for example, field-effective transistors and solar cells, understanding the carrier transport mechanism in organic crystals is essential.

The Science

A proper understanding on the charge mobility in organic materials is one of the key factors to realize highly functionalized organic semiconductor devices. So far, however, although a number of studies have proposed the carrier transport mechanism of rubrene (5,6,11,12-tetraphenyltetracene) single crystal (SC) to be band-like, there are disagreements between the results reported in these papers. Here, we show that the actual dispersion widths of the electronic bands formed by the highest occupied molecular orbital (HOMO) are much smaller than those reported in the literature, and that the disagreements originate from the diffraction effect of photoelectron and the vibrations of molecules. The present result indicates that the electronic bands would not be the main channel for hole mobility in case of rubrene single crystal and the necessity to consider a more complex picture like molecular vibrations mediated carrier transport. These findings open an avenue for a thorough insight on how to realize organic semiconductor devices with high carrier mobility.

The Impact

In the present study, we demonstrated that a band-like mechanism observed in transport measurements does not mean that the MO bands are the main channel for carrier transport in case of organic SCs. Taking the difference between the dispersions of the HOMO-derived bands obtained experimentally at room temperature and those obtained theoretically into account, we propose that a more complex picture such as molecular vibrations mediated carrier transport would be the origin of the high carrier mobility in rubrene SC. Thus, this work will open a new avenue to realize organic semiconductor devices with high carrier mobility.

Summary

The state-of-the-art organic-technology, organic light emitting diode (OLED) demonstrates the availability of organic molecules as materials for fascinating printable and flexible electronic devices. However, although a number of powerful organic devices such as organic field-effective transistor and organic solar cell have been proposed, OLED is the only one distributed on the market so far.

One of the most crucial problems for realizing the other organic devices is the low charge carrier mobility in most organic crystals. In order to overcome this problem and to fulfill various organic devices, it is indispensable to have a proper understanding on the carrier transport mechanism in organic crystals, and therefore a lot of endeavor has been devoted to determine the electronic band structures of organic “single” crystals.

Among the organic SCs, rubrene SC is the one whose electronic band structure was most intensively studied due its high hole mobility as reported by transport measurement (40–45 cm^2/Vs).

Nevertheless, despite of the great experimental and theoretical efforts, there is still no complete consensus between the band dispersion and hole mobility, and not even between the experimentally and theoretical dispersions.

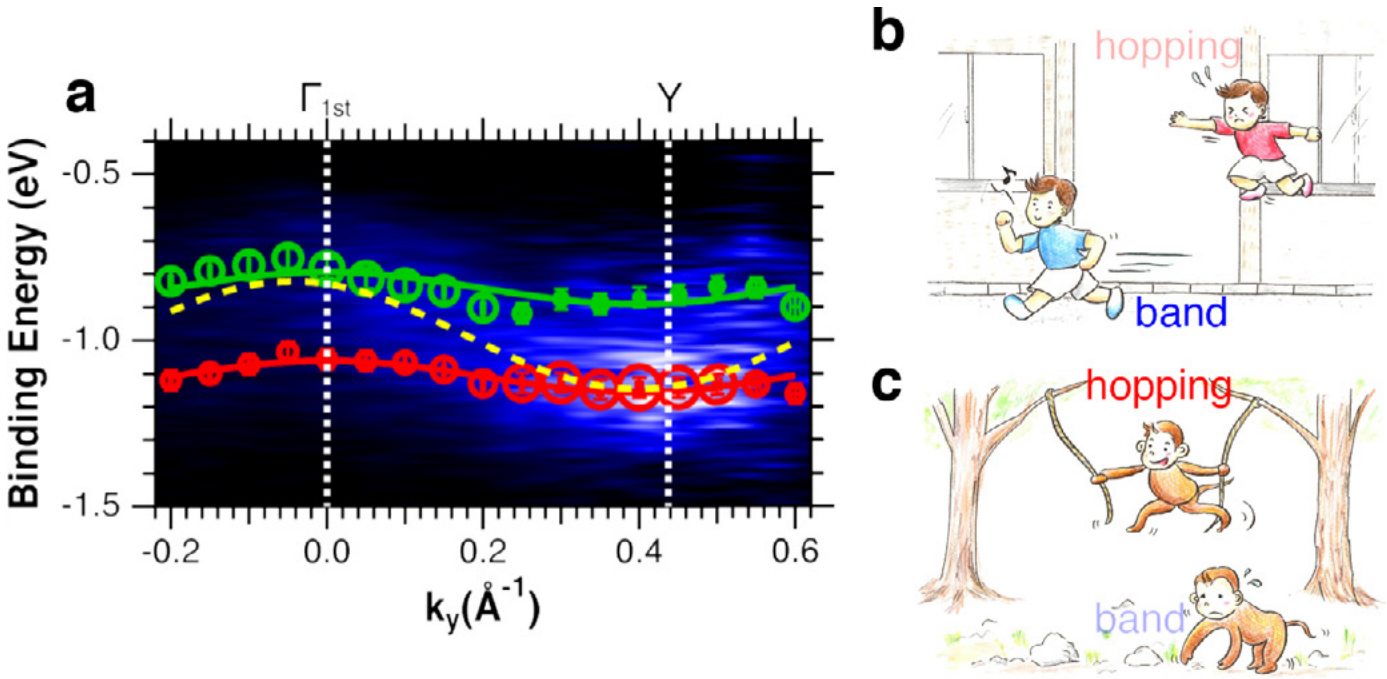

a *Dispersion of the HOMO bands of a rubrene SC. Circles and solid lines are the dispersion obtained in the present study, and the broken line shows the dispersion of the HOMO band that have been consider so far. The obtained results show that different from the case of inorganic crystal, where the high charge mobility results from the band dispersion, the high mobility in organic crystal originates from the flexibility of the molecule. This difference could be understood by changing the "person" to "charge", the "concrete jungle" to "inorganic crystal", the "building" to "atom", "jumping" to "hopping", and "walking" to "passing through a band" in* **b**, *and the "monkey" to "charge", the "forest jungle" to "organic crystal", and the "wood" to "organic molecule" in* **c**.

This means that the carrier transport mechanism in rubrene SC, which is an essential information for designing organic devices with high carrier mobility, is still an unresolved issue.

Theoretical studies reported the presence of two highest occupied molecular orbital (HOMO)-derived bands with strong anisotropy.

We show the HOMO band dispersion of a high-quality rubrene SC obtained using high-resolution ARPES, explain the origin of the contradicted former results by taking the photoelectron diffraction (PED) effect into account, and also discuss the mechanism of carrier transport in rubrene SC.

Funding

This work was supported by the JSPS Grant-in-Aid for Scientific Research (B) 25287070 and 19H02592, JSPS Grant-in-Aid for Scientific Research on Innovative Areas "3D Active-Site Science" 15H01041 and 17H05211, and the JSPS Core-to-Core Program, A. Advanced Research Networks. This work has been partly performed in the framework of the Nanoscience Foundry and Fine Analysis (NFFA-MIUR, Italy, Progetti Internazionali) facility.

Publication

Nitta, J., Miwa, K., Komiya, N. et al.,
The actual electronic band structure of a rubrene single crystal, *Sci Rep* **9**, 9645 (2019). https://doi.org/10.1038/s41598-019-46080-4
Open Access

A study of how graphene can protect copper from oxidising

Graphene has potential as a protective layer for materials, against corrosion by for example moisture or gas. In this study we have used near-ambient-pressure photoemission spectromicroscopy and low energy electron micro-scopy to characterise the coating and its protective role in an operando experiment.

The Science

Graphene, thanks to its hydrophobicity and impermeability to all gas molecules, acts as a protective layer for its supporting substrate. It is resistant to oxidation and can also decouple adsorbed molecular layers from an underlying metal. Being impermeable to liquids and gases and inert to most chemicals, graphene is also widely studied as an anticorrosive coating for metals. Its transparency, conductivity, and intrinsically two-dimensional nature make graphene a perfect candidate that does not affect the morphology of the coated surface.

In this work, we address, in particular, the high-temperature corrosion phenomenon, which is the chemical deterioration of copper as a result of heating in an aggressive (e.g. oxidizing) environment. This form of corrosion is of particular interest for materials used in car engines, power generation, turbines, or other machinery coming in contact with an atmosphere containing corrosive products of combustion at high temperatures.

The Impact

The demonstration that graphene hinders the oxidation of copper in an aggressive environment at high temperatures, whereas bare copper oxidizes already naturally at room temperature, shows the great potential of graphene as a stable protective layer, with only one atom thickness, which retards the formation of copper oxide.

The innovative experimental technique also pushes the limit of standard photoemission spectroscopy, which was traditionally limited to UHV conditions for fundamental studies, and leads the way toward directly studying surface and interface applications under more realistic working conditions.

Summary

We performed spatially resolved near-ambient-pressure photoemission spectromicroscopy on graphene-coated copper in operando under oxidation conditions in an oxygen atmosphere (0.1 mbar). We investigated regions with bare copper and areas covered with mono- and bi-layer graphene flakes, in isobaric and isothermal experiments. The key method in this work is the combination of spatial and chemical resolution of the scanning photoemission microscope operating in a near-ambient-pressure environment, thus allowing us to overcome both the material and pressure gap typical of standard ultrahigh-vacuum X-ray photoelectron spectroscopy (XPS) and to observe in operando the protection mechanism of graphene toward copper oxidation.

The ability to perform spatially resolved XPS and imaging at high pressure allows for the first time a unique characterization of the oxidation phenomenon by means of photoelectron spectromicroscopy, pushing the limits of this technique from fundamental studies to real materials under working conditions. Although bare Cu oxidizes naturally at room temperature, our results demonstrate that such a graphene coating acts as an effective barrier to prevent copper oxidation at high temperatures (over 300 °C), until oxygen intercalation beneath graphene starts from

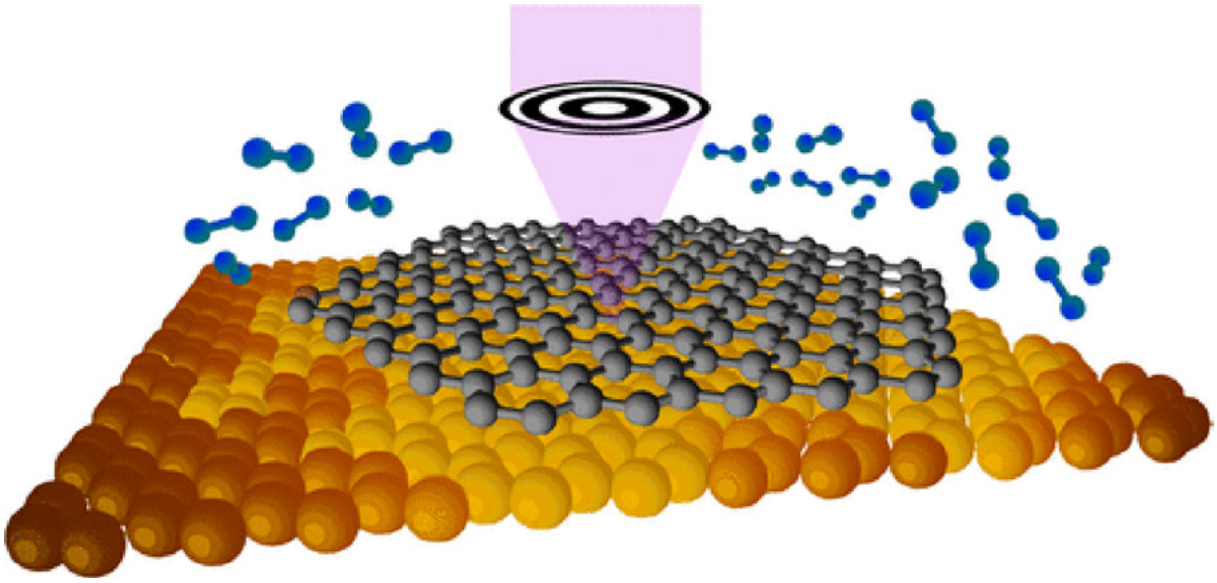

Schematic image of the near-ambient-pressure photoemission spectromicroscopy experiment.

boundaries and defects. We also show that bilayer flakes can protect at even higher temperatures. The protected metallic substrate, therefore, does not suffer corrosion, preserving its metallic characteristic, making this coating appealing for any application in an aggressive atmospheric environment at high temperatures.

In the experiment, we probe in operando the protecting action of graphene on copper by locally investigating the different dynamics of copper under mono- and bi-layer graphene flakes and bare copper regions by means of near-ambient-pressure X-ray photoelectron spectromicroscopy in a molecular oxygen gas environment. Isothermal and isobaric experiments unravel the dynamics of different phenomena involved during the process: (1) the removal of atmospheric contaminants at lower oxygen pressure and subsequently the oxidation of bare copper regions; (2) the intercalation of oxygen under graphene and the oxidation of the copper beneath; (3) the etching of graphene associated with a change in the morphology of the copper oxide. We used the SPEM and the near-ambient-pressure (NAP) cell installed at ESCAmicroscopy beamline (Elettra Synchrotron, Trieste, Italy).

To distinguish different possible physical mechanisms and obtain information on their dynamics, we performed two experiments: (1) isobaric, that is, slowly heating the sample inside the NAP cell up to 390 °C at a constant pressure of 0.1 mbar of O_2; (2) isothermal, that is, increasing the pressure by steps up to 0.1 mbar at a fixed temperature of 350 °C. LEEM and µLEED measurements were performed using the aberration-corrected low-energy electron microscope (Elmitec GmbH) installed at MAXPEEM beamline (MAX IV) to inspect the morphology and the structure of the samples investigated by SPEM.

Funding

The Calipso Programme is acknowledged for financial support. C.S. acknowledges Stiftelsen för Strategisk Forskning (SSF) (Project No. RMA15-0024).

Publication

Reprinted (adapted) with permission from Scardamaglia M, Struzzi C, Zakharov A, Reckinger N, Zeller P, Amati M, Gregoratti L, Highlighting the Dynamics of Graphene Protection toward the Oxidation of Copper Under Operando Conditions, *ACS Appl. Mater. Interfaces* 2019, 11, 32, 29448–29457. Copyright 2019 American Chemical Society https://doi.org/10.1021/acsami.9b08918

Growth and characterization of sidewall graphene nanoribbons for nanoelectronics

High quality graphene nanoribbons (GNR) epitaxially grown on the sidewalls of silicon carbide mesa structures stand as key building blocks for graphene-based nanoelectronics. Here we present a technique for wafer scalable template growth of high quality GNRs on Si-face of SiC(0001) and provide detailed structural information collected at Low Energy Electron and Scanning Tunneling Microscopes (LEEM and STM). This approach generates an entirely new platform for both fundamental and application-driven research of quasi one-dimensional carbon based magnetism and spintronics.

The Science

Sidewall graphene nanoribbons (GNR) display quantum and electronic properties which are entirely defined by their edge termination. Sidewalls aligned parallel to the [11-20] SiC direction are composed of a periodic array of mini-terraces hosting several ~3 nm wide armchair terminated GNRs (ac-GNRs) at their step edges. Such narrow, one-dimensionally (1D) confined nanoribbons demonstrate a width-dependent bandgap in their electronic structure, the property which can be utilized in the field-effect graphene transistors. Sidewalls aligned parallel to the [1-100] SiC produce ~40 nm wide free-standing zigzag graphene nanoribbons (zz-GNRs). Epitaxial zz-GNRs demonstrate 1D single-channel ballistic transport at room temperature with exceptionally long electronic mean free paths.

The Impact

Theoretical predictions, such as tunable band gaps in ac-GNRs, and the existence of topologically protected metallic states located at the zigzag edges, make them a potential candidate for transistor applications as well as a new class of fully coherent devices.

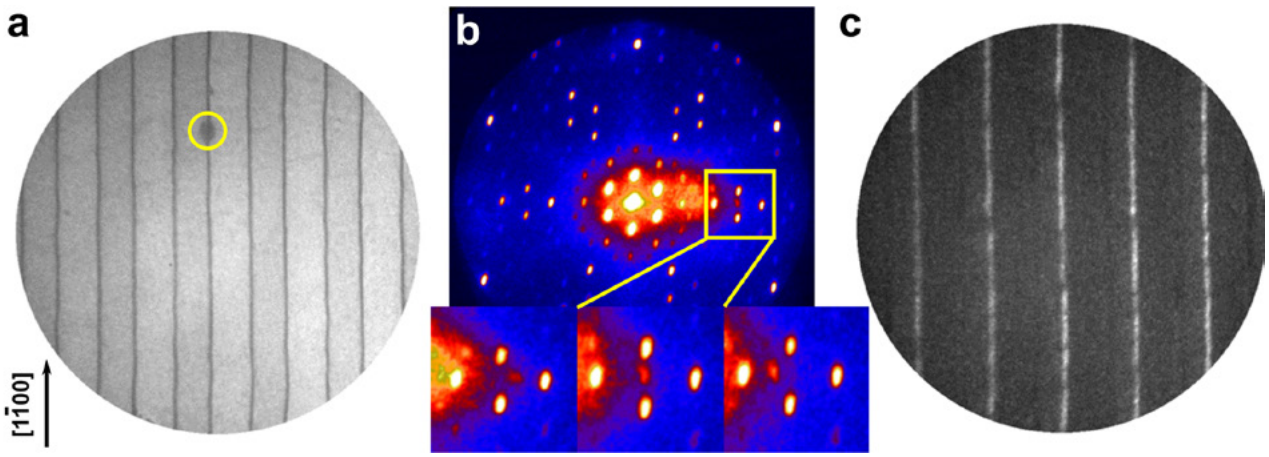

Fig.1. a) Bright field LEEM image (FoV=10µm, E=5eV), yellow circle marks the sampling area (400nm) for the micro-LEED from a single mesa wall; b) m-LEED pattern (E=25.5eV) from a single mesa wall. Insets in the bottom (E=25eV, 25.5eV and 26eV from left to right, correspondingly) show a moving facet spot chosen for dark-field imaging; c) LEEM DF image (E=25.5eV) highlighting graphene nanoribbons on every second wall of the mesa structure.

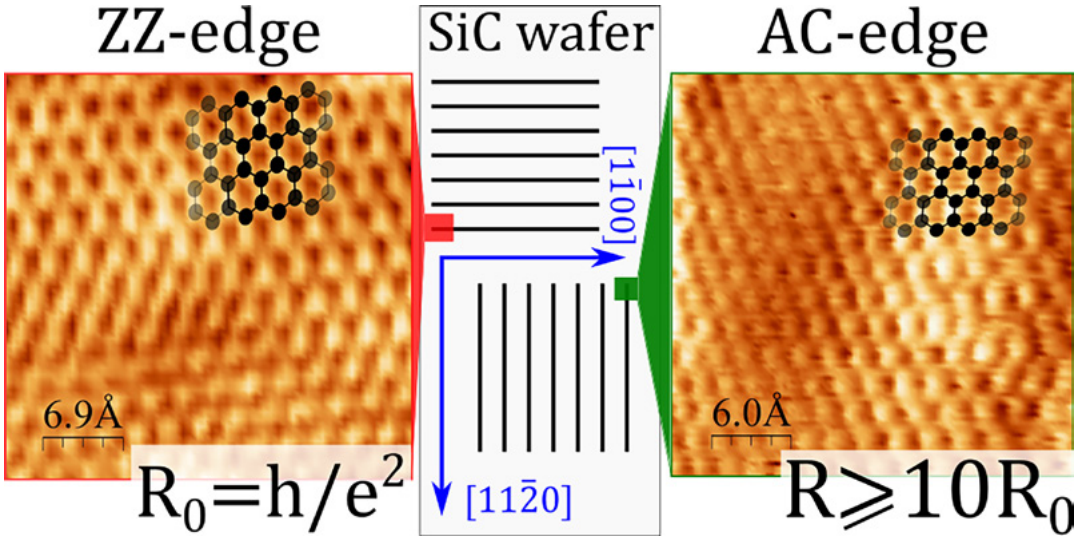

Fig.2. High-resolution STM micrographs of GNRs oriented along [1-100] and [11-20] directions (left and right, respectively). The schematics in the center shows the orientation of the GNRs, the atomic ball-and-stick model of the GNR is shown as an inset in top-right of both left and right panels. FoV is ~ 4 nm in both images.

Summary

LEEM and micro-LEED studies were performed at an aberration-corrected low energy electron microscope (Elmitec GmbH) installed at MAXPEEM beamline. Scanning tunneling microscopy data were collected using a commercial VT XA STM (Scienta-Omicron), installed at SPM lab, MAX IV Laboratory. To quantify topologically the side wall graphene, a dark field LEEM mode was used. As an example, Fig.1 shows a sequence of experimental steps for dark field LEEM imaging of zz-GNRs.

To further characterize GNRs in both orientations, STM measurements were performed both on zz and ac nanoribbons. The STM studies have confirmed the formation of high-quality, defect-free graphene on the faceted mesa walls, and verified the different orientation of zz- and ac-GNRs, leading to a different edge termination.Conductance measurements reveal ballistic transport for the zz-GNRs (R0=h/e2) and dielectric behavior for the ac-GNRs as a result of the quantum confinement in very narrow graphene nanoribbons.

In summary, our results demonstrate that free standing graphene grows on the faceted mesa walls for both crystallographic directions of the SiC(0001) substrate (ac-GNRs and zz-GNRs). The quality of the graphene nanoribbons is exceptional, they can be grown on the wafer scale and applied in graphene electronics.

Funding

Research conducted at MAX IV is supported by the Swedish Research Council as Swedish partner of the TAILSPIN project in the frame of European FLAG-ERA project.

Publications

Reprinted (adapted) with permission from Zakharov A.A., Vinogradov N.A., Aprojanz J. et al., Wafer Scale Growth and Characterization of Edge Specific Graphene Nanoribbons for Nanoelectronics, *ACS Appl. Nano Mater.* 2019, 2, 1, 156–162. Copyright 2019 American Chemical Society
https://doi.org/10.1021/acsanm.8b01780
Johannes Aprojanz et al., Ballistic tracks in graphene nanoribbons, *Nat. Commun.* **9**, 4426 (2018). Open Access
https://doi.org/10.1038/s41467-018-06940-5

Connecting structure and conductivity change of vanadium dioxide

Vanadium dioxide can change its conductivity up to four orders of magnitude. This makes the material of interest for electronic devices. In this paper, spectromicroscopy performed at MAXPEEM sheds new light on the mechanism behind the transition.

The Science

Emergent order at mesoscopic length scales in condensed matter can provide fundamental insight into the underlying competing interactions and their relationship with the order parameter. Using spectromicroscopy, we show that mesoscopic stripe order near the metal-insulator transition (MIT) of strained VO_2 represents periodic modulations in both crystal symmetry and V—V dimerization. Above the MIT, we unexpectedly find the long-range order of V—V dimer strength and crystal symmetry become dissociated beyond ≈200 nm, whereas the conductivity transition proceeds homogeneously in a narrow temperature range.

The Impact

Bulk VO_2 at low temperature exists in a strongly dimerized (between neighboring V ions) and insulating monoclinic structure (the M1 phase), which transitions to the high symmetry tetragonal rutile (R) phase at 65 °C concomitant with a huge change in the conductivity of 4 orders of magnitude. The advantageous properties of this transition have placed VO_2 at the forefront of exploitable new technologies.

Summary

Recent observations of the separation of the electronic and structural transitions of vanadium dioxide (VO_2) have shed new light on the microscopic mechanism of the metal-insulator transition (MIT) of this exemplar MIT material.

The coincidence of large structural and electronic transitions precludes the unambiguous untangling of the mechanism behind the transition, which has led to decades of debate as to whether the MIT is driven by structural instabilities towards dimerization or as a consequence of the effects of strong electron correlation. In this context, the details of the low symmetry monoclinic like metallic phase(s) that develop intermediately between M1 and R offer a unique and crucial insight into these questions.

Here, we employ spatially resolved x-ray absorption spectroscopy (XAS) by imaging the secondary electron yield using photoemission electron microscopy (XPEEM) in concert as a spectromicroscopic technique (XASPEEM), which we apply in detail to the intermediate region of the MIT.

In summary, we find that the M1 VO_2 is quickly destroyed on heating and is replaced by an insulating monoclinic phase that gradually separates into strongly and weakly paired dimers that are coupled to the underlying symmetry of the crystal structure. The electronic transition occurs over a narrow temperature range within this structural evolution, giving way to a monocliniclike metallic phase that still contains bimodal dimer pairing and symmetry. The continuous weakening of the structural distortion eventually establishes the rutile phase. These details are inconsistent with a structural MIT model, depending instead on the effects of strong electron correlation.

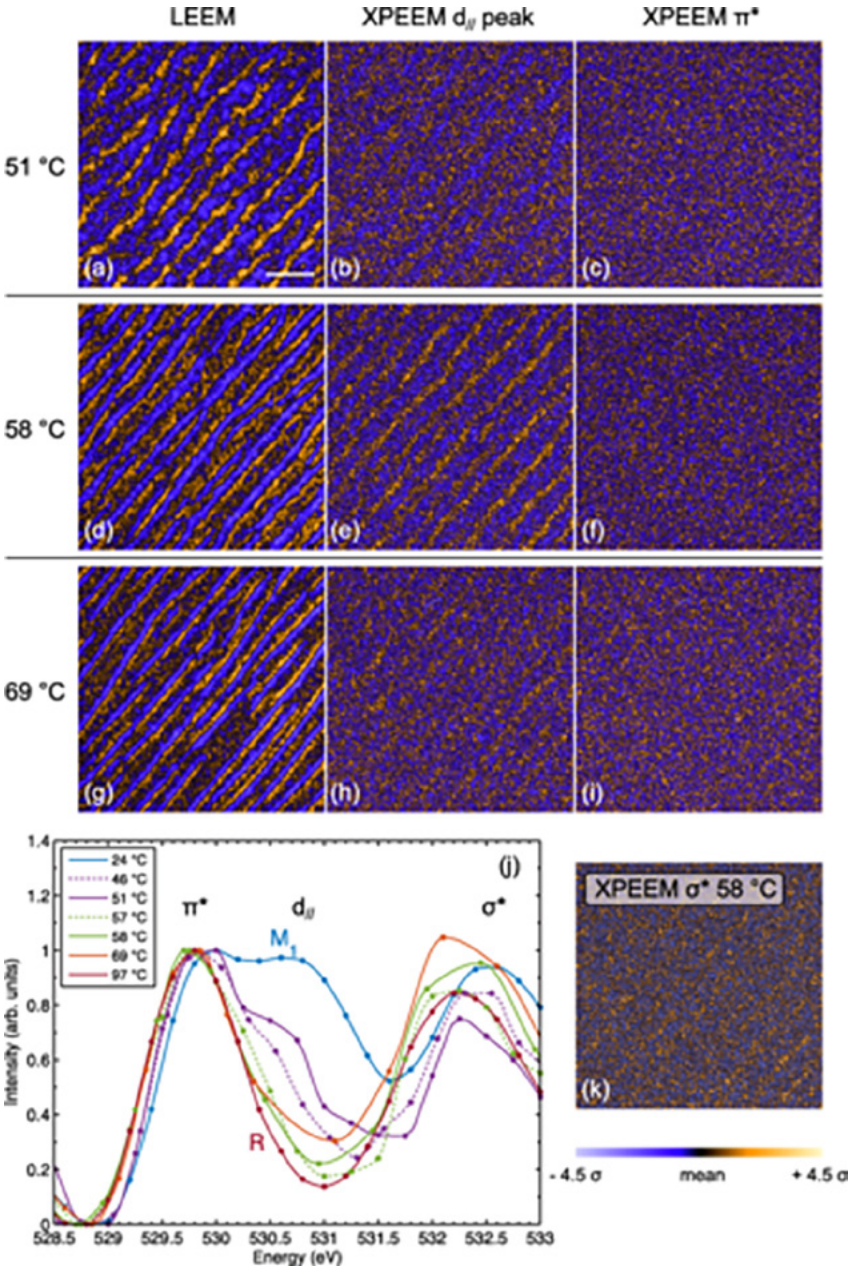

LEEM and XASPEEM images of VO_2(110) at select temperatures through the MIT. (a)–(c) 51 °C. (d)–(f) 58 °C. (g)–(i) 69 °C. At each temperature, three images are shown: LEEM, XPEEM at the d‖ photon energy (531 eV), and XPEEM at the π photon energy (529.7 eV). (j) Spatially averaged O K edge XAS obtained by integrating the energy-dependent XASPEEM images over their field of view (approximately 100 μm2). (k) Example at 58 °C of the recovery of XPEEM image contrast at the σ* absorption feature (532.5 eV). The color scale of each image is normalized to ±4.5σ from the mean LEEM or XPEEM (d‖) values. Scale bar: 1 μm.*

Funding

The Boston University program is supported in part by the Department of Energy under Grant No. DE-FG02-98ER45680. S.K., J.W.L., and S.A.W. gratefully acknowledge financial support from the Army Research Office through MURI Grant No. W911-NF-09-1-0398. J.L. acknowledges the EPSRC Centre for Doctoral Training in Condensed Matter Physics (CDT-CMP), Grant No. EP/L015544/1. Calculations were performed using the computational facilities of the Advanced Computing Research Centre, University of Bristol.

Publication

J. Laverock, V. Jovic, A. A. Zakharov, Y. R. Niu, S. Kittiwatanakul, B. Westhenry, J. W. Lu, S. A. Wolf, and K. E. Smith, Observation of Weakened V—V Dimers in the Monoclinic Metallic Phase of Strained VO2, Phys. Rev. Lett. **121**, 256403
https://doi.org/10.1103/PhysRevLett.121.256403
Open Access

Metallic contact between MoS2 and Ni via Au nanoglue

Inorganic layered crystals, such as molybdenum disulphide are promising candidates for future electronics. The challenge is to make functional contacts to these materials. This study shows a route towards using nickel contacts and a gold buffer, a so called nanoglue. The resulting contacts have been thoroughly characterised with several methods including synchrotron radiation-based photoemission electron microscopy at the PEEM end station of beamline I311 at MAX II.

The Science

Since the rediscovery of monolayer graphene, exploration and manipulation of layered crystal properties have become a research focus in materials science. Composed of intralayer covalent bonds and interlayer van der Waals interactions, the transition metal dichalcogenides (TMDs) are featured as typical inorganic layered crystals (ILCs). Distinct from the gapless graphene and insulating hexagonal boron nitride (h-BN), many TMDs exhibit semiconducting and layer-dependent band structures, and thus are considered as promising candidates for future electronics. However, the quality of electrical contact between the ILCs and metals, is of crucial importance to ensure the performance of the entire electronics.

Compared with well-established Group IV semiconductors, effective contacts in ILC-metal systems are rather difficult to achieve, especially in low dimensions. In this work, we report a materials engineering method via nanocomposite decoration as an efficient and inexpensive way to glue NiNPs to the MoS2.

The key recipe of the synthesis relies on introducing Au nanoglue from chloroauric acid. Through such synthesis, Ni–Au–MoS2 contact is established with a greatly reduced contact resistance. The synthesized complexes preserve the semiconducting character of the MoS2 host and the ferromagnetism of Ni. Microscopic and spectroscopic determination from synchrotron-based X-ray photoemission electron microscopy (XPEEM) verified the successful bonding of Ni to the layered MoS2 at the nanoscale interface regions.

The Impact

A critical factor for electronics based on inorganic layered crystals stems from the electrical contact mode between the semiconducting crystals and the metal counterparts in the electric circuit. In this study, a materials tailoring strategy via nanocomposite decoration is carried out to reach metallic contact between MoS2 matrix and transition metal nanoparticles.

We show that gluing properly selected nanocomposites to the ILCs may provide a general route for transferring the properties of the guest materials to the functionalized host materials, simultaneously reaching metallic contact between the two sites, and improving chemical robustness of the layered hosts.

Summary

Nickel nanoparticles (NiNPs) are successfully joined to the sides of a layered MoS2 crystal through gold nanobuffers, forming semiconducting and magnetic NiNPs@MoS2 complexes. The intrinsic semiconducting property of MoS2 remains unchanged, and it can be lowered to only few layers. Chemical bonding of the Ni to the MoS2 host is verified by synchrotron radiation based photoemission electron microscopy, and further proved by first-principles calculations. Following the system's band alignment, new electron migration channels between metal and the semiconducting side contribute to the metallic contact mechanism, while semiconductor–metal heterojunctions enhance the photocatalytic ability.

With the proposed synthesis method, an ef-

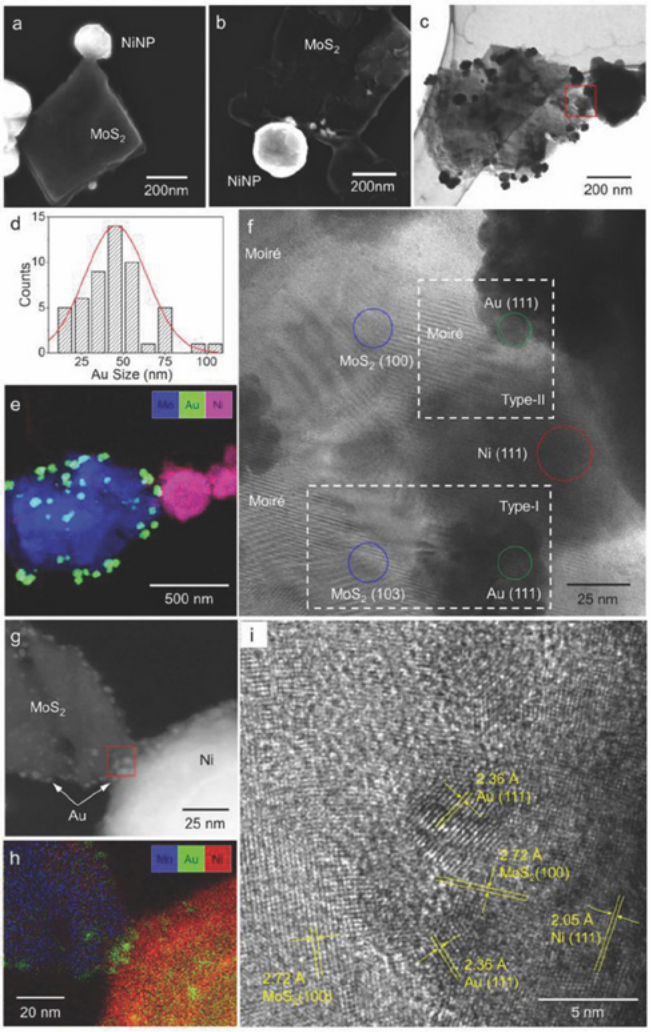

Morphologies of MoS2–Ni complexes glued by Au nanoparticles.
a) Scanning electron microscope (SEM) image shows a well-shaped MoS2 flake with a Ni nanoparticle on the edge.
b) SEM image taken after 50 times of mechanical exfoliation.
c) TEM image.
d) Histogram of Au nanoparticle size distribution in (c).
e) TEM-EDS mapping.
f) HRTEM of the square region shown in (c). The lower and upper rectangles in dashed line denote the type-I and type-II interfaces, respectively.
g) Dark field TEM image showing Au nanoparticles in a smaller size.
h) TEM-EDS mapping.
i) HRTEM of the square region shown in (g).

fective metallic contact is established between MoS2 and NiNPs, introducing ferromagnetic and enhanced photocatalytic properties. Samples both in suspension and in dry powder form are feasible to prepare, thus suitable for industrial production. Endowed with magnetic attribute, such TMDs provide high potential for innovation in semiconductor industry and provide a series of candidates for chemical catalysts. The synthesis route was also proven efficient in joining different TMDs to NPs. The growth mechanism was explicated in first-principles calculations. Through the present experimental evidence and theoretical clarifications, the side contact model was realized. Further investigations may also pay attention to targeted doping to particular positions of semiconductor layers and extend the present method to synthesize ILC-based materials for specific needs.

Funding

The authors acknowledge financial support from Strategic Grant of University of Oulu, Academy of Finland, National Natural Science Foundation of China (Grant No. 11204079), and the Natural Science Foundation of Shanghai (Grant No. 12ZR1407000). W.C. and M.H. acknowledge the European Regional Development Funding and the Oulu Council. X.S. acknowledges the scholarship sponsored by China Scholarship Council. J.H., J.-Cl.D., and F.Z. acknowledge the financial support of the Swiss National Science Foundation (Grant No. 200020_146739).

Publication

Shi X., Posysaev S., Huttula M., *et al*. Metallic Contact between MoS2 and Ni via Au Nanoglue. Small (2018) **14** 1704526 Copyright Wiley-VCH GmbH. Reproduced with permission.
https://doi.org/10.1002/smll.201704526

Growth and characterizations of high quality multilayer graphene for electronic devices

Multilayer graphene is a candidate for future electronics. The electronic properties depend on stacking and uniformity of the layers. In these two joint works through a collaboration between researchers at Linköping University (LiU) and MAX IV, beamline MAXPEEM, is used to characterize the graphene layers grown on a cubic silicon carbide (3C-SiC) surface.

The Science

Graphene with several layers stacked on top of each other, so called multilayer graphene, is a material with attractive electronic properties such as a tunable bandgap and it exhibits several exotic properties. The utilisation of multilayer graphene in devices depends on the level of control of material growth process.

The electronic band structure and therefore the properties of multilayer graphene depend on the stacking of its layers. The ABCA type stacking sequence, called rhombohedral stacking, is thought to give rise to a flat band structure. It may result in effects such as superconductivity, and fractional quantum Hall effect.

A common and promising way of growing graphene is through thermal decomposition of silicon carbide, SiC. The challenge is to control uniformity over a large area and avoid step bunching on surface.

In the two studies presented here, low energy electron microscopy (LEEM) at the MAXPEEM beamline was used to examine the layer stacking and quality of the grown graphene layers. This is a way to connect growth parameters with resulting structure.

The Impact

If the growth of multilayer graphene can be optimised and controlled to manufacture desired properties, it will be applicable in new types of electronic devices.

In the studies presented here, the LEEM is used to characterise the graphene layers epitaxially grown on SiC. The resulting material can be reliably associated with the growth parameters used. Step-bunching free, large-area mono-, bi- and four-layer graphene layers have been achieved.

Summary

Monolayer and multilayer graphene were grown on off-axis 3C-SiC(111) by researchers at LiU and the layer thickness and uniformity were studied by LEEM.

With using the off-axis 3C-SiC(111), the authors show that the periodic step edges of the 3C-SiC exhibit the unique thermal decomposition energy and step bunching can be eliminated. The LEEM results confirm that the graphene is uniformly grown over tens of square micrometers.

LEEM imaging was also used to confirm the number of layers and the stacking sequence. It could be connected with the angle-resolved photoelectron spectroscopy (ARPES) data, revealing the band structure, of the samples. The authors show that a rhombohedral stacking sequence gives rise to a nearly dispersionless electronic band (flat band) near the Fermi level. Moreover, it was found that the interlayer spacing can be used to tune the momentum width, band gap and curvature of the flat-band region.

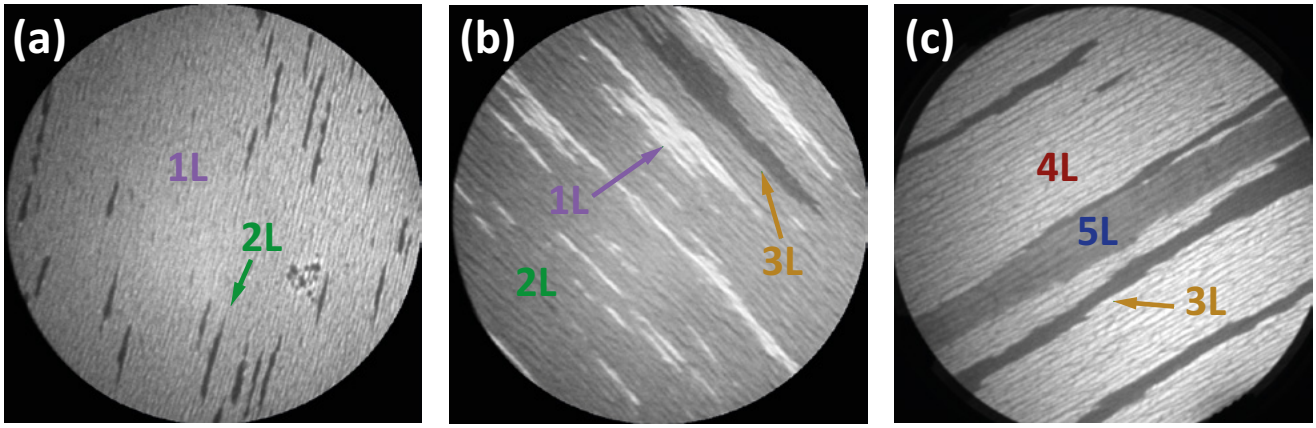

LEEM measurements of graphene grown on 3C-SiC(111). (a–c) LEEM images of graphene samples grown at 1800 °C for (a) 15 min, (b) 30 min, and (c) at 2000 °C for 30 min, measured with an electron energy of 5.48, 5.88, and 2.89 eV at a field of view of 10, 15, and 10 µm, respectively. (d–f) Electron reflectivity curves extracted from the labeled areas in (a–c). The number of minima in an electron reflectivity curve indicates the number of graphene layers.

Funding

[1] The Swedish Research Council (Grant No. 621-2014-5461, 621-2014-5825), The Swedish Research Council for Environment, Agricultural Sciences and Spatial Planning (Grant No. 2016-00559), The Swedish Foundation for International Cooperation in Research and Higher Education (Grant No. CH2016-6722), ÅForsk Foundation (Grant No. 16-399), and Stiftelsen Olle Engkvist Byggmästare (Grant No. 189-0243): R.Y and M.S acknowledge the support by EU project CHALLENGE (720827).
[2] Financial support was provided by the Swedish Research Council (Contract No. 621-2014-5461, No. 621-2014-4764, and No. 621-2014-5805), the Swedish Research Council for Environment, Agricultural Sciences and Spatial Planning (Grant 2016-00559), the Swedish Foundation for International Cooperation in Research and Higher Education (Grant CH2016-6722), ÅForsk foundation (Grant 16-399), and Stiftelsen Olle Engkvist Byggmästare (Grant 189-0243).

Publication

[1] Shi Y., Zakharov A.A., Ivanov I.G., Yazdi G.R., Jokubavicius V., Syvajarvi M., Yakimova R., Sun J. Elimination of step bunching in the growth of large-area monolayer and multilayer graphene on off-axis 3C-SiC (111), CARBON 140 533-542 (2018) https://doi:10.1016/j.carbon.2018.08.042

[2] Wang W., Shi Y., Zakharov A.A., Syvajarvi M., Yakimova R., Uhrberg R., Sun J. Flat-Band Electronic Structure and Interlayer Spacing Influence in Rhombohedral Four-Layer Graphene, *Nano Lett.* 18 5862-5866 (2018), https://doi:10.1021/acs.nanolett.8b02530

Borophene – a new, exciting 2D material

Borophene is a two-dimensional layer of boron atoms, named by analogy to a famous graphene. Unlike its carbon-based relative, borophene may possess a variety of structures due to the existence of hexagonal holes in its structure. These holes stabilize the borophene layer, and their number and motif determine its properties. Recently we were able to synthesize an unusual borophene on iridium surface.

The Science

Not so long ago, graphene was proclaimed a new wonder-material thanks to its outstanding mechanical, chemical, and electronic properties. While mass-production of graphene-based devices is yet to come true, the extensive research within one-atom-thick materials has helped to discover a few other "flatlands": silicene, germanene and borophene (one-atom-thick sheets of silicon, germanium and boron).

The Impact

For this reason, borophene has been at the cutting edge of contemporary research in the last few years. Discovered experimentally in 2015, borophene was mainly studied on Ag(111), until recently, when several other metals have been shown to be suitable for hosting 2D boron layers.

Amongst them are gold, aluminium and copper, however, some controversy remains regarding the structure and composition of boron overlayers. As for borophene on (111) face of silver, it forms as a mixture of several different phases, and fine tuning of the borophene preparation conditions suppresses but unfortunately does not stop the formation of one or another phase.

As the physical properties of these phases are intrinsically different, their co-existing hindered the practical implementation of this material. Therefore, our discovery of stable single-phase borophene on Ir(111) is a major step towards unleashing the borophene's potential.

Summary

Borophene is particularly interesting because it is believed to be even stronger than graphene while maintaining many of its outstanding properties: excellent heat and electricity conductivity. However, heat and electricity conductivity are not the only borophene' strengths making it so important to study.

Unlike carbon atoms in graphene, which must be bound to four neighbours, boron atoms in two-dimensional borophene sheets may be bound to three, four, five or six neighbours, which creates a periodic motif of vacancies or hexagonal (by a number of neighbours) holes in the flat sheet of boron. It is the number of these hexagonal holes and the motif of their positions in the lattice that mostly define the properties of a specific borophene.

In this manuscript, we discover a novel structure of borophene and report an original approach to its synthesis involving bottom-up fabrication and control of boron self-organization on iridium single-crystal substrate. We demonstrate that truly two-dimensional borophene does grow on iridium and appears in only one stable structural phase in a wide range of growth temperatures.

Moreover, we reveal the exact atomic arrangement of this complex borophene phase – its structure is found to be different from all known B polymorphs – and provide a simple recipe for its formation.

Furthermore, we prove the integrity and stability of the borophene layers per se by lifting them off the substrate via gold intercalation. This

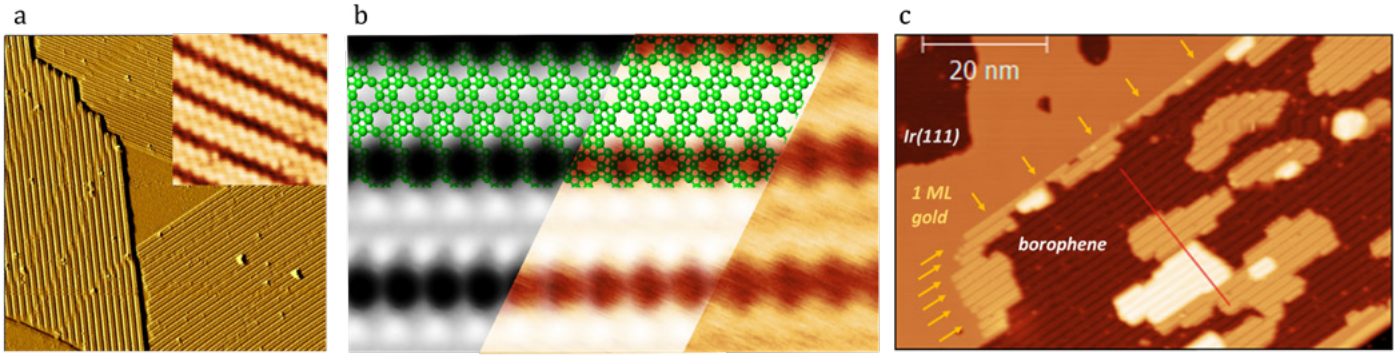

Borophene on Ir(111). a, survey STM micrograph (FOV ~ 100 nm) of borophene on Ir(111), showing three orientation domains. Inset in top-right corner shows a high-resolution STM close-up on one of the domains (FOV ~ 5 nm). b, theoretically modeled STM image (greyscale) overlaid on experimental data (yellow-red). On top there is a theoretical ball-and-stick atomic model of borophene/Ir. c, STM image of borophene intercalated with ~ 1 ML of gold. An intercalation front is clearly visible (marked with arrows).

opens a route for transferring borophene onto other substrates after synthesis for use in e.g. electronic devices.

In summary, we have demonstrated that a single phase borophene can be formed on Ir(111) substrate by direct exposure to a flux of B atoms at a wide range of elevated temperatures. According to the existing terminology, this is a χ6-type borophene, with a HH density parameter η = 1/6 and boron atom density of 0.326 Å–2. Based on combined LEED, dynamic STM studies, and DFT calculations, we propose the exact atomic arrangement of this structure. Our experiments with decoupling borophene from Ir substrate via intercalation suggest that this type of borophene must be stable at RT on low-binding substrates.

From the practical point of view, the most appealing properties of χ6 borophene are the ease and reproducibility of preparation in combination with a well-defined and single-phase structure of the final borophene layer. On the other hand, an important difference from other known borophene structures comes from the presence of relatively active underlying Ir surface, which makes the electronic relief along the borophene sheet highly uneven. We foresee that the adjacent borophene sites with opposite electron doping might exhibit catalytic activity or facilitate highly regular adsorption of large molecules, metal clusters, and other objects interesting for catalysis, sensors, and nanotechnology.

Funding

N.A.V. and A.B.P. gratefully acknowledge Swedish Research Council and Carl Trygger's Foundation for the financial support. A.L. and T.T. are grateful for financial support from the program of the Ministry of Education, Culture, Sports, Science, and Technology (MEXT, Japan) "Priority Issue on Post-K computer" (Development of new fundamental technologies for high-efficiency energy creation, conversion/storage and use). Institute for Chemical Reaction Design and Discovery (ICReDD) was established by World Premier International Research Initiative (WPI), MEXT, Japan. The computations were partly performed at the Research Center for Computational Science, Okazaki, Japan and the Numerical Materials Simulator, NIMS, Tsukuba, Japan.

Publication

Vinogradov N. A., Lyalin A., Taketsugu T., Vinogradov A. S., Preobrajenski A., Single-Phase Borophene on Ir(111): Formation, Structure, and Decoupling from the Support, *ACS NANO* **13** (2019) 14511-14518
https://doi.org/10.1021/acsnano.9b08296

Small catalyst-like nonoparticles can be imaged in situ

The Bragg Coherent Diffraction Imaging (BCDI) technique is expected to provide new insights into catalysic processes occuring on the surfaces of nanoparticles. Currently, a gap in particle sizes exists between what can be imaged and what is used in industrial applications. The X-ray source at MAX IV pushes the size limit of the BCDI technique. The researchers demonstrate imaging of 60 nm particles inside an electrochemical cell and estimates that 15 nm particles can realistically be studied.

The Science

Catalysis in electrochemical systems is crucial for a number of industrial applications in energy transduction, chemical production and water purification. While much can be learned from pure electrochemical studies, sometimes combined with scanning probe or spectroscopic techniques, direct nanoscopic visualization of when and where catalytic processes occur is lacking. Bragg Coherent Diffraction Imaging (BCDI) is one option for mapping catalytic reactivity across nanoparticle surfaces and studying these chemical dynamics in new detail.

The Impact

While there are numerous successful applications of in-situ BCDI published, there is a gap in particle sizes between the particles that can be imaged at third generation synchrotron sources (>100 nm) and particles typically used in real catalytic applications (<10 nm). This divide can be overcome by exploiting the new generation of Diffraction-Limited Storage Rings (DLSR:s), which provide unprecedented coherent flux densities on the sample. By imaging particles of 60 nm under potential control in an electrochemical cell, this paper shows for the first time that DLSR:s can push the limits of this coherent imaging technique, paving the way for investigations of real catalytic systems.

Summary

The work was carried out at the NanoMAX hard X-ray nanoprobe beamline, where X-rays are focused in a diffracted-limited manner with curved mirrors to achieve an intense focal spot around 100 nm wide. The experimental station features a two-circle goniometer and a pixel detector mounted on an industrial robot arm. This allows flexible BCDI measurements in different geometries. A custom three-electrode cell was developed (Fig. 1) which gives access to electrically contacted nanoparticles and allows the coherent diffraction patterns to exit the cell and reach the pixel detector.

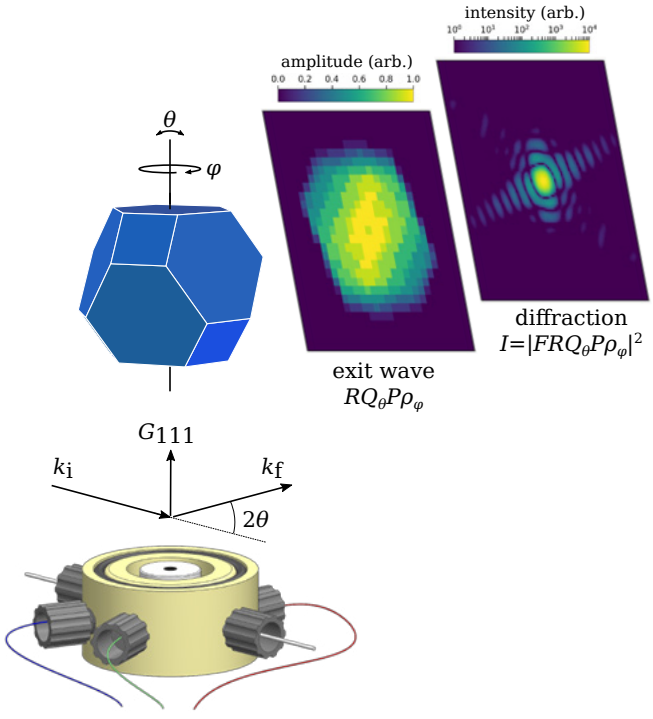

Fig. 1. Experimental geometry showing the electrochemical cell and a model particle with simulated data.

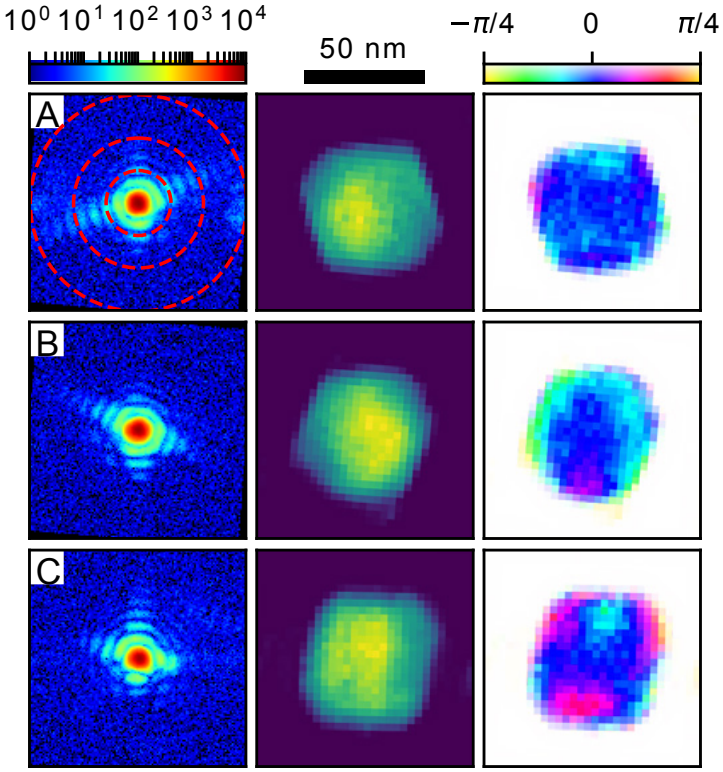

Fig. 2. Reconstructed particles in shape and amplitude.

Truncated-octahedral nanoparticles of gold were used as model particles. These were well-controlled in shape and size as measured with Transmission Electron Microscopy (TEM), and supported by a conductive carbon matrix commonly used in catalysis applications, which also ensures that they are isolated.

Coherent diffraction patterns were found and recorded by scanning an Au-C deposit through the focused beam. The experiment was not limited by coherent flux, but by instability of the particles under the intense radiation. It is a known problem, related to the angular sensitivity of all measurements in the Bragg geometry, that particles rotating because of local heating and/or radiation pressure can limit BCDI data collection. The original aim of the experiment was to record three-dimensional data by performing controlled scans of the diffraction angle.

Because of the observed instability, the acquisition strategy was changed. Instead of aiming for three-dimensional data, two-dimensional data were recorded by arbitrary scanning, selecting the brightest chance hits.

Figure 2 shows examples of diffraction patterns together with the reconstructed (phase-retrieved) real-space particle images. The images are projections in the direction of the diffracted beam, and show particle shapes which closely match what is expected from TEM. Recurring phase patterns were found, but are not analyzed further as they are difficult to interpret in two dimensions.

Based on these results, the possibility of imaging realistic catalysts was assessed. Assuming that the stability issues are solved or accounted for, and that sufficient long-term stability is ensured, it is estimated that full three-dimensional data from particles as small as 15 nm could be recorded in 45 minutes, considerably improving the current limits of BCDI.

Funding

This work was supported by the ÅForsk Foundation through grant 17-408. JS-G acknowledges financial support from VITC (Vicerrectorado de Investigación y Transferencia de Conocimiento) of the University of Alicante (UATALENTO16-02).

Publication

Björling, A., Carbone, D., Sarabia, F. J., Hammarberg, S., Feliu, J. M., and Solla-Gullón, J., Coherent Bragg imaging of 60 nm Au nanoparticles under electrochemical control at the NanoMAX beamline, *J. Synchrotron Rad.* **26**, 1830 (2019). Reproduced with permission of the International Union of Crystallography
https://doi.org/10.1107/S1600577519010385

Low Density Matter Science at MAX IV

Research investigating the interaction of light with molecules, clusters and liquids/aqueous solutions enables a fundamental understanding of the properties of these samples, as well as an understanding of various processes that occur in nature, or that are relevant to industrial and technological development. For example, research within molecular/cluster science can provide insight into photoreactions that take place in Earths' upper and lower atmospheres – reactions relevant to climate and cloud formation. Clusters also play a role in many technological applications. The investigation of UV-radiation damage in biological molecules/small clusters affords a better understanding of certain UV-induced physical/chemical processes that can have an adverse influence on human health. Studies on liquids/aqueous solutions are relevant to the development of various technological advancements as well as to a better understanding of atmospheric and environmental sciences. For example, the study of electrolytes used in dye-sensitized solar cells and the determination of the surface properties of aqueous solutions of relevance to atmospheric chemistry.

Over the last decades, Low Density Matter science has proven to be a highly productive research area at MAX-lab – utilizing experimental techniques such as photoelectron spectroscopy, molecular jet/cluster beam generation and liquid micro jet generation. At MAX IV laboratory, we continue to offer the availability of such staple techniques; however, we are also committed to expanding our LDM equipment portfolio – developing new experimental capabilities to complement the established techniques – new methods for sample generation and characterisation - in collaboration with our user community.

MAX IV currently has six LDM-relevant beamlines (FinEstBeAMS, FlexPES, Veritas, HIPPIE, SPECIES and FemtoMAX) that together deliver photons over a broad photon energy range. Whilst none of these beamlines caters solely to gas phase/liquid jet research, these beamlines have branches or end stations that can/will facilitate low-density matter research covering such topics as:

- Photo-induced molecular/cluster fragmentation and ionization processes
- Electron correlations
- Electronic and/or nuclear dynamics in molecular/cluster systems
- Site-selective photo-chemistry/fragmentation
- Coulomb explosion reactions and charge-transfer processes in molecules/clusters
- Photochemistry of molecules that play a role in atmospheric chemistry
- Surface properties of liquids and aqueous solutions
- Properties of hydrogen-bonded systems
- Properties of ionic liquids

Experimental techniques available at MAX IV:

- High-resolution photoelectron spectroscopy and angle resolved electron spectroscopy on molecules, clusters and liquids
- Ion Time-Of-Flight mass spectrometry
- Electron energy resolved PEPIPICO on molecules and clusters
- Multi-coincident, momentum imaging (Reaction microscope /COLTRIMS) on molecules/clusters (final stages of commissioning)
- Multi-coincident electron spectroscopy using a Magnetic Bottle electron spectrometer (available via collaboration with one of our user groups)
- Negative-ion/positive-ion coincidence spectroscopy (under commissioning)
- Gas phase RIXS (under development)
- Liquid jet RIXS (under commissioning)
- Ambient pressure XPS using a liquid micro-jet
- Single-bunch operation will be available at the 1.5 GeV ring during a couple of weeks of each academic year, allowing time-resolved experiments at the soft x-ray beamlines.
- FemtoMAX beamline delivers short (~100fs) pulses of light in the tender and hard x-ray ranges and has an 800nm pump laser available to its users. Potentially opening up the possibility of pump probe gas phase experiments at MAX IV.

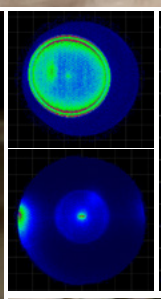

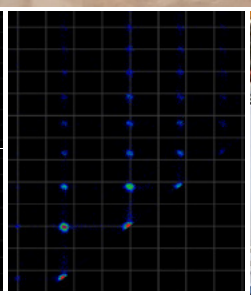

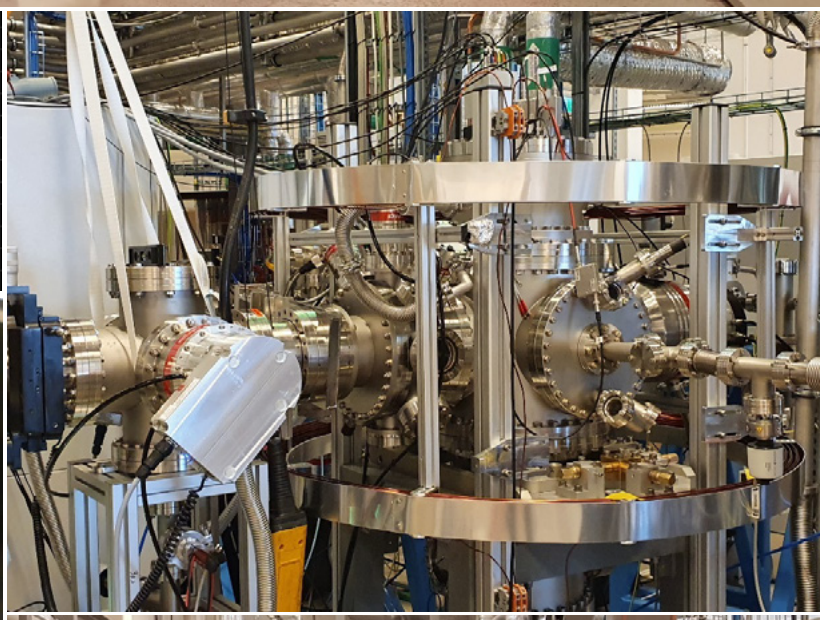

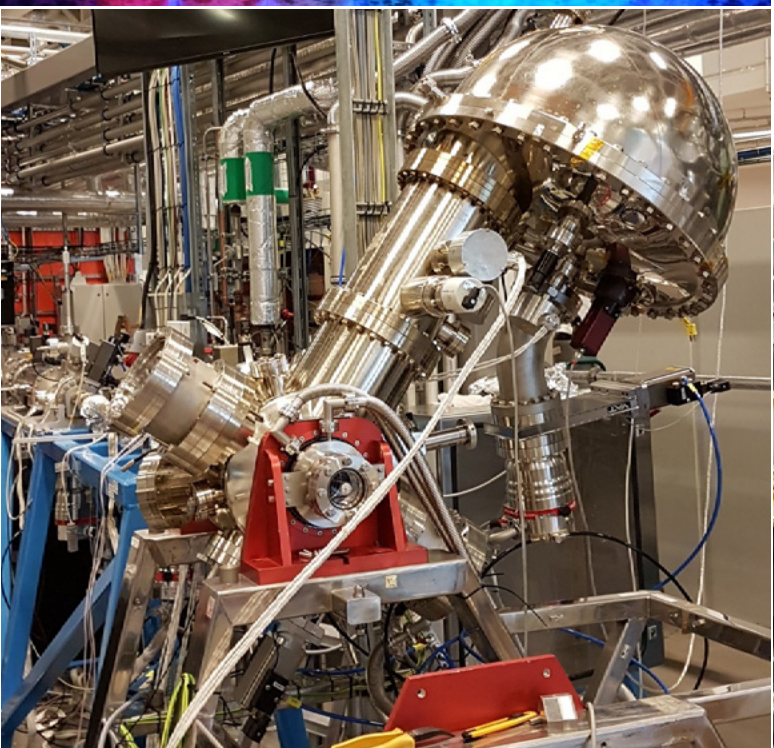

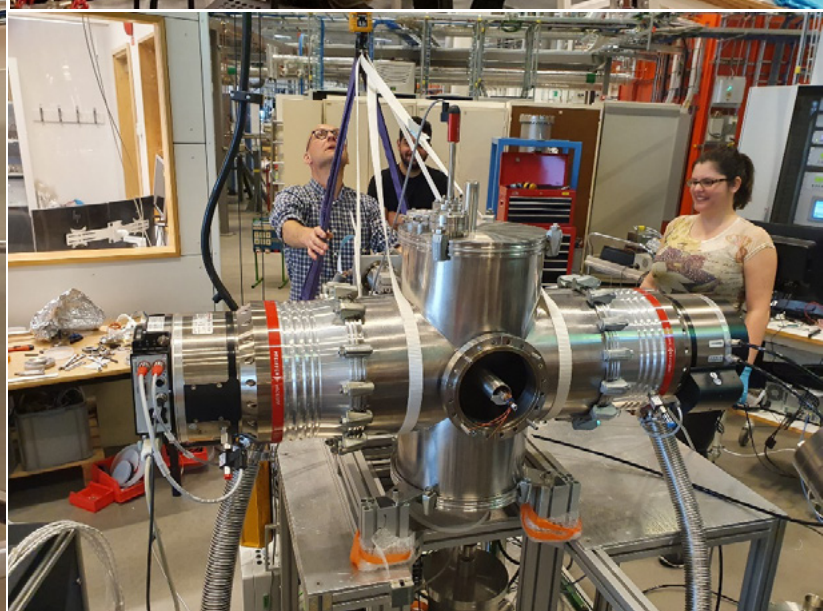

LDM publications 2018 – 2019

Sample	Year	Publication	Beamline
Clusters	2019	Fission of charged nano-hydrated ammonia clusters – microscopic insights into the nucleation processes Oostenrijk et al. https://doi.org/10.1039/C9CP04221K	I411, MAX-lab
Clusters, nanoparti-cles	2019	Tin-oxide nanoparticles deposited from a beam: what happens to the composition? Tchaplyguine et al. https://doi.org/10.1039/C8CP06168H	I411, MAX-lab
Clusters, nanoparti-cles	2018	Ag-Cu Oxide Nanoparticles with high oxidation states: Towards new high T c materials Tchaplyguine et al. https://doi.org/10.1039/C8DT04118K	I411, MAX-lab
Clusters	2018	The role of charge and proton transfer in fragmentation of hydrogen-bonded nanosystems: the breakup of ammonia clusters upon single photon multi-ionization Oostenrijk et al. https://doi.org/10.1039/C7CP06688K	I411, MAX-lab
Liquid jet	2018	Anomalous surface behavior of hydrated guanidinium ions due to ion pairing Ekholm et al. https://doi.org/10.1063/1.5024348	I411, MAX-lab
Liquid jet	2018	Shifted equilibria of organic acids and bases in the aqueous surface region† Werner et al. https://doi.org/10.1039/C8CP01898G	I411, MAX-lab
Liquid jet	2018	Strong enrichment of atmospherically relevant organic ions at the aqueous interface: the role of ion pairing and cooperative effects Ekholm et al. https://dx.doi.org/10.1039/c8cp04525a	I411, MAX-lab
Molecular	2019	Energy-Dependent Relative Cross Sections in Carbon 1s Photoionization: Separation of Direct Shake and Inelastic Scattering Effects in Single Molecules Travnikova et al. https://doi.org/10.1021/acs.jpca.9b05063	International study, part of work performed at I411, MAX-lab
Molecules	2018	Role of ultrafast dissociation in the fragmentation of chlorinated methanes Kokkonen et al. https://doi.org/10.1063/1.5026720	I411, MAX-lab
Molecules	2018	Fragmentation of imidazole, pyrimidine and purine induced by core ionization: Significance of small-scale chemical environment Itäla et al. https://doi.org/10.1016/j.jphotochem.2018.01.003	I411, MAX-lab
Liquid jet	2019	Chemical equilibria of aqueous ammonium– carboxylate systems in aqueous bulk, close to and at the water–air interface† Salamanca Blanco et al. https://doi.org/10.1039/C9CP02449B	I411, MAX-lab
Liquid jet	2019	pH-dependent X-ray Photoelectron Chemical Shifts and Surface Distribution of Cysteine in Aqueous Solution Caravetta et al. https://doi.org/10.1021/acs.jpcb.9b00866	International study, part of work performed at I411, MAX-lab
Ionic liquids	2019	The electronic structure of ionic liquids based on the TFSI anion: A gas phase UPS and DFT study Kuusik et al. https://doi.org/10.1016/j.molliq.2019.111580	FinEstBeAMS, MAX IV

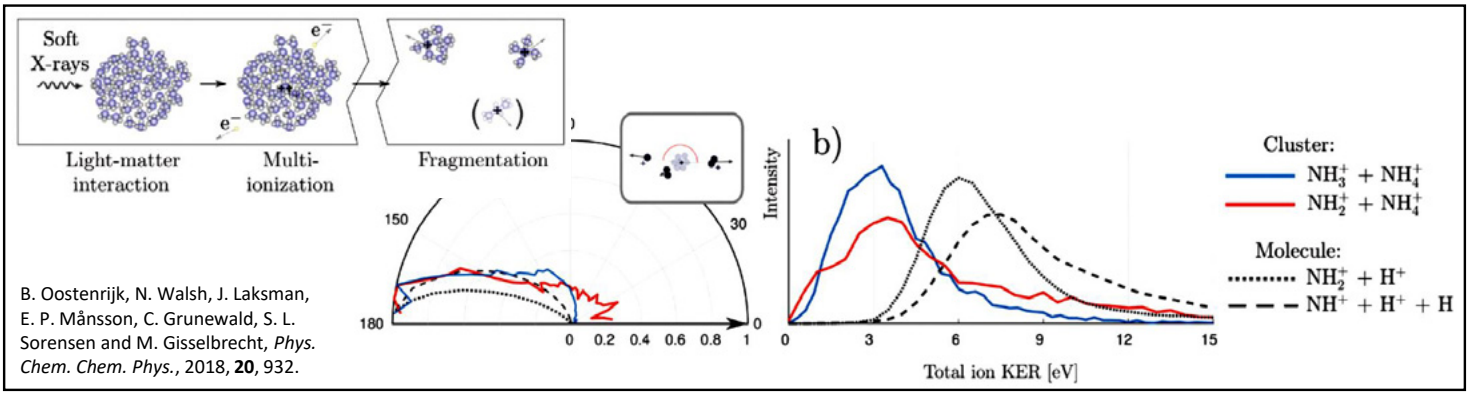

B. Oostenrijk, N. Walsh, J. Laksman, E. P. Månsson, C. Grunewald, S. L. Sorensen and M. Gisselbrecht, *Phys. Chem. Chem. Phys.*, 2018, **20**, 932.

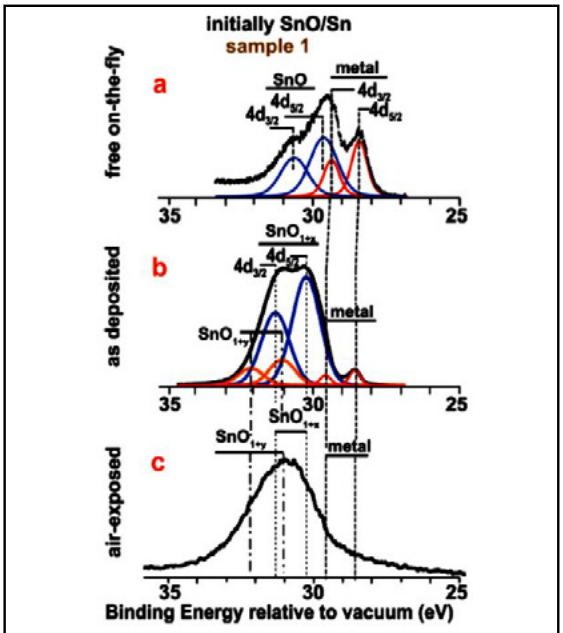

M. Tchaplyguine, C. Wright, A. Shavorskiy, S. Zhu, M.-H. Mikkelä, C. Zhang, O. Björneholm, E. Mårsell, A. Mikkelsen, S. Sorensen, C. J. D. Hetherington and L. R. Wallenberg, *Phys. Chem. Chem. Phys.*, 2019, **21**, 6287.

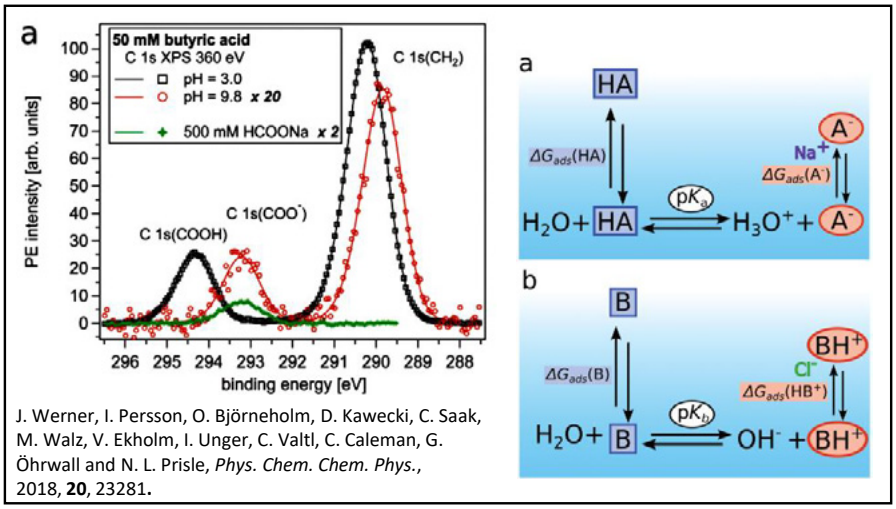

J. Werner, I. Persson, O. Björneholm, D. Kawecki, C. Saak, M. Walz, V. Ekholm, I. Unger, C. Valtl, C. Caleman, G. Öhrwall and N. L. Prisle, *Phys. Chem. Chem. Phys.*, 2018, **20**, 23281.

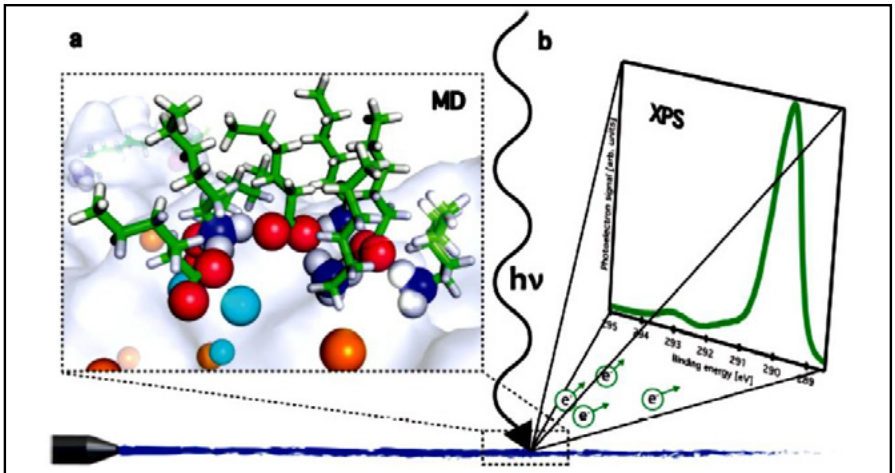

V. Ekholm, C. Caleman, N. Bjärnhall Prytz, M. Walz, J. Werner, G. Öhrwall, J.-E. Rubensson and O. Björneholm, *Phys. Chem. Chem. Phys.*, 2018, **20**, 27185.

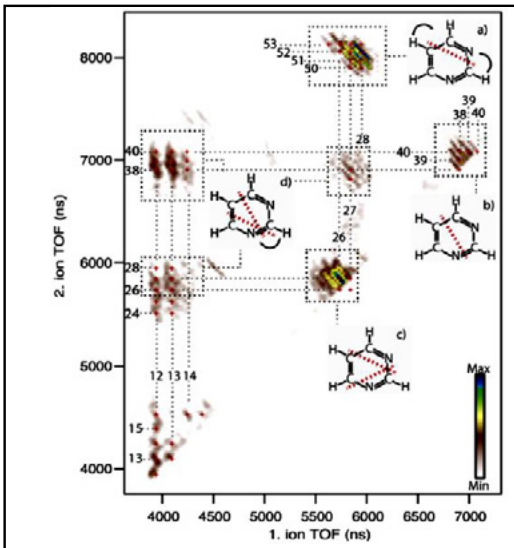

E. Itälä, S. Granroth, D.T. Ha, K. Kooser, H. Levola, E. Rachlew, K. Tanzer, E. Kukk, J. Photochem. Photobiol. A: Chem. 356 (2018) 283.

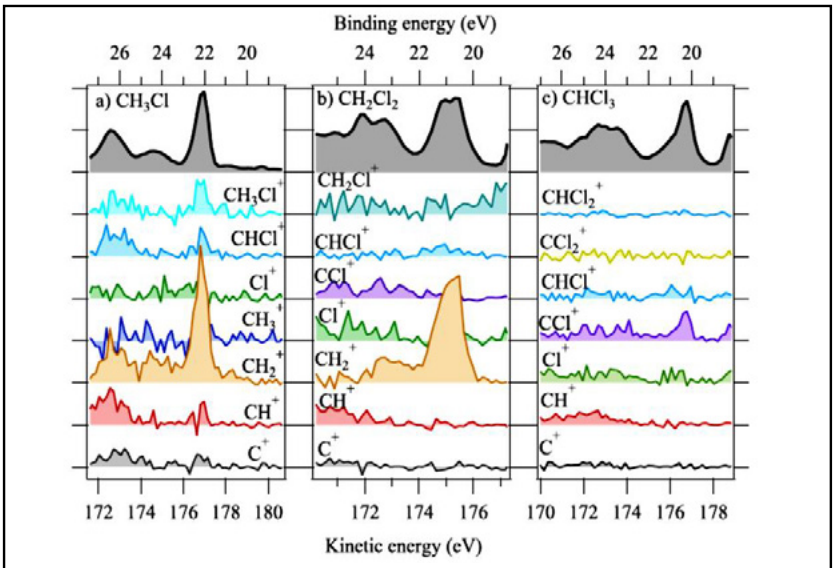

E. Kokkonen, K. Jänkäla, M. Patanen, W. Cao, M. Hrast, K. Bucar, M. Zitnik, M. Huttula, JCP, 148 (2018) 174301.

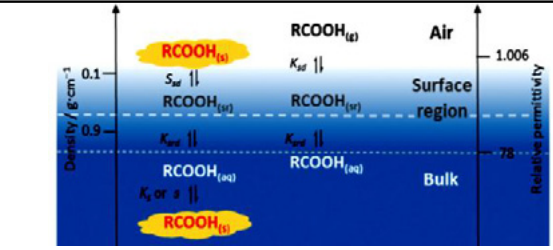

Y. S. Blanco, Ö. Topel, É. G. Bajnóczi, J. Werner, O. Björneholm and I. Persson, *Phys. Chem. Chem. Phys.*, 2019, **21**, 12434

MAX IV Accelerators

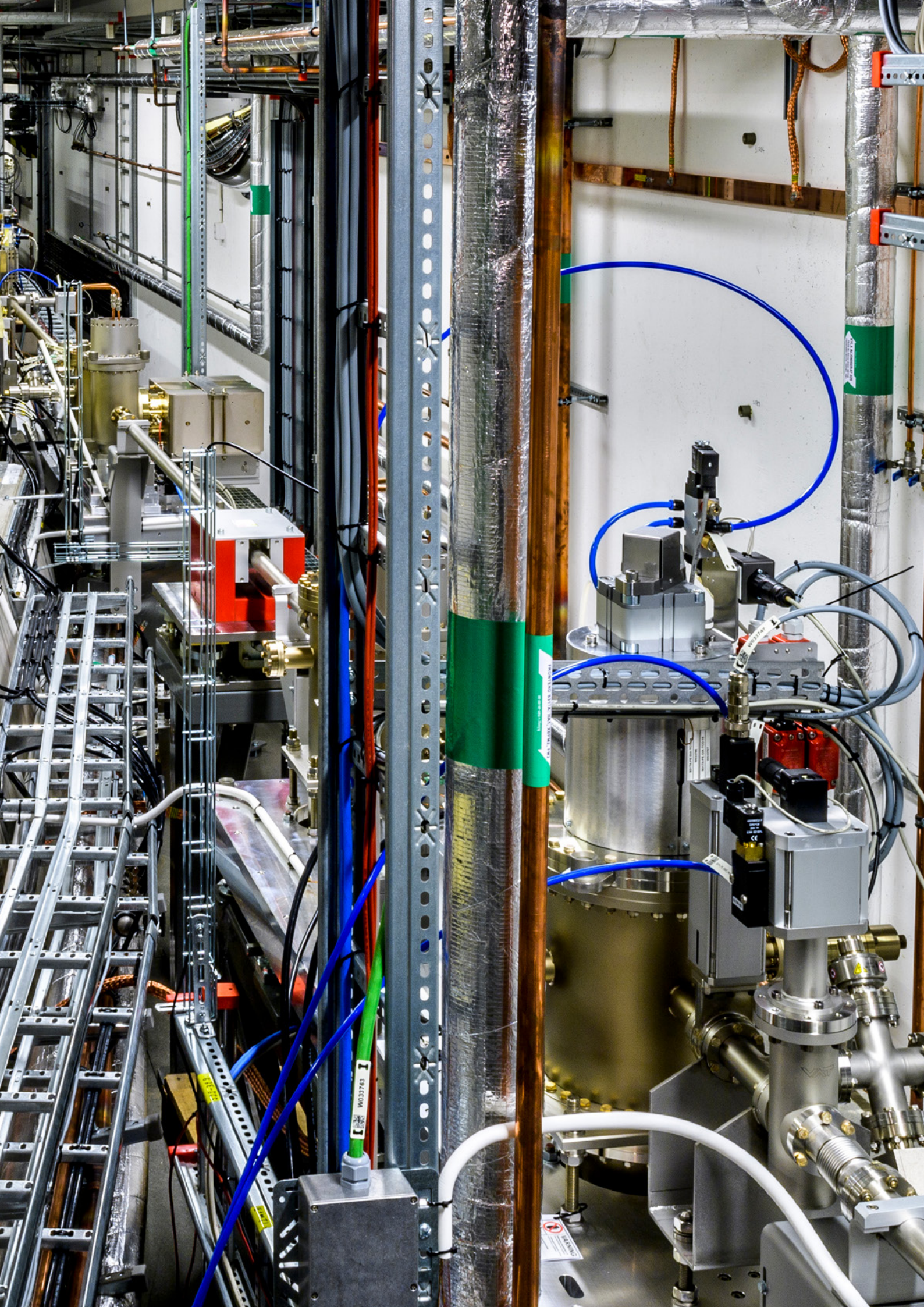

Overview

The period since the last edition of this MAX IV Science Highlights & Activity report marks a major transition in the history of accelerator-based science in Sweden and the world. In fact, over the past years, a whole new suite of high-performance electron accelerators has been commissioned and put into routine operation for the benefit of the Swedish, Nordic and international communities of users of synchrotron-radiation based techniques and tools.

Amongst the three accelerators that make up the MAX IV accelerator complex, the MAX IV 3 GeV ring is the first fourth-generation storage ring worldwide, which makes use of the multi-bend achromat (MBA) lattice to achieve ultralow emittance of 330 pm rad in its 528 metre circumference. A number of innovative and daring technologies were developed and successfully demonstrated to make this outstanding performance possible, in particular compact magnet blocks, NEG (non-evaporable getter) coated copper vacuum chambers and a low frequency RF system complemented with higher harmonic passively operated cavities. The impact of the first successful demonstration of the MBA concept is underscored by the number of projects worldwide that followed in the footsteps of the MAX IV pioneering efforts, amongst which the most recent are the Brazilian Synchrotron Sirius and the European Synchrotron Radiation Facility upgrade EBS.

The MAX IV facility is however not limited to the 3 GeV ring. In fact a 3 GeV linear accelerator serves not only as an injector to the MAX IV rings but is also a light source by itself, using two bunch compressors to provide ultrashort electron bunches (nominally down to 100 fs) that produce ultrashort X-ray pulses through spontaneous emission in the undulators of the Short Pulse Facility. Finally, a 1.5 GeV storage ring, optimized for the production of soft X-rays and UV radiation complements the facility portfolio, meeting the needs of the historically very strong spectroscopy community in Sweden.

The following sections present performance and operation highlights of the MAX IV accelerators, with a focus on the most recent achievements. Apart from delivering the design parameters required for injection into the two storage rings, the linear accelerator has demonstrated the production of electron bunch durations well below the nominal 100 fs. The innovative bunch compressor design has proven to provide reliable linearization of the energy chirp required for compression as well as outstanding stability.

The 1.5 GeV ring achieved its nominal operation current of 500 mA in June 2018 and delivers now routinely 400 mA to users, the intensity being limited by heating of optical components in the beamlines. In addition, single-bunch mode of interest for time-resolved experiments in a number of beamlines has become, since early 2020, a regular user delivery mode in this ring. Even though the typical current delivered in single-bunch mode is of the order of 20 mA, single-bunch currents in excess of 93 mA have been demonstrated. Finally, initial tests done in collaboration with the accelerator physics team at HZB Berlin have demonstrated the possibility of implementing Transverse Resonance Island Buckets (TRIBs), which have the potential of allowing pseudo-single bunch operation.

The demonstration of a record low emittance $\varepsilon_x = 320 \pm 18$ pm in the 3.0 GeV ring [2] was not only a confirmation of the sound MBA design, but also of the excellent performance of the instrumentation (diagnostic beamlines) needed to measure the correspondingly very small beam sizes. Also outstanding has been the position stability (well below the typical 10 %-of-beam size rule-of-thumb) that has been achieved even without the use of fast orbit feedback systems. These feedback systems have nevertheless also been implemented and are under commissioning in the 3 GeV ring, not as a means to counteract vibrations (as has been the case in several third-generation light sources) but as a means to compensate for the perturbations introduced by gap and phase motion of insertion devices.

The nearly 100 % NEG coated vacuum system performance has shown to be excellent, providing vacuum lifetime performance (20 A.h) well in excess of the design goals. Finally, top-up injections have achieved record transparency with transient beam size perturbations associated to injection being reduced down to micrometre level as a result of the use of a multipole injection kicker (MIK) developed in a collaboration with the French SOLEIL synchrotron laboratory.

It is important to highlight that the MAX IV accelerators have, in the past few years, successfully completed the transition from a construction project into a running facility with the establishment of an operations team and organizational and technical infrastructure and procedures that allowed achieving internationally competitive levels of delivery hours and accelerator reliability.

Finally, following a MAX-lab tradition, the preparation for the mid and long-term future of the MAX IV accelerators started already the same year the facility was inaugurated, 2016, with the preparation of the accelerator roadmap as part of the MAX IV strategy plan 2016–2026. Amongst the development paths foreseen in that roadmap, this report briefly describes the current work on a conceptual design for a soft X-ray free electron laser, the SXL, which uses the MAX IV 3 GeV linear accelerator to produce ultra-short pulses in the 1–5 nm wavelength range.

Mikael Eriksson (left), creator of the MAX IV design concept and Machine Director 1974–2015 with Pedro Tavares Fernandes (right), Accelerator Director since 2016, discussing the performance of the multi-bend achromat in the 3 GeV storage ring. Photo: Madeleine Schoug

Accelerator Operations

As of mid-2020, all three accelerators at MAX IV have transitioned well into the operational phase of their lifetimes. The time during which the accelerators deliver light to users has reached levels matching those of mature world-class facilities. In addition, the fraction of time during delivery for which the accelerators were not operational, perhaps due to a technical issue, has also fallen to a level consistent with a cutting-edge international laboratory.

This period of transition began in 2017 and was broadly completed by the end of 2018. Of particular importance to this process was the start of 24/7 operation of the accelerators by a dedicated group, and the founding of a round-the-clock on-call service by the major technical groups.

Figure 1 shows the time for which the accelerators were scheduled to deliver beam to the beamlines over the last four years. Note the strong increase from 2017 to 2018, which was facilitated by the onset of 24/7 work by a team of professional operators.

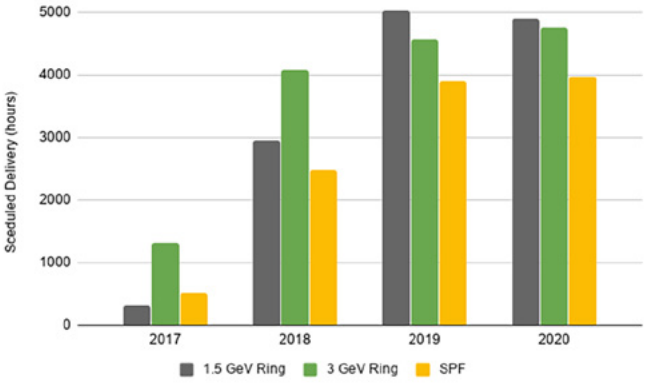

Figure 1: Year-by-year delivery hours scheduled for each accelerator.

There was a considerable expansion of the Accelerator Operations Group at the beginning of 2018 to allow for continuous operation of the accelerators. This group now consists of the equivalent of eight full-time operators, as well as a Head and an Assistant Head of Accelerator Operations. Experience over the last two years shows that this allows continuous attended operation of the accelerators, as well as providing for sufficient redundancy to cover any periods of absence for particular operators.

The daily work of an operator is split into three shifts: “Day Shift” 08:00–16:00, “Evening Shift” 16:00–24:00, and “Night Shift” 00:00–08:00. The schedule is agreed in advance of coming into force and is designed so that a full-time operator will work an average of 36 hours per week.

In addition to the scheduled annual running time of the accelerators, another major metric is fraction of time during which the accelerators are supposed to be in operation but are suffering from technical problems. This is referred to as the “downtime” for the accelerator, and the evolution of this is shown in Figure 2.

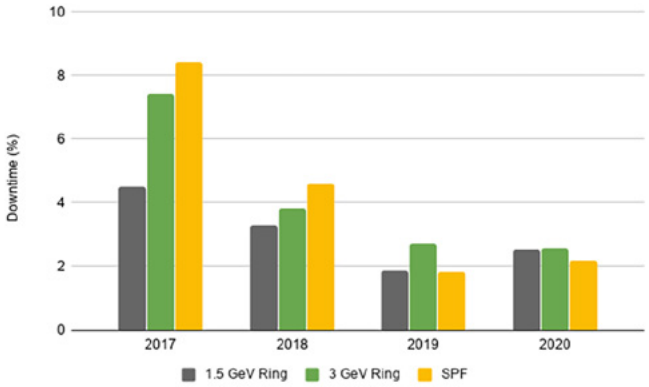

Figure 2: Year-by-year downtime for the three accelerators. The values are given as percantage of the scheduled delivery time for that year.

Achieving a downtime fraction of less than 3 % puts the MAX IV accelerators in the top-flight of such facilities, especially when the maturity of the accelerators is considered. This level of success is due to the dedication and hard work of technical teams throughout the lab. Of particular importance is the existence of the on-call service provided by many of these groups. Each of the technical teams provides a phone number that is attended 24/7. In case of a problem with a system belonging to one of these groups, an operator can call to get advice or to bring in a technical

Busy control room when starting up beamlines.

expert to help solve the issue.

Having such easy access to technical expertise has led to a significant reduction in the Mean Time To Repair (MTTR) accelerator faults, thus leading to the significant improvement in the downtime fraction shown in Figure 2.

As part of the transition to operations, a regular schedule was implemented for the operation of the accelerators throughout a standard week. This is shown in Figure 3.

The week begins at 08:00 on Monday with a general shutdown of the accelerators to allow for planned accelerator and beamline maintenance and installation activities. Once these are completed, a series of validation exercises is run on the accelerators to ensure that they are prepared to provide the expected beam conditions for the remainder of the week.

On Tuesday at 08:00, the accelerators then begin to provide beam with special requirements to allow commissioning of various beamline-related devices. This might be studies in the beamlines, but also includes characterisation of the performance of the insertion devices used to generate the X-ray beams.

Delivery under normal conditions then begins on Wednesday at 08:00 and runs through the remainder of the week.

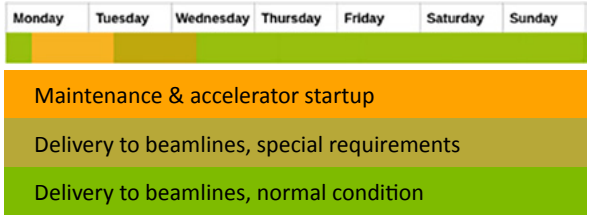

Figure 3: High-level weekly operational plan for the accelerators.

The week-by-week plan for the operation of the accelerators is agreed several months in advance through discussions between stakeholders in the accelerator and beamline divisions. Once this is complete the plan is published online, an example of this is shown in Figure 4.

Week	Start date	LINAC	R1 (1.5 GeV)	R3 (3 GeV)
1	December 30	RF Conditioning	RF Conditioning	RF Conditioning
2	January 6, 2020	Shutdown	Shutdown	Shutdown
3	January 13	Startup	Startup	Startup
4	January 20	Accelerator Studies (reduced)	Accelerator Studies	Accelerator Studies
5	January 27	Startup	Delivery to beamlines	Accelerator Studies
6	February 3	Delivery to SPF & Rings	Delivery to beamlines	Delivery to beamlines
7	February 10	Delivery to SPF & Rings	Delivery to beamlines	Delivery to beamlines
8	February 17	Delivery to SPF & Rings	Delivery to beamlines	Delivery to beamlines
9	February 24	Accelerator Studies	Delivery to beamlines	Delivery to beamlines
10	March 2	Delivery to SPF & Rings	Delivery to beamlines	Delivery to beamlines
11	March 9	Delivery to SPF & Rings	Delivery to beamlines	Delivery to beamlines
12	March 16	Delivery to SPF & Rings	Delivery to beamlines	Delivery to beamlines
13	March 23	Accelerator Studies (reduced)	Accelerator Studies	Delivery to beamlines
14	March 30	Delivery to SPF & Rings	Delivery to beamlines	Delivery to beamlines
15	April 6	Delivery to SPF & Rings	Delivery to beamlines	Delivery to beamlines
16	April 13	Accelerator Studies (reduced)	Delivery to beamlines	Accelerator Studies
17	April 20	Delivery to SPF & Rings	Delivery to beamlines	Delivery to beamlines
18	April 27	Delivery to SPF & Rings	Delivery to beamlines	Delivery to beamlines
19	May 4	Delivery to SPF (reduced) & Rings	Delivery to beamlines	Accelerator Studies
20	May 11	Delivery to SPF & Rings	Delivery to beamlines	Delivery to beamlines
21	May 18	Delivery to SPF & Rings	Delivery to beamlines (reduced)	Delivery to beamlines
22	May 25	Accelerator Studies	Delivery to beamlines	Delivery to beamlines
23	June 1	Delivery to SPF & Rings	Delivery to beamlines	Delivery to beamlines
24	June 8	Delivery to SPF (reduced) & Rings	Accelerator Studies	Delivery to beamlines
25	June 15	Delivery to SPF & Rings	Delivery to beamlines	Delivery to beamlines
26	June 22	Delivery to SPF & Rings	Delivery to beamlines	Delivery to beamlines
27	June 29	Delivery to SPF & Rings	Delivery to beamlines	Delivery to beamlines
28	July 6	Delivery to SPF & Rings	Delivery to beamlines	Delivery to beamlines
29	July 13	Shutdown	Shutdown	Shutdown
30	July 20	Shutdown	Shutdown	Shutdown
31	July 27	Shutdown	Shutdown	Shutdown
32	August 3	Shutdown	Shutdown	Shutdown
33	August 10	Shutdown	Shutdown	Shutdown
34	August 17	Startup & Survey	Startup & Survey	Startup & Survey
35	August 24	Radiation Survey	Radiation Survey	Radiation Survey
36	August 31	Delivery to SPF & Rings	Delivery to beamlines	Delivery to beamlines
37	September 7	Delivery to SPF & Rings	Delivery to beamlines	Delivery to beamlines
38	September 14	Delivery to SPF & Rings	Delivery to beamlines	Delivery to beamlines
39	September 21	Delivery to SPF & Rings	Delivery to beamlines	Delivery to beamlines
40	September 28	Accelerator Studies (reduced)	Delivery to beamlines	Accelerator Studies
41	October 5	Delivery to SPF & Rings	Delivery to beamlines	Delivery to beamlines
42	October 12	Delivery to SPF & Rings	Delivery to beamlines	Delivery to beamlines
43	October 19	Delivery to SPF & Rings	Delivery to beamlines	Delivery to beamlines
44	October 26	Delivery to SPF & Rings	Delivery to beamlines	Delivery to beamlines
45	November 2	Delivery to SPF & Rings	Delivery to beamlines	Delivery to beamlines
46	November 9	Delivery to SPF & Rings	Delivery to beamlines	Delivery to beamlines
47	November 16	Radiation Survey	Radiation Survey	Radiation Survey
48	November 23	Radiation Survey	Radiation Survey	Radiation Survey
49	November 30	Delivery to SPF & Rings	Delivery to beamlines	Delivery to beamlines
50	December 7	Delivery to SPF & Rings	Delivery to beamlines	Delivery to beamlines
51	December 14	Accelerator Studies	Delivery to beamlines	Delivery to beamlines

Fig 4. Annual plan for most of 2020.

3 GeV Storage Ring

The MAX IV 3 GeV storage ring is a 528 metre circumference synchrotron, which uses a multi-bend achromat (MBA) lattice to reach an equilibrium emittance of 328 pm rad.

The commissioning of the 3 GeV ring started 11 August 2015. First turn was achieved without the use of any orbit correctors and by 15 September there was stored beam in the accelerator. Commissioning activities such as calibration of diagnostics, orbit correction, optics tuning, RF tuning, vacuum laundry, etc. then proceeded apace allowing the current to be ramped up to 120 mA by January 2016. During the first half of 2016 up to the inauguration in June, the two first In-Vacuum Undulators (IVUs) were installed and beamline commissioning started. Regular user operations for these first beamlines then commenced in spring 2017. For detailed accounts of the 3 GeV ring commissioning, please see [1-2, 10].

The 3 GeV ring is equipped with a suite of diagnostic tools, among them a large number of beam position monitors (BPMs) able to continuously monitor the transverse orbit position with bandwidths compatible with extracting both turn-by-turn and averaged positions, sampled at both 10 kHz and 10 Hz.

Since the commissioning, a few BPMs have been re-purposed for use as RF pick-ups. Vertical beam size and energy spread, two key parameters determining achievable beamline performance, can be monitored non-destructively via the two diffractometric diagnostic beamlines [5] using visible SR. To measure the beam current a Direct Current Current Transformer (DCCT) is used.

Additional diagnostic systems that affect the beam are also available for tuning the accelerator during maintenance and accelerator studies shifts, as they cannot be used online during delivery. They include insertable scrapers, an insertable screen, and pulsed dipole magnets, with which it is possible to study beam lifetime composition, the injected beam dimensions and the ring magnet optics. These were all instrumental during the start-up and commissioning of the accelerator [1,2,4].

A broadband transverse bunch-by-bunch (BbB) feedback system makes use of button pickups and stripline kickers to guarantee transverse beam stability at high currents as the beam starts to interact more strongly with the surrounding vacuum chambers.

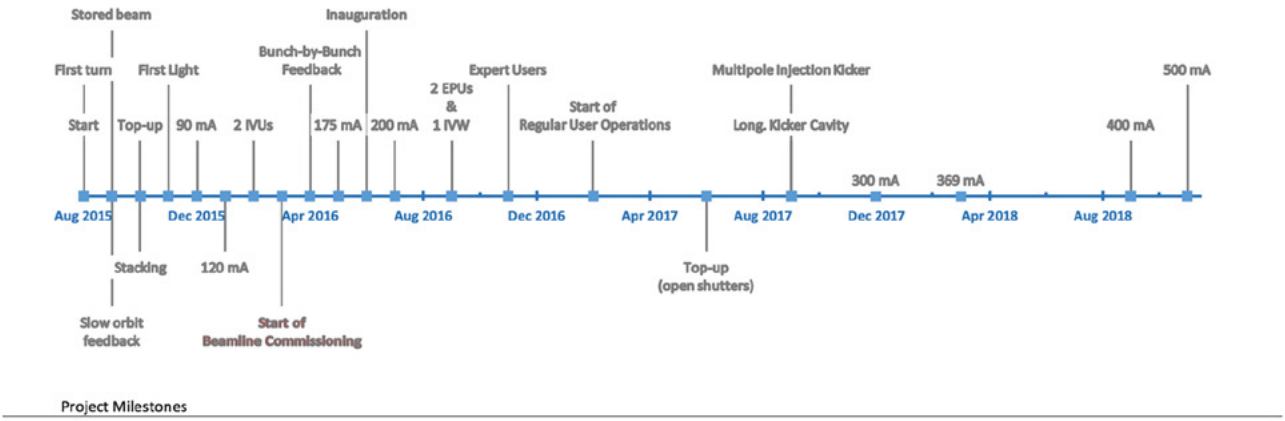

The 3 GeV Storage Ring commissioning timeline

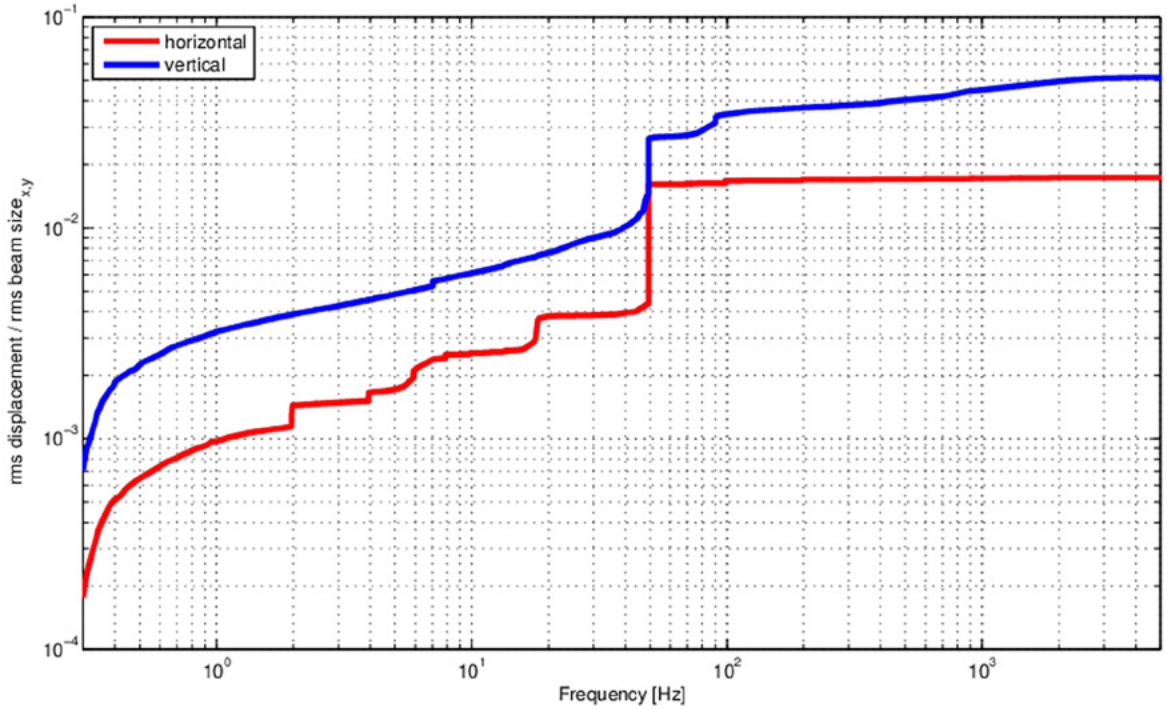

Figure 5 : Integrated power spectral density for the e-beam position readings, taken at the 250 mA delivery current. Orbit noise at 50 Hz, the electrical grid frequency, is a large contribution to the overall beam noise in the vertical plane.

In addition, the BbB provides a convenient online measurement of the transverse tunes. Longitudinal stability at high currents is obtained through a combination of passively operated harmonic cavities and RF system feedback loops including main cavity amplitude and phase loops as well as Robinson mode feedback [16].

A Slow Orbit Feedback (SOFB) system uses the beam position data to counteract drifts and slow orbit perturbations using dipole corrector magnets; it works at a 5 Hz repetition rate during normal delivery and is able to damp orbit motion below a cut-off frequency of roughly 0.1 Hz. Given the very low levels of noise that couple to the beam, this has allowed the accelerator to deliver better than the typical rule-of-thumb '10 % of RMS beam size' position stability, corresponding to 300 nm in the vertical plane.

As seen in Figure 5, the rms stability comes in below that, at roughly 2 % and 5 % of the RMS beam size in the horizontal and vertical plane, respectively, when using 3.3 kHz bandwidth data.

Nonetheless, a Fast Orbit Feedback (FOFB) system is currently in commissioning which will cooperate with the existing SOFB [6] to further improve the beam stability. This uses a 10 kHz data stream from the BPMs together with ferrite-core steerer magnets to damp orbit noise in the Insertion Device (ID) straight sections.

Initial results show a noise rejection cut-off frequency of 125 Hz is possible. However, the primary benefit is expected to be the damping of perturbations from insertion device gap changes.

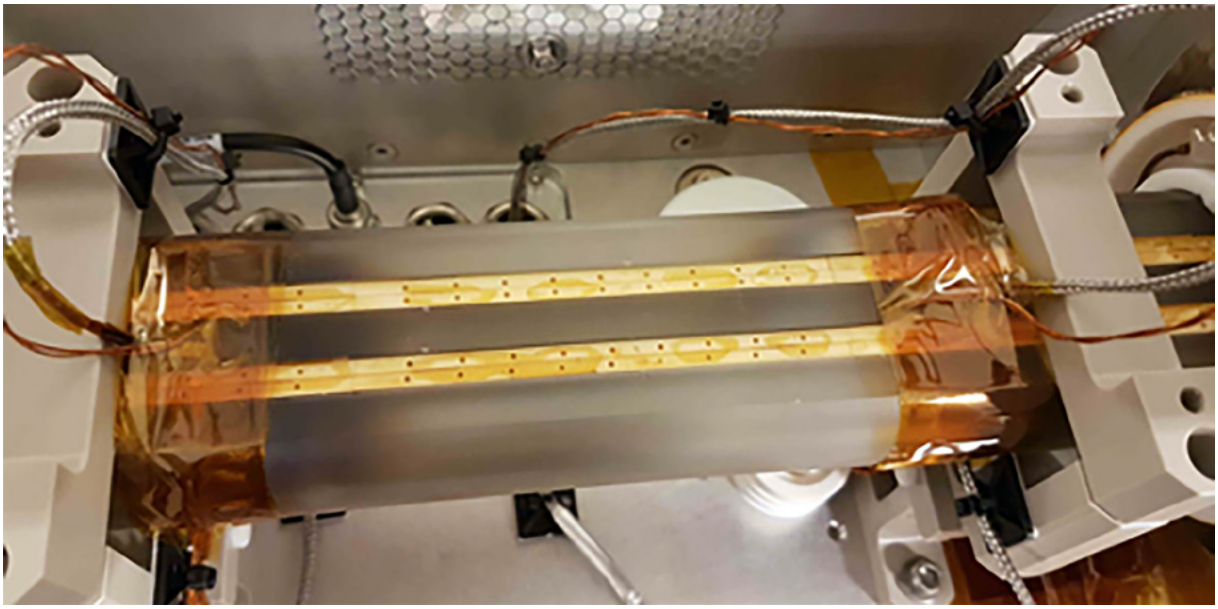

Figure 6: Multipole Injection kicker housing, showing the vacuum chamber with the machined grooves and current leads

While initially the 3 GeV ring made use of a single pulsed dipole injection kicker during commissioning, a Multipole Injection Kicker (MIK) [7], [8], [9] has been designed and constructed in a collaboration with the French synchrotron laboratory SOLEIL. The first version of the MIK was installed in late 2017. It quickly became the primary mode of injection and vastly decreased the transient disturbances during top-up events. During the summer shutdown 2019 the original MIK chamber was exchanged for a new version, (Fig. 6), machined to better tolerances and with a thicker coating on the ceramic chamber. The thicker coating successfully addressed overheating issues and the improved mechanics led to a further reduction of the residual beam size perturbations to sub-micrometre level in the vertical plane.

The vacuum chambers for the 3 GeV ring are made of copper and close to the entire ring is coated with Non-Evaporable Getter (NEG); a necessity given the small cross-section of the vacuum chamber which, although it enables stronger fields in the magnets, would otherwise necessitate a large number of discrete pumps around the circumference in order to cope with the low vacuum conductance. The NEG coating instead provides distributed pumping and enables very good vacuum lifetimes, i.e. low beam particle loss rates due to scattering on residual gas molecules. 23 March 2020, after a total accumulated dose of 2690 Ah, vacuum lifetimes in excess of 39 Ah were observed.

NEG-coated surfaces do require a bake-out and activation procedure in order to pump effectively, which can be a lengthy process as a disassembly of the surrounding magnet structures is required. Hence, during a planned vacuum intervention in summer 2018, a method originally developed for the LHC [11] was trialled at a synchrotron for the first time where the chambers were vented using purified neon gas. As neon is not pumped by NEG coating the activation was preserved. Beam lifetime quickly recovered to the prior levels after the intervention, as seen in figure 7.

It should be noted that although the present delivery current is 250 mA, the vacuum system has been validated at the full design current of 500 mA since November 2018. All the design goals of the vacuum system have thus been met.

Both rings at the MAX IV laboratory use the same type of normal-conducting, capacity-loaded cavities, described in more detail in [13]. The 3 GeV ring uses 6 cavities each powered by a 60 kW solid-state amplifier; in order to reach the full 500 mA design current with a full complement of insertion devices, an upgrade to 120 kW is foreseen. There are also three passive harmonic cavities at 300 MHz installed in the ring, in order to elongate the bunches. This acts to improve the Touschek lifetime, i.e. loss of beam particles due to intra-beam scattering, and to improve the beam stability.

The 3 GeV ring vacuum system under installation in 2015.

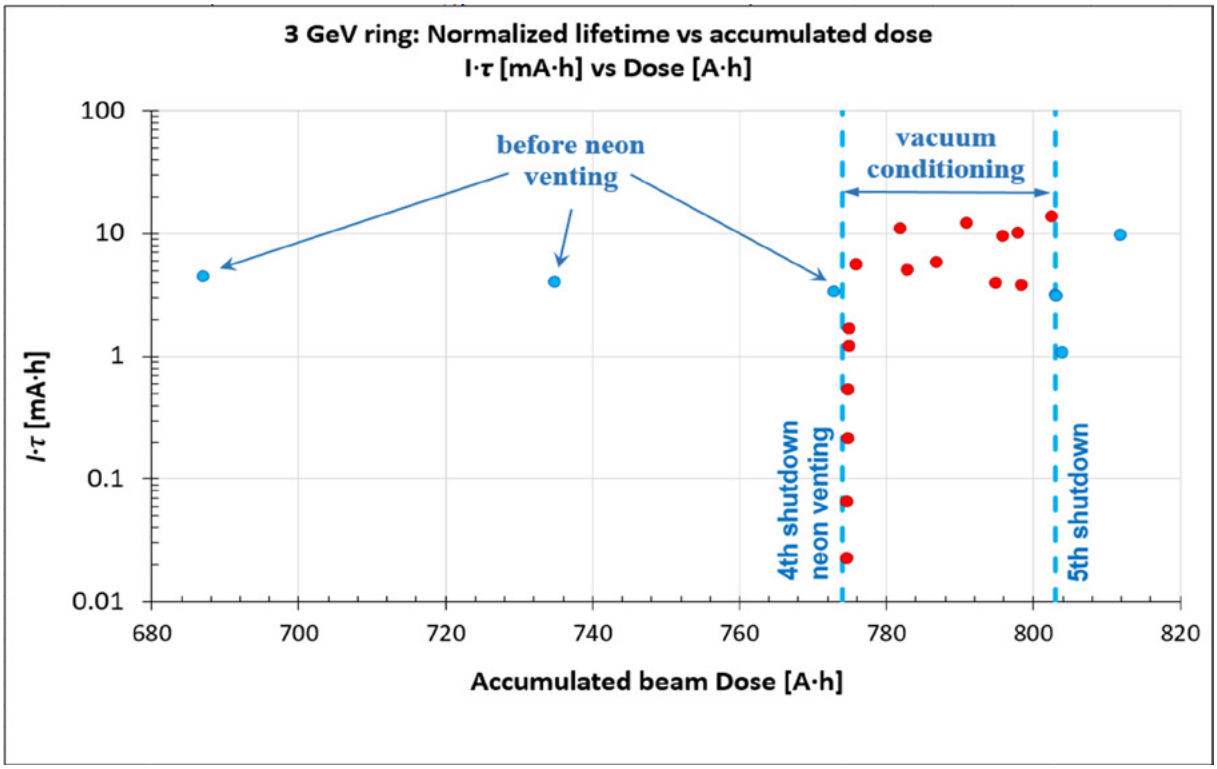

Figure 7: Normalized lifetime as a function of accumulated dose in the 3 GeV ring, before and after the Ne-intervention just before the maintenance shutdown during summer 2018. Plot by E. Al-Dmour.

Installing the power coupler in a 3 GeV 100 MHz RF cavity (left) and the final installed setup (right) in the 3 GeV ring.

The MAX IV 3 GeV ring magnets use a design with all magnetic elements integrated into a number of solid iron blocks, 7 per achromat. The Multi-Bend Achromat (MBA) lattice the 3 GeV storage ring uses in order to reach its extremely low emittance results in very tight alignment tolerances. The magnet block concept offered a way to meet these inside the blocks by relying on the high accuracy of modern CNC machining in industry; this greatly reduced the alignment work needed at MAX IV during the installation as only the blocks themselves needed to be positioned carefully. Another advantage of the block concept concerned stability; due to the block stiffness it pushed the mechanical eigenfrequencies to above 90 Hz in all cases, where environmental vibration noise levels were expected to be very low and vibrational modes would therefore not be excited. As shown in Figure 5, this expectation has been borne out by observations. Details regarding the magnet design can be found in [14].

The blocks incorporate both the main dipoles with a defocusing gradient, as well as quadrupoles, sextupoles and octupoles. Tuning of the dipole gradient is achieved via pole-face current strips. Furthermore, all sextupoles and octupoles were equipped with configurable trim coils. These can be configured to provide (normal or skew) dipole or quadrupole fields, and in the case of the sextupole trim coils also a sextupol field correction.

Correction of the optics began immediately once beam had been stored in the 3 GeV ring back in late 2015 using standard technique; this process is described in detail in references [2,15]. At the time of writing, the 3 GeV ring is operating with the design linear lattice and at the design working point with tunes of 42.20 and 16.28, in the horizontal and vertical plane respectively. Coupling and linear optics corrections are regularly carried out to preserve the optics and maintain a vertical beam emittance of below 8 pm rad during regular operation. Over the past two years work has also been carried out to develop a method to characterize and correct the non-linear optics, relying on measurements of off-energy closed orbits. This has recently borne fruit as the 3 GeV ring sextupoles have been corrected during spring 2020, yielding an immediate improvement in beam lifetime from 11 hours up to 19 hours. A manuscript detailing the method has been submitted for publication.

1.5 GeV Storage Ring

The MAX IV 1.5 GeV electron storage ring is 96 metre in circumference. With a 12-fold double bend achromatic lattice, including several combined-function magnets, it reaches a horizontal emittance of 6 nm rad, which is comparatively small for that small a storage ring. The purpose of this storage ring is to serve UV and soft X-ray users at the facility. The ring is the successor of the MAX II ring at the old MAX-Lab, with the difference that it need not serve any hard X-ray users, and thus has no wiggler insertion devices. As a comparison, the MAX II ring had a circumference of 90 m and a horizontal emittance of 10 nm rad.

The ring started commissioning in autumn 2016, and went into user operation one year later, according to the time plan. The ring magnet lattice is extremely compact, where the achromat magnets covers only 4.4 metre in length, and thus 3.2 metre is available for an ID. The entire achromat magnet sequence is constructed from one solid iron block in which dipoles, quadrupoles, sextupoles and corrector magnets are all incorporated, thus implying no need for individual magnet alignment. This was a new concept, following the compact magnet blocks used in the MAX III ring, and it turned out to be a successful one as testified by the quick commissioning and the fact that the availability during the following years 2017–2019 has been over 96 %, 97 % and 98 %.

Several insertion devices (ID) were installed during summer 2017, and today the ring contains five operational IDs. One important fact to mention is that even though the IDs are not wigglers, some of them are rather strong and distort the optics of the ring significantly. Special attention is therefore needed for compensating these effects. An on-going effort to implement these corrections consists of breaking up magnet circuits in order to provide additional optics tuning knobs. The ultimate goals is to allow all IDs to cover their full gap and phase ranges during routine operation.

The ring operates in top-up mode each half hour, but with a less sophisticated injection scheme than the 3 GeV ring, and thus the horizontal orbit distortions are larger.

The nominal current of 500 mA was first demonstrated in June 2018. Routine operation is for the moment at 400 mA, due to heat load issues at some beamlines. With a not too offensive use of small gaps in the IDs, the lifetime of the beam is higher than 12.5 hours, which is the design value, even though the beam is delivered with a vertical emittance of less than 30 pm rad (one half of the design value). Together, this leads to a current variation of less than 5 % between the top-up events. The injection rate is typically between 25 mA/min and 100 mA/min, depending on ID gaps, which means that the top-up takes less than a minute.

The two systems responsible for a good lifetime are the RF and the vacuum systems. The RF system is identical to the 3 GeV ring RF system, just with fewer components. Two main cavities and two higher harmonic cavities, where all cavities are situated in one straight section in the ring. Two 60 kW solid state transmitters, via the same 120 kW circulators as in the big ring, serve each one RF main cavity, while the harmonic cavities are both passively driven by the beam. The whole system can elongate the 32 bunches in the ring from being roughly 10 mm (rms) long to reaching a length of around 50 mm (rms). At 500 mA, this raises the beam lifetime from otherwise around 2 hours to 10 hours, which with the above injection scheme makes a huge difference. The vacuum system is a combined system of ion pumps, NEG coated ID chambers and possibility to in-situ activate Titanium sublimation units. The vacuum system, as opposed to the 3 GeV ring, is based on lumped synchrotron radiation absorbers, and vacuum is generated using ion pumps, titanium sublimation pumps and NEG strips, in addition NEG coating is used for the narrow gap vacuum chambers. The rest gas composition is the traditional one, for a well-conditioned vacuum system, with H_2 dominating, and CO, CO_2, CH_4 as the following main contributors at a total level of less than 10 % of the total rest gas pressure.

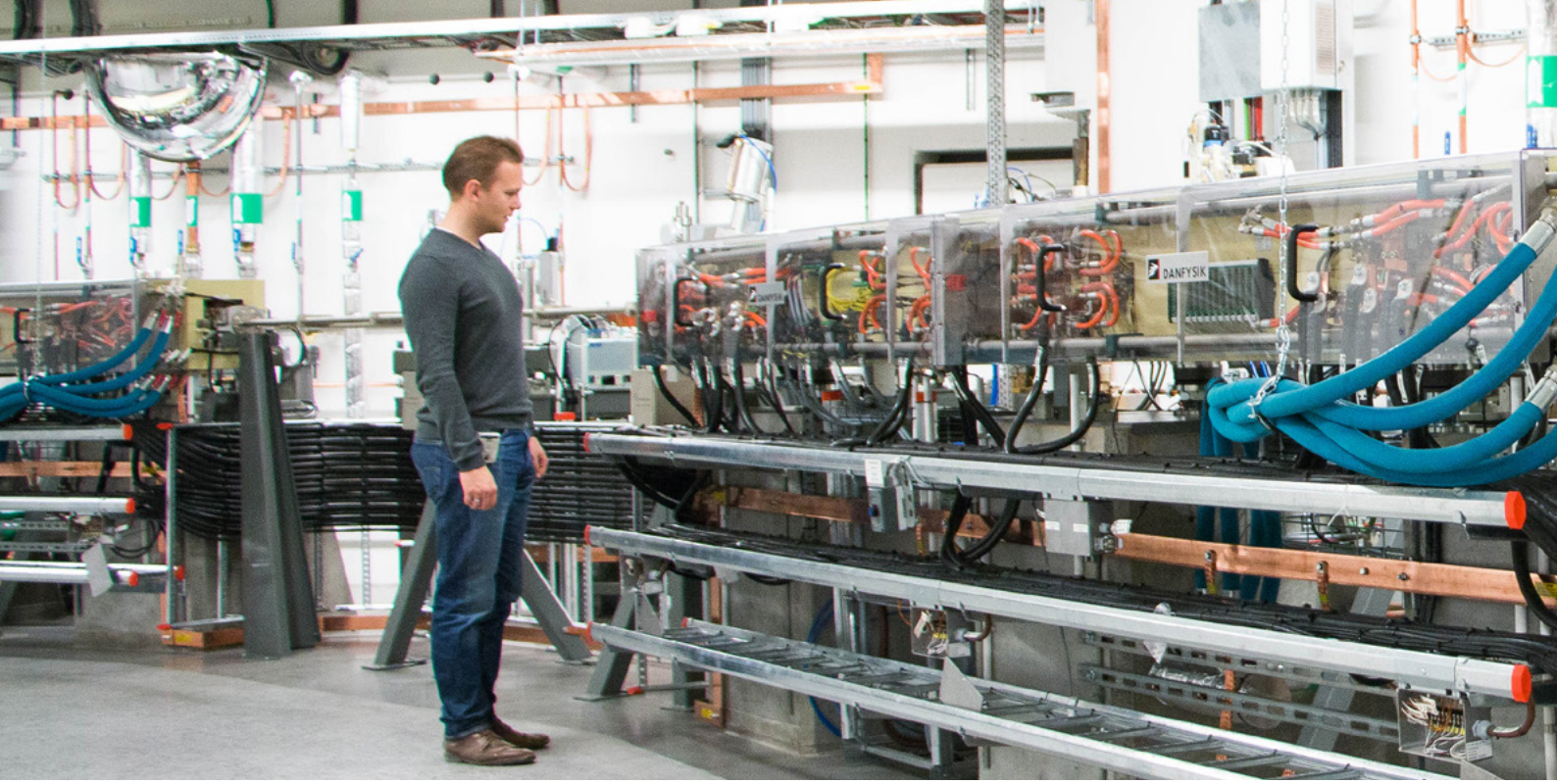

The 1.5 GeV storage ring.

Closely connected to the RF-system, is the longitudinal stability of the beam, or in other words, the ability for the IDs to use higher harmonics of the undulator radiation. With a longitudinally unstable beam, the energy spread ends up at a higher level than the natural, given by the magnet lattice (around 0.07 %), which is detrimental to the ID radiation. The stable region of the beam in the 1.5 GeV ring turned out to be relatively easy to reach, even at the highest current. The dangerous higher order modes (HOM) in the cavities, which are responsible for longitudinal beam instabilities, could fairly quickly during commissioning be avoided by the combination of temperature tuning of the cavities and setting of the tuning point of the higher harmonic cavities. The possible transverse instabilities of the beam also turned out to be easily avoidable. Operating at slightly positive chromaticities led to stable conditions. In single bunch operation almost three times higher bunch current than at nominal multibunch operation could be reached with no or small signs of transverse instabilities.

Beside the beam stability with respect to high beam intensity operation, pure orbit positional stability is of course of utmost importance. The floor and infrastructure of the MAX IV facility has shown a great passive stability against vibrations propagating to the electron beam (see 3 GeV ring). The slow beam movements (< a few Hertz) are kept under control by a slow orbit feedback system, based on a beam position monitor and correction system of the same kind as in the 3 GeV ring. Since the beam sizes at the centre of the IDs in this ring is approximately σ_x=190 µm and σ_y=13 µm, the system has no difficulties keeping vibrations/motions of the beam below the 10 % limit of the actual beam size. The capability of the system is at the same level as for the large ring, where the demands are greater (<0.4 µm). Just as for the 3 GeV ring, the final goal is still to implement also a fast orbit feedback system, which will suppress beam motions further than to the 10 % level, and simultaneously allow for fast changing of ID gaps and phases.

The 1.5 GeV ring has for a number of user weeks been delivering single-bunch operation, where only one of the available 32 buckets are filled with electrons. In this case, the light pulses to the beam lines only occur at 3.12 MHz, instead of the usual 99.93 MHz. Thus, there is a time window of 320 ns during which time-resolved studies may be performed at the beamlines. This user mode has been automated, and usually the injections take place every second hour. The bunch is then injected up to 20–25 mA, about twice as high intensity as in multi-bunch mode, and is left to decay down to roughly half intensity. Of particular interest for accelerator studies, is the fact that 43 mA could be stored in a single bunch with no signs of collective effect instabilities, and further that 93 mA could be kept stable by help of a bunch-by-bunch feedback system, although with a higher energy spread than the natural one.

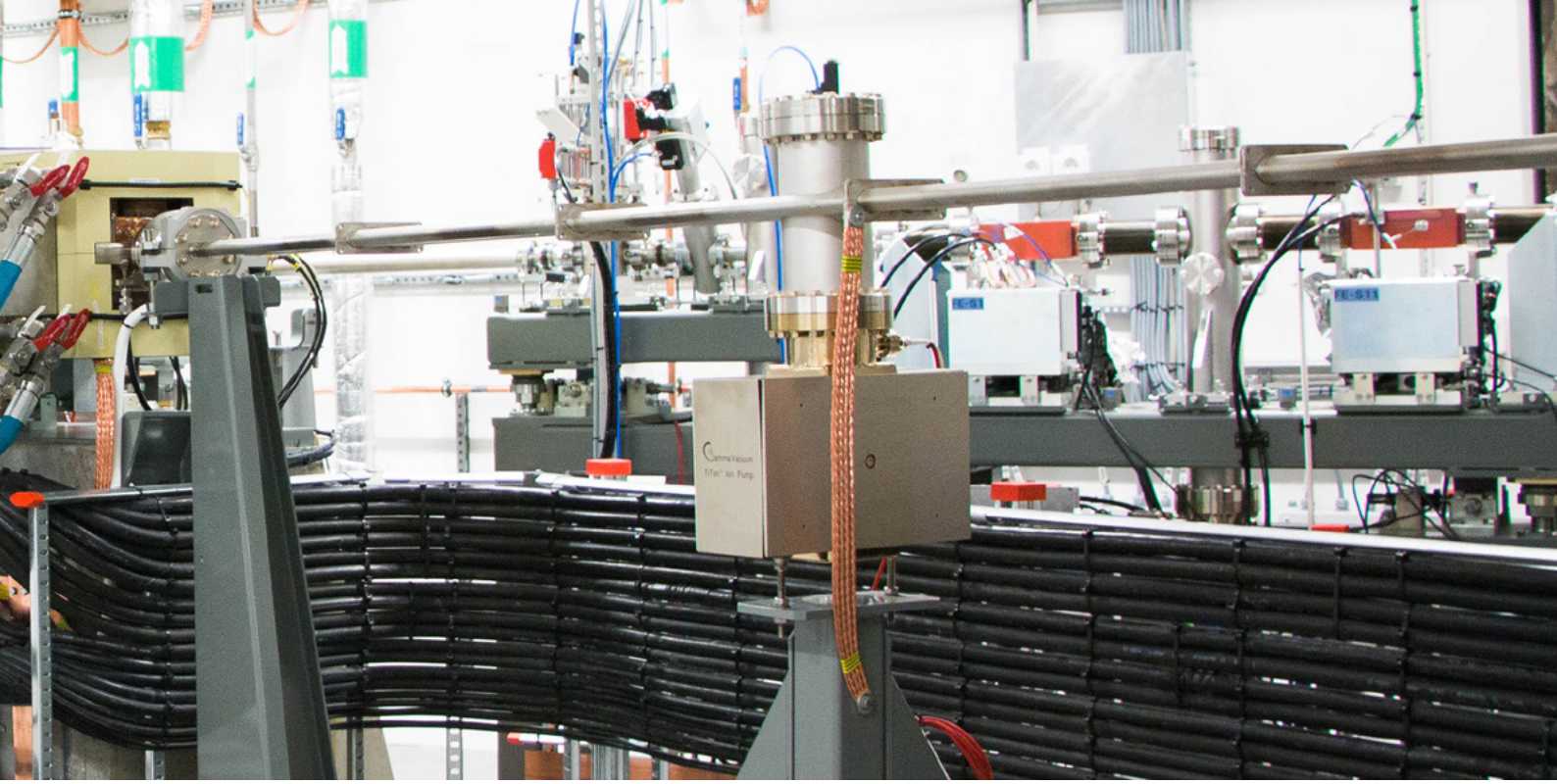

However, the bunch current lifetime is fairly short because of Touschek scattering, so for user operation it is still not feasible.

One fundamental problem regarding the single bunch operation is of course that those beamlines that are not specialized for time-resolved studies, will receive a much lower light intensity compared to the multi-bunch operation. This is not ideal for a user facility built for several beamlines working in parallel. One brilliant way to circumvent this deficiency might be the use of so-called Transverse Resonant Island Buckets (TRIBs). This is a scheme where possibly one bunch of electrons can be stored on a path either vertically or horizontally displaced from the rest of the bunches. Due to the dynamics of the storage ring, the single bunch will not follow the same path each turn, but rather close its orbit after three or four turns. However, this implies that for a beamline which wants to utilize the exceptional bunch, the light from firstly the ordinary bunches must be blocked, and secondly also the light from the exceptional bunch when it passes at yet another off centre position, if not the accelerator physicist succeed in only filling one of possibly three or four islands.

Local corrector magnets may be used to alter the local beam path through the undulator so that the exceptional bunch passes at the ordinary orbit. Initial tests of the implementation of TRIBS were performed in 2019 in the 1.5 GeV ring in a collaborative experiment with the beam dynamics team of BESSY. Figure 8 shows the result of these investigations, where the electrons were stored in exceptional buckets. The horizontal separation of these buckets is somewhat less than a milimetre.

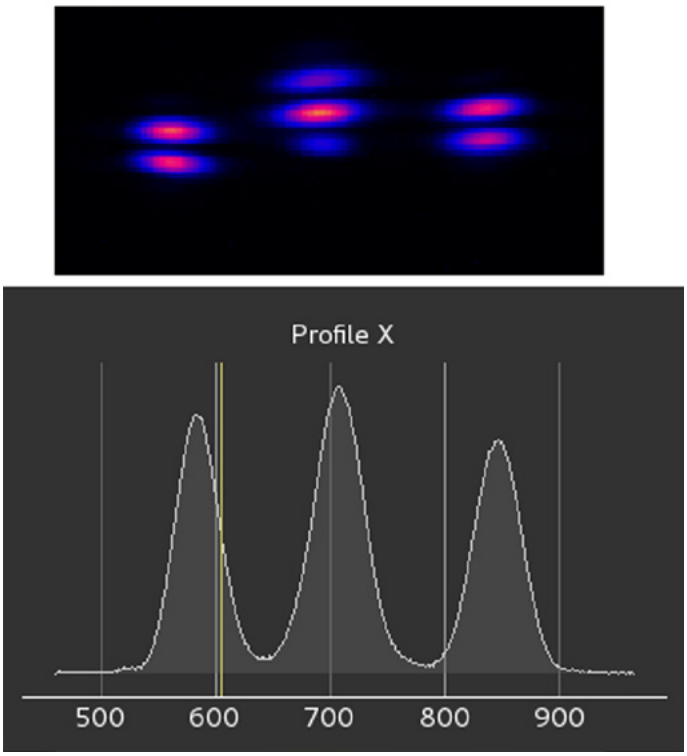

Fig. 8 Transverse Resonance Island Bucket Test in the 1.5 GeV ring

Linear Accelerator

Shortly after the completion of the linear accelerator (linac) building, in spring 2013, installation of the accelerator components started. After a year to complete installation, commissioning of the linac followed, with the first aim to deliver electron beam to the short-pulse facility (SPF) and light to the FemtoMAX beamline. Next in line was the 3 GeV storage ring and then finally the 1.5 GeV storage ring. All accelerators were commissioned successfully and are now several years into user operation.

The dual purpose of the linac, injector for the storage rings and high brightness SPF driver, puts additional demands on the fast switching between running modes. Every ten minutes, the 3 GeV ring is topped up to nominal current, using a thermionic gun as electron source. In between top-ups, beam is delivered to the SPF with a photogun as starting point of the acceleration. In the electron guns and the following accelerating structures, 3 GHz radio frequency (RF) electric fields push the electrons forward up to the nominal 3 GeV beam energy at the end of the linac.

In the photogun, electrons are emitted when an ultraviolet laser pulse hits the cathode inside the gun. This gives additional control and higher beam quality, compared to the thermionic gun, where electrons are emitted from a hot cathode surface.

The electron beam from the photogun is compressed in bunch duration in two stages, bunch compressor 1 and 2 (BC1 and BC2). Bunch compression relies on off-crest acceleration, which gives an energy chirp on the electron beam. Through the bunch compressor, different electron energies have different path length and by matching the off-crest phase and bunch compressor parameters, the compression can be tuned. The curvature of the sinusoidal accelerating electric field is imprinted on the electron energy distribution and, if no additional actions are taken, present also after compression. To reach extremely short bunches, linearization is required to straighten out the curvature. Adding accelerating structures at a multiple of the main frequency is the most common way of linearizing the sum field of all accelerating structures. This adds complexity, cost and energy jitter. The MAX IV approach is magnetic linearization. This is possible with our bunch compressor design based on arch shaped magnet arrangements rather than chicane shaped, which is the more conventional design.

Figure 9 (left) shows a measurement that gives information on the bunch duration after BC1. The measurement was carried out by adjusting the accelerator for hard compression and good linearization in BC1.

The start of the linear accelerator showing the thermionic gun to the left and the first accelerating structures to the right.

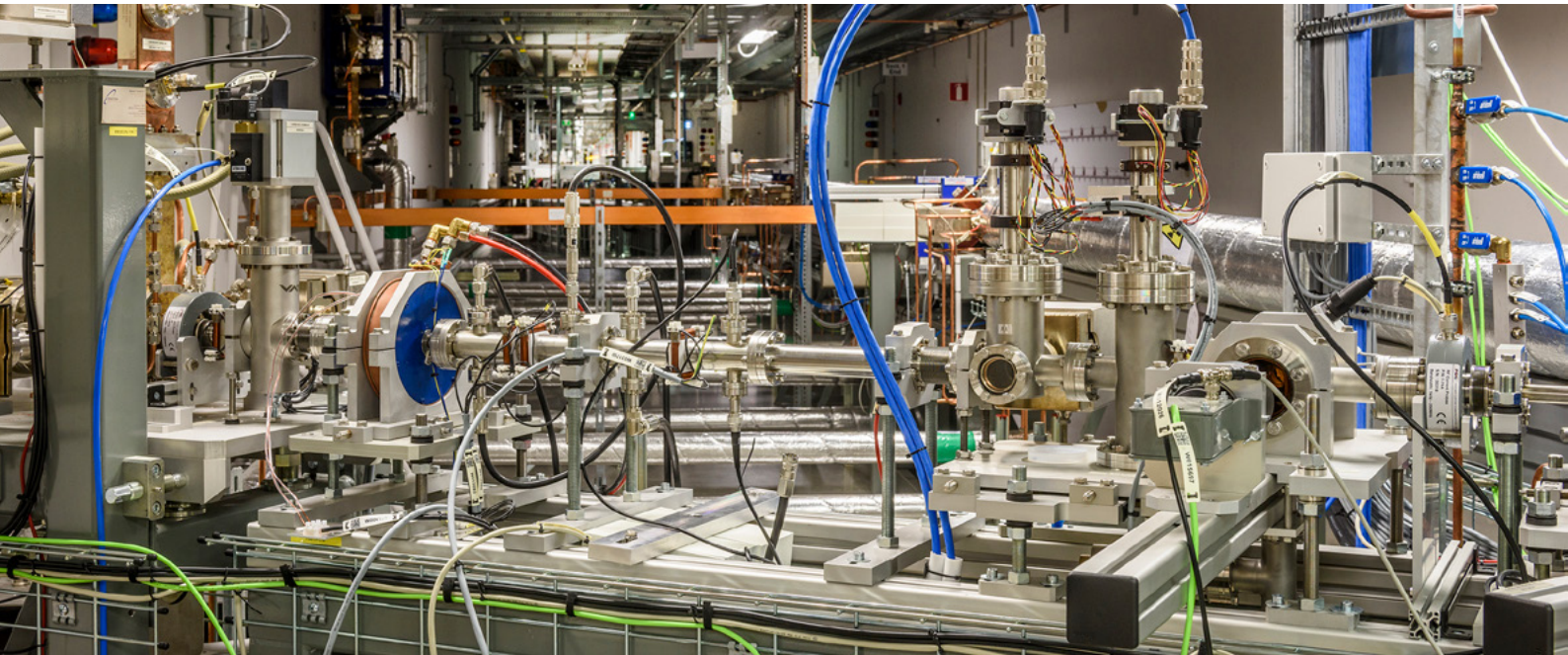

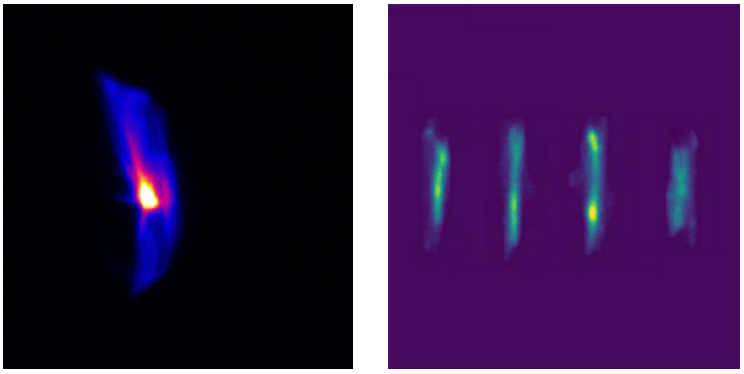

Figure 9: (left) Longitudinal distribution characterization of the linac beam. The horizontal axis is proportional to time and the pulse duration is 25 fs FWHM. (right) Multi-slit characterization of the beam from the gun test facility.

The rest of the accelerator functioned as a large streak camera. The horizontal direction in the picture is proportional to time. The measurement revealed a bunch duration of 25 fs FWHM after BC1. To measure the electron pulses after final compression in BC2, a transverse deflecting cavity (TDC), is currently under construction. The TDC will, in addition to bunch duration, give direct information on the chirp and how the beam parameters vary along the electron bunches. This will be important both for SPF tuning and free electron laser (FEL) development.

Our gun test facility is another important tool for accelerator development. The first measurements were carried out early 2019. The picture to the right in Figure 9 shows images of the electron beam during a slit scan.

The purpose of the measurement is to characterize the emittance of the beam emitted by the electron gun. Emittance is a measure of beam quality and how tight the beam can be focused. Currently a gun capable of low emittance, operation at 100 Hz, designed with the demands of an FEL in mind, is under construction, it will be fully characterized in the gun test facility before installation in the linac.

Accelerator references

[**1**] M. Eriksson et al., Commissioning of the MAX IV light source, IPAC2016, Busan, Korea. https://accelconf.web.cern.ch/ipac2016/papers/moyaa01.pdf

[**2**] P. F. Tavares et al., Commissioning and first-year operational results of the MAX IV 3 GeV ring, Journal of Synchr. Rad. (2018), https://doi.org/10.1107/S1600577518008111

[**3**] D. Olsson et al., "The Bunch-by-Bunch Feedback System in the MAX IV 3 GeV Ring", Technical Report LUTEDX/(TEAT-7253)/1-48/(2017) 7253. https://portal.research.lu.se/portal/files/33463876/TEAT_7253.pdf

[**4**] Å. Andersson et al., "Diagnostics at the MAX IV 3 GeV storage ring during commissioning", IBIC2016, Barcelona, Spain. https://accelconf.web.cern.ch/ibic2016/papers/moal02.pdf

[**5**] J. Breunlin at al., "Emittance diagnostics at the MAX IV 3 GeV storage ring", IPAC 2016, Busan, Korea. https://accelconf.web.cern.ch/ipac2016/papers/wepow034.pdf

[**6**] M. Sjöström et al., "Orbit feedback system for the MAX IV 3 GeV storage ring", IPAC 2011, San Sebastian, Spain. https://inspirehep.net/literature/1183604

[**7**] J. Kallestrup et al., "Studying the dynamic influence on the stored beam from a coating in a multipole injection kicker", IPAC 2019, Melbourne, Australia, https://doi.org/10.18429/JACoW-IPAC2019-TUPGW063

[**8**] Å. Andersson, "Experience with Multipole Injection at MAXIV", presented at the 2nd Topical Workshop on Injection andInjection systems, Villigen, Switzerland, Apr. 2019, https://indico.psi.ch/event/6972/

[**9**] P. Alexandre, "Development and Operation of a MultipoleInjection Kicker for SOLEIL and MAX IV", presented at the 2nd Topical Workshop on Injection and Injection systems,Villigen, Switzerland, Apr. 2019, https://indico.psi.ch/event/6972/

[**10**] P. F. Tavares et al., "Commissioning of the MAX IV Light Source", NAPAC 16, p. 439. http://accelconf.web.cern.ch/napac2016/papers/tub3io01.pdf

[**11**] V. Baglin, G. Bregliozzi, D. Calegari, J. M. Jimenez, G. Lanza, and G. Schneider, "The LHC Experimental Beam Pipe Neon Venting, Pumping and Conditioning", in Proc. 2nd Int. Particle Accelerator Conf. (IPAC'11), San Sebastian, Spain, Sep. 2011, paper TUPS017, pp. 1557-1559. https://accelconf.web.cern.ch/ipac2011/papers/tups017.pdf

[**12**] G. Skripka et al., "Commissioning of the harmonic cavities in the MAX IV 3 GeV ring", IPAC 2016, Busan, Korea. http://accelconf.web.cern.ch/ipac2016/papers/wepow035.pdf

[**13**] Å. Andersson et al., "The 100 MHz RF system for the MAX IV storage rings", IPAC 2011, San Sebastian, Spain. https://accelconf.web.cern.ch/IPAC2011/papers/mopc051.pdf

[**14**] M. Johansson et al., "Magnet design for a low-emittance storage ring", J. Synchrotron Rad. 21 (2014), 884–903, https://doi.org/10.1107/S160057751401666X

[**15**] S.C. Leemann et al., "First optics and beam dynamics studies on the MAX IV 3 GeV storage ring", Nucl. Instrum. Methods Phys. Res. A, 883, 33–47, https://doi.org/10.1016/j.nima.2017.11.072

[**16**] D. McGinnis, "Beam Stabilization and Instrumentation Systems based on Internet of Things Technology", 9th LLRF WS, Chicago, 2019. https://arxiv.org/abs/1910.07822

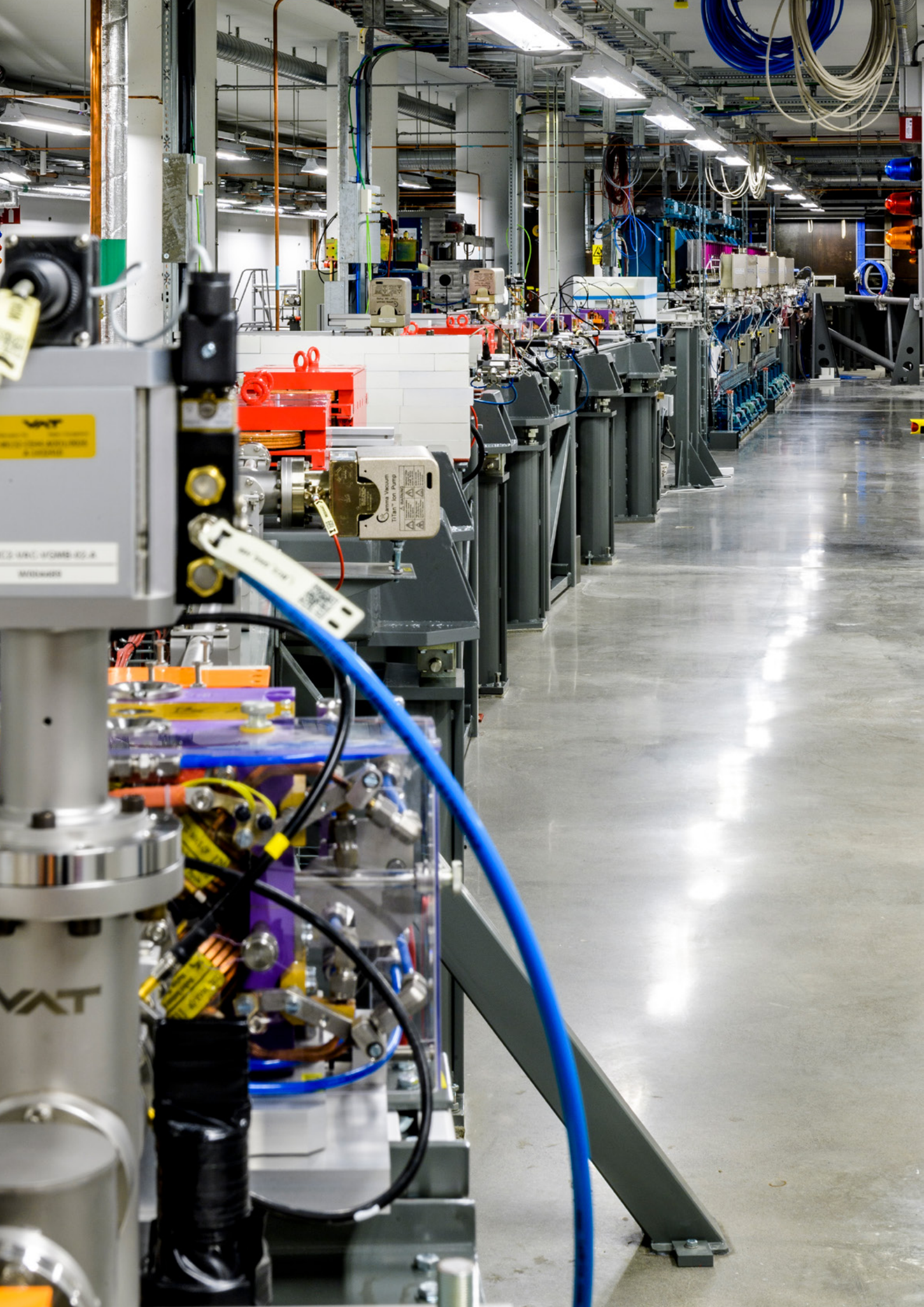
VAT
Gamma Vacuum
Titan™ Ion Pump

Future perspectives

In 2016, a user initiative was launched to enhance capabilities to deliver coherent ultra-short pulses in the soft X-ray region through the construction of a free-electron laser (FEL) driven by the 3 GeV linear accelerator at MAX IV. The science case includes atomic and molecular physics, condensed matter physics, chemistry and life science. The Soft X-ray Laser (SXL) will have a spectrally broad pumping range and take advantage of unique detection schemes as well as synergies with other beamlines at MAX IV.

SXL is a natural development step for the facility, since the MAX IV linac was already in the original design prepared in several ways to serve as an FEL driver.

The SXL design is optimized to produce radiation in the 1–5 nm photon wavelength range with full polarization control as well as two-pulse/two-colour schemes and is an opportunity for innovative developments in accelerator physics, FEL physics as well as insertion device and beamline instrumentation developments.

The layout below illustrates the setup, starting from a new BC2 ending in the SPF hall, and continuing with the FEL and two beamlines.

A conceptual design report (CDR) is currently being written and will be delivered in spring 2021. Particle tracking simulations have confirmed that the linac can produce very short electron bunches, down to 1 fs FWHM. To fully benefit from the short bunches, equally good timing stability is required. There are indications that the MAX IV linac already now have very low energy and timing jitter. The energy jitter in BC2 corresponds to a timing jitter of 15 fs RMS jitter. The low jitter can be achieved thanks to our self-compensating acceleration scheme where the biggest contribution to energy and timing jitter can be cancelled out. Other jitter sources have been localized and a plan for how to minimize the jitter to be comparable to the bunch duration is emerging and will be one essential part of the SXL CDR.

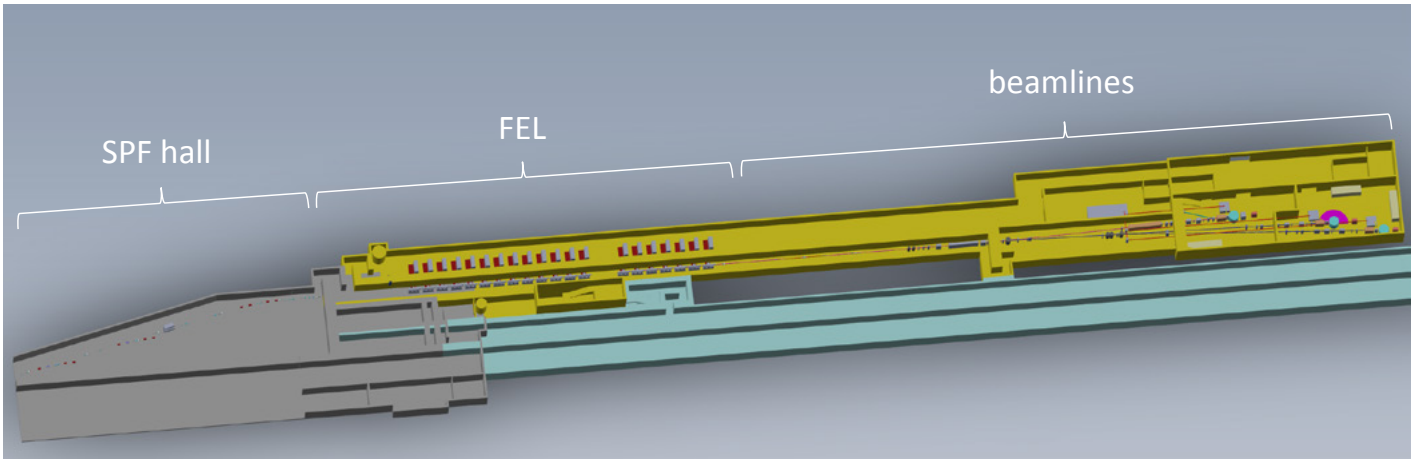

Facts & Figures

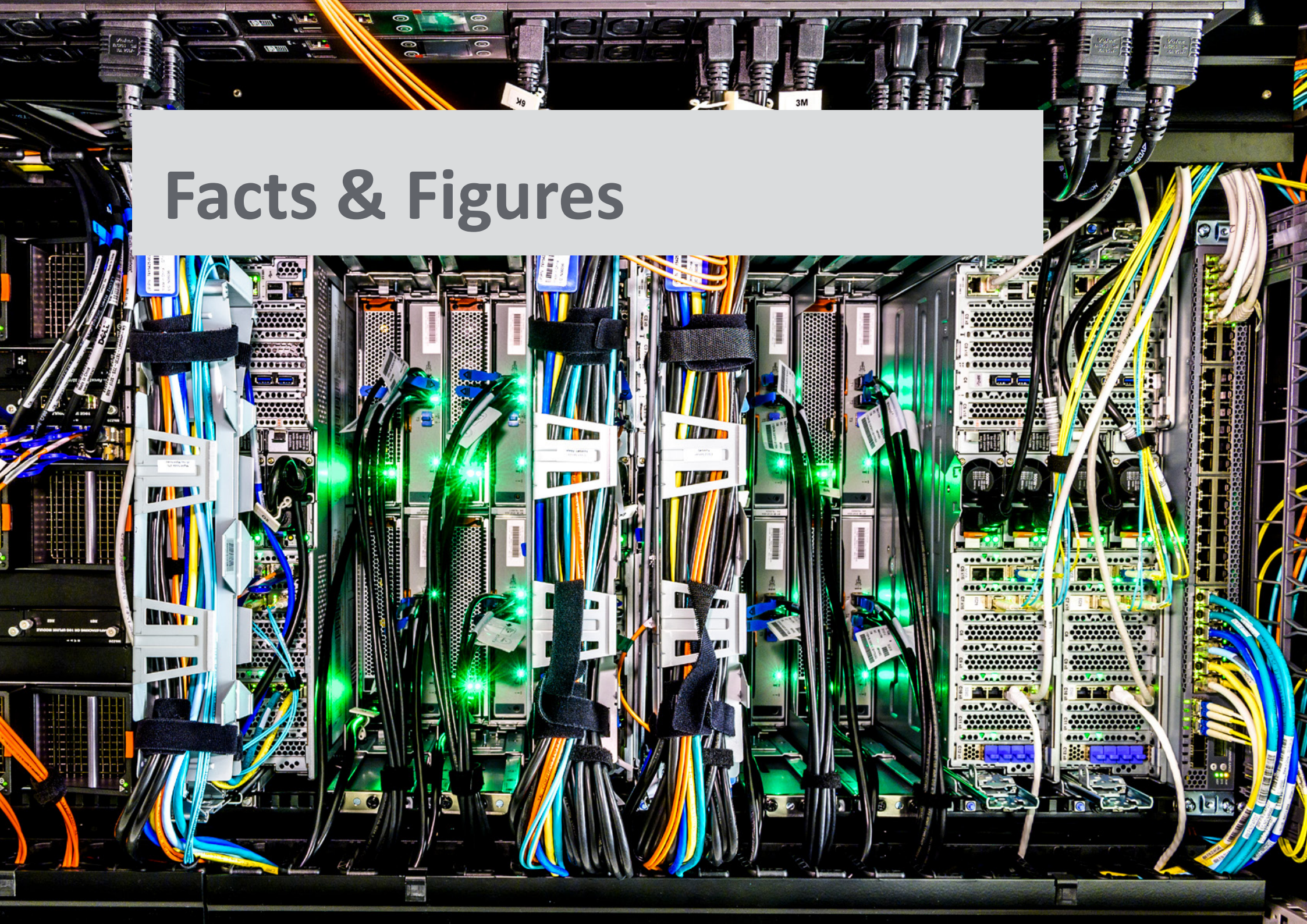


IBM
D1 D2 D3 D4 D5 D6 D7 D8 D9 D10 D11 D12
Power S812L
DVD
POWER8
4
ESS Storage 2U24
1 2 3 4 5 6 7 8 9 10 11 12 13 14 15 16 17 18 19 20 21 22 23 24
3
D1 D2 D3 D4 D5 D6 D7 D8
Power S822L
2
1

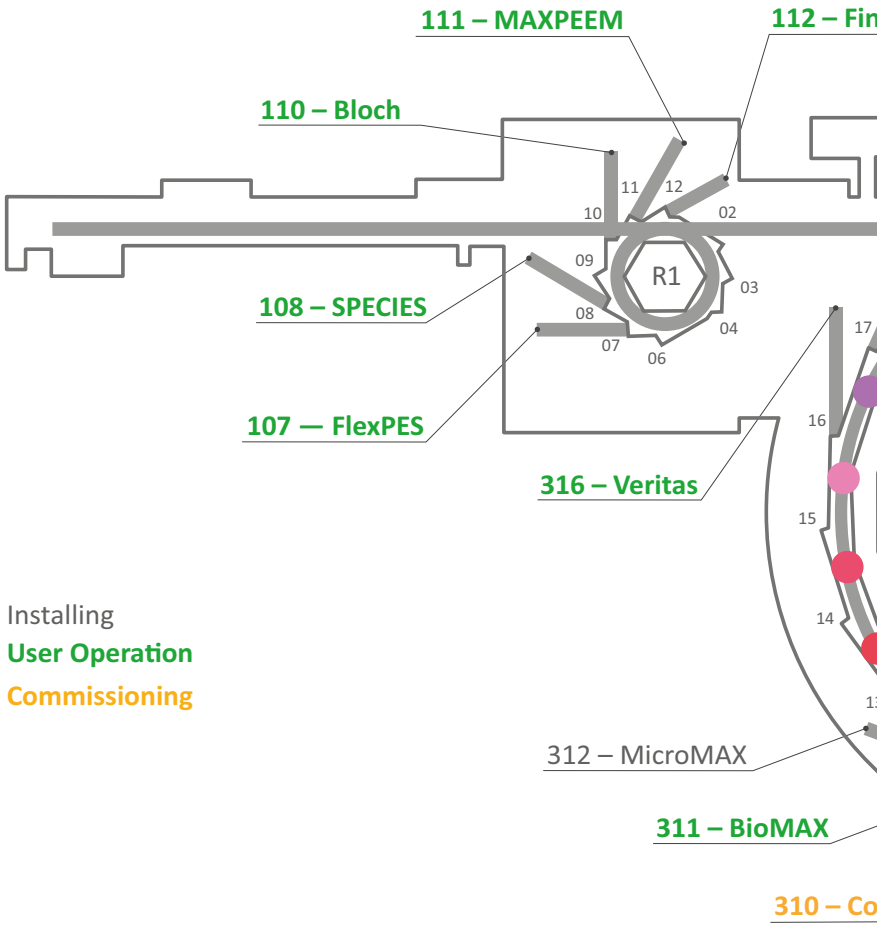

Currently funded beamlines at MAX IV. Numbers correspond to those in the map. Status in the map as per June 2020.

Beamline	No.	Accelerator	Technique
Balder	308	3 GeV	Hard X-ray absorption and emission spectroscopy (XAS, XES) and X-ray diffraction (XRD) with emphasis on in-situ and time resolved studies
BioMAX	311	3 GeV	Macromolecular crystallography with a high degree of automation and remote user access
Bloch	110	1.5 GeV	Angle resolved photoelectron spectroscopy (ARPES) including spin resolution (SPIN-ARPES) for studies of the electronic structure of solids and surfaces
CoSAXS	310	3 GeV	Small and wide angle X-ray scattering (SAXS, WAXS) and coherent techniques for soft matter and bio materials
DanMAX	304	3 GeV	Powder diffraction (XRD) and full-field tomographic imaging of hard (energy) materials
FemtoMAX	SPF	Linac	Time-resolved hard X-ray scattering (XRD) and spectroscopy (XAS) methods for studies of ultrafast processes
FinEstBeaMS	112	1.5 GeV	Electron and ion spectroscopies and luminescence methods for studies of low density matter and solids
FlexPES	107	1.5 GeV	Soft X-ray spectroscopies for studies of low density matter and solids

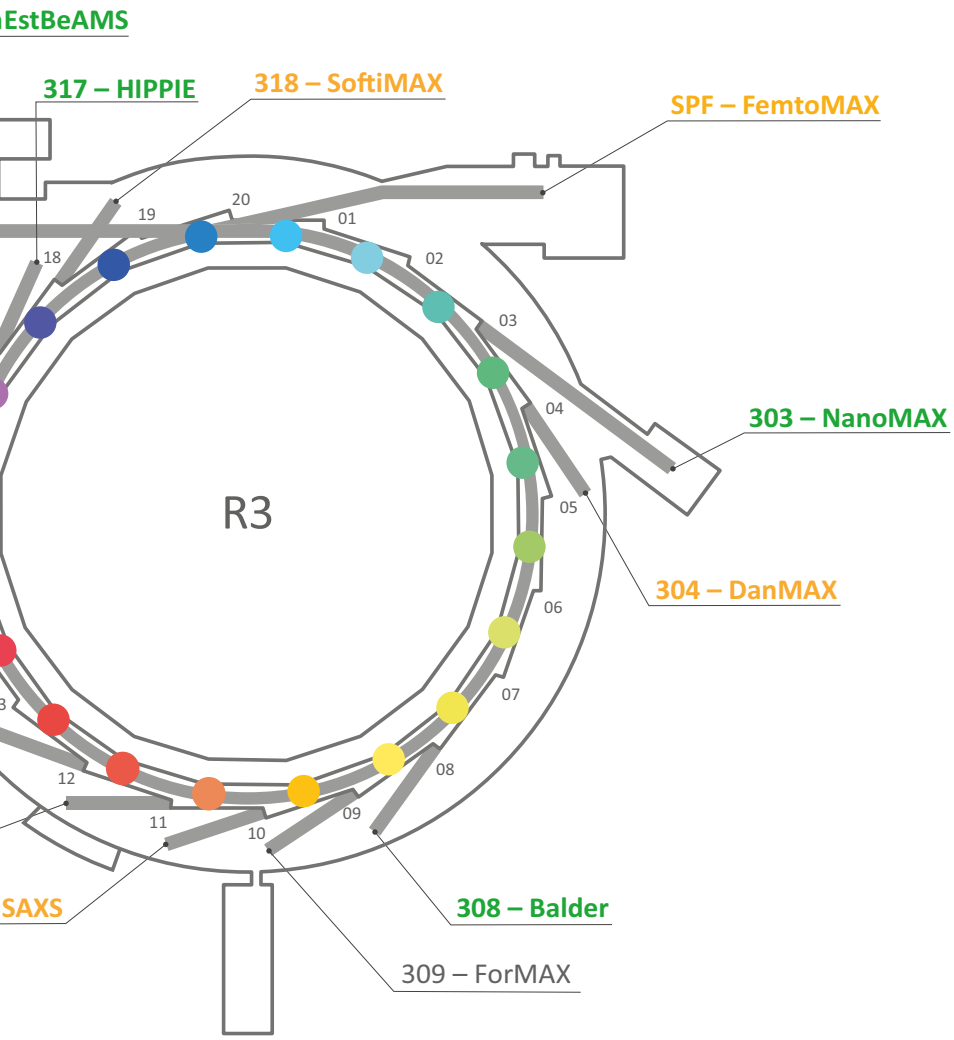

Beamline	No.	Accelerator	Technique
ForMAX	309	3 GeV	Full-field tomography, SAXS/WAXS, scanning SAXS/WAXS imaging
HIPPIE	317	3 GeV	Ambient Pressure Photoelectron Spectroscopy (APXPS) on solids and liquids
MAXPEEM	111	1.5 GeV	Photoelectron microscopy for investigation of surfaces and interfaces
MicroMAX	312	3 GeV	Macromolecular crystallography, serial crystallography, time-resolved crystallography
NanoMAX	303	3 GeV	Imaging with spectroscopic and structural contrast techniques on the nano scale
SoftiMAX	318	3 GeV	Scanning transmission X-ray microscopy (STXM) and coherent imaging methods
SPECIES	108	1.5 GeV	Resonant inelastic X-ray scattering (RIXS) and Ambient Pressure Photoelectron Spectroscopy (APXPS)
Veritas	316	3 GeV	Resonant inelastic X-ray scattering (RIXS) with unique resolving power and high spatial resolution

MAX IV in brief

MAX IV has 16 funded beamline projects. By the end of 2019, twelve of these were "taking light", four of which were in commissioning, and eight in general user operation. Procurement and construction of the remaining four beamlines are well underway, including for the ForMAX and MicroMAX beamline projects, the two most recently funded.

In particular, all five planned beamlines on the 1.5 GeV ring have been commissioned with three in general user operation, and the last two prepared to accept users in March 2020. Completing the planned beamline portfolio on the 1.5 GeV ring serves a long-standing Swedish soft X-ray spectroscopy and imaging community. MAX IV Biolab, a laboratory that supports Life Science experiments on various beamlines, opened during spring.

User Operations

User statistics in this chapter covers the period 1 March 2019 to 29 February 2020, following our proposal schedule.

By the end of this period, eight beamlines were in operation and received general users and three beamlines have been open to expert users.

In total, MAX IV Laboratory had 945 user visits by 662 individual users during the period. The user gender distribution was 33% women and 67% men. The vast majority of users came from the Nordic countries. In total, MAX IV had users from 30 different countries and 140 various institutions in this period.

There were two general user calls in 2019, one closing in March for beamtime from September 2019 to February 2020 and one closing in September was for beamtime from March to August 2020.

In 2019, BioMAX commissioned remote access mode, to increase efficiency and decrease costs for the beamline and its users. BioMAX is currently the only beamline at MAX IV, which is open for block allocation group (BAG) proposals. Accepted BAG proposals are valid for four beamtime cycles (two years). Out of the 40 submitted proposals to BioMAX in the 2019 call, fourteen were BAG-proposals.

The Covid-19 pandemic has affected user operation subsequently in 2020. At the time of printing approximately 50% of experiments scheduled since March 2020 had to be cancelled. Here, remote operation capabilities at BioMAX, but also flexible arrangements at other beamlines have helped to mitigate the impact.

MAX IV has dedicated 2 % of the beamtime for education and training initiatives. Eight courses with a total of around 100 participants have had beamtime for educational purposes between 1 March 2019 to 29 February 2020. Together these eight courses were allocated 144 hours of beamtime.

Beamline	User visits
Balder	154
BioMAX	308
Bloch	49
FemtoMAX*	11
FinEstBeAMS	109
FlexPES*	32
HIPPIE	89
MAXPEEM	29
NanoMAX	135
SPECIES-APXPS*	12
Veritas	17
Total	**945**

** Beamlines in commission*

User distribution per beamline - 2019-03-01 – 2020-02-29

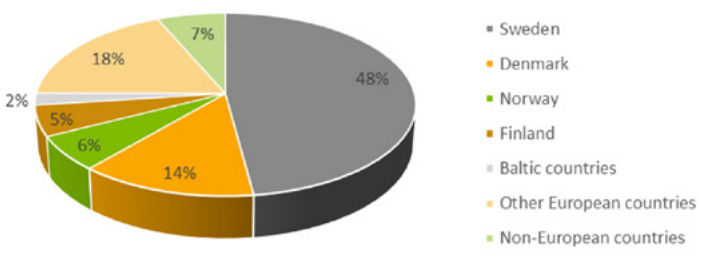

User distribution geographically - 2019-03-01 – 2020-02-29

User meeting

MAX IV hosted the 31st User Meeting at the Scandic Star hotel 23-25 September, 2019. The theme "Developing MAX IV: with the users, for the users" attracted over 300 scientists, researchers, and engineers, who attended to listen or give presentations, engage with colleagues, and display their work during the poster session.

After a welcome speech by the Director the attendees got updates from the user associations ESUO, SSUO and FASM, as well as from the User Office and Industry Office. The rest of the afternoon some of the beamlines presented their status and latest activities.

Day two of the programme was dedicated to parallel sessions on science and technology advancements with synchrotron light. There was palpable energy in the various rooms as groups gathered to hear their colleagues present and learn the latest developments in a wide range of subject areas, including coherent scattering opportunities in condensed matter, metal processing studies, structural biology with BioMAX, correlated electron materials and magnetism geology, archaeology, and cultural heritage.

The final day of the meeting opened with Nønne Prisle from the University of Oulu, with a talk on her research on climate change using FinEstBeAMS beamline. The latest User Highlights followed from BLOCH, MAXPEEM, NanoMAX, BioMAX, and HIPPIE beamlines as well as individual research topics from invited speakers.

Closing the meeting at the Banquet dinner, the winner of the best PhD student poster, Susanna Hammarberg, and winner of the best PhD thesis, Xiaocui Wang, received their awards.

Engaging Industy

Proprietary beamtime allocated at MAX IV increased in 2019, both in terms of hours and in terms of the number of organisations and beamlines used.

In total, 216 hours of proprietary beamtime was sold to eight different organisations at 22 scheduled occasions during 2019. BioMAX is the dominant beamline accepting proprietary users with several pharmaceutical companies and mediator companies buying beamtime; however, HIPPIE, Balder and NanoMAX also served proprietary users.

Three new user organisations came to MAX IV through Vinnova funded projects within the program for industrial pilot projects for utilisation of large-scale infrastructures for neutron and photon-based techniques.

Thematic initiatives are ongoing in these industrial sectors:

- Food & Packaging
- Life Science
- Metallic materials
- Energy materials
- Wood materials
- Textile
- Mechanical systems production & Scientific equipment production

Collaborations & partnerships

MAX IV is actively working to take advantage of the ever-increasing interest from other research facilities, research organisations, companies and scientists worldwide. MAX IV participates actively in several projects, for example, LEAPS – League of European Accelerator-based Photon Sources, lightsources.org, PARI – workshop on Public Awareness of Research Infrastructures, EuroScience Open Forum (ESOF), Big Science Business Forum and Big Science Sweden. These projects all aim to raise awareness of synchrotron and/or neutron techniques through targeted outreach both to users, funders and the general public.

The MAX IV KITS (Controls and IT) group are part of the Horizon 2020 funded project, ExPaNDS (EOSC Photon and Neutron Data Services) that started in September and runs to 2022 together with ten other research infrastructures. ExPaNDS's ambition is to enrich the European open science cloud with data management services, to coordinate activities to facilitate national photon and neutron research infrastructures to make the majority of their data 'open' following FAIR principles and to enable sharing of data in a uniform way.

Finance

With 2019, a new five-year funding period of the operation of MAX IV Laboratory started. In 2019 MAX IV operation was supported by the Swedish Research Council (VR) under contract 2018-07152, the Swedish Governmental Agency for Innovation Systems (Vinnova) under contract 2018-04969, and Formas under contract 2019-02496.

Operations funding has also been recieved from Chalmers University of Technology, Gothenburg University, Karlstad University, Karolinska Institutet, KTH Royal Institute of Technology in Stockholm, Linköping University, Linnæus University, Luleå University of Technology, Lund University, Malmö University, Stockholm University, Swedish University of Agricultural Sciences (SLU), Umeå University and Uppsala University, and the Academy of Finland.

The total funding for 2019 was 435 MSEK and the total result -14 MSEK, which was in line with the budget. The outgoing agency capital was 32 MSEK.

Organisation & staff

At the end of 2019, MAX IV Laboratory had 254 employees. All parts of the organisation have been strengthened by new recruitments, although the vast majority have been of staff members for beamlines and to the Controls & IT group as more beamlines have become operational. About one-third of MAX IV employees are from countries other than Sweden.

In September 2019, Ian McNulty was appointed Director of MAX IV Laboratory. Conny Såthe, group manager for the Spectroscopy group, was appointed interim Physical Science Director.

MAX IV has a new Board from 1 January 2020:

- Peter Honeth (Chair), former State Secretary, Ministry of Education and Research, Sweden
- Massimo Altarelli, EuXFEL/Max Planck Institute, Germany
- Lise Arleth, University of Copenhagen, Denmark
- Paula Eerola, University of Helsinki, Finland
- Torbjörn Holmström, Volvo Group, Sweden
- Aleksandar Matic, Chalmers University of Technology, Sweden
- Ingmar Persson, Swedish University of Agricultural Sciences, Sweden
- Anna Sandström, AstraZeneca, Sweden
- Stacey Sörensen, Lund University, Sweden

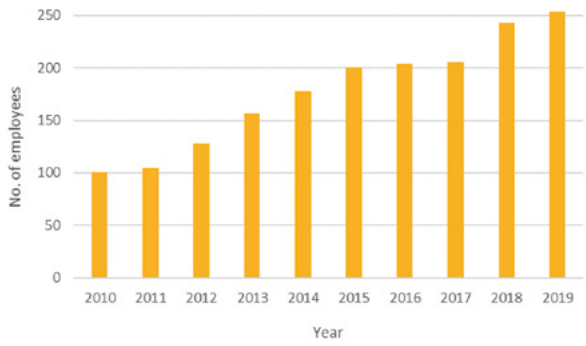

End of year numbers of MAX IV Laboratory employees for the years 2010-2019

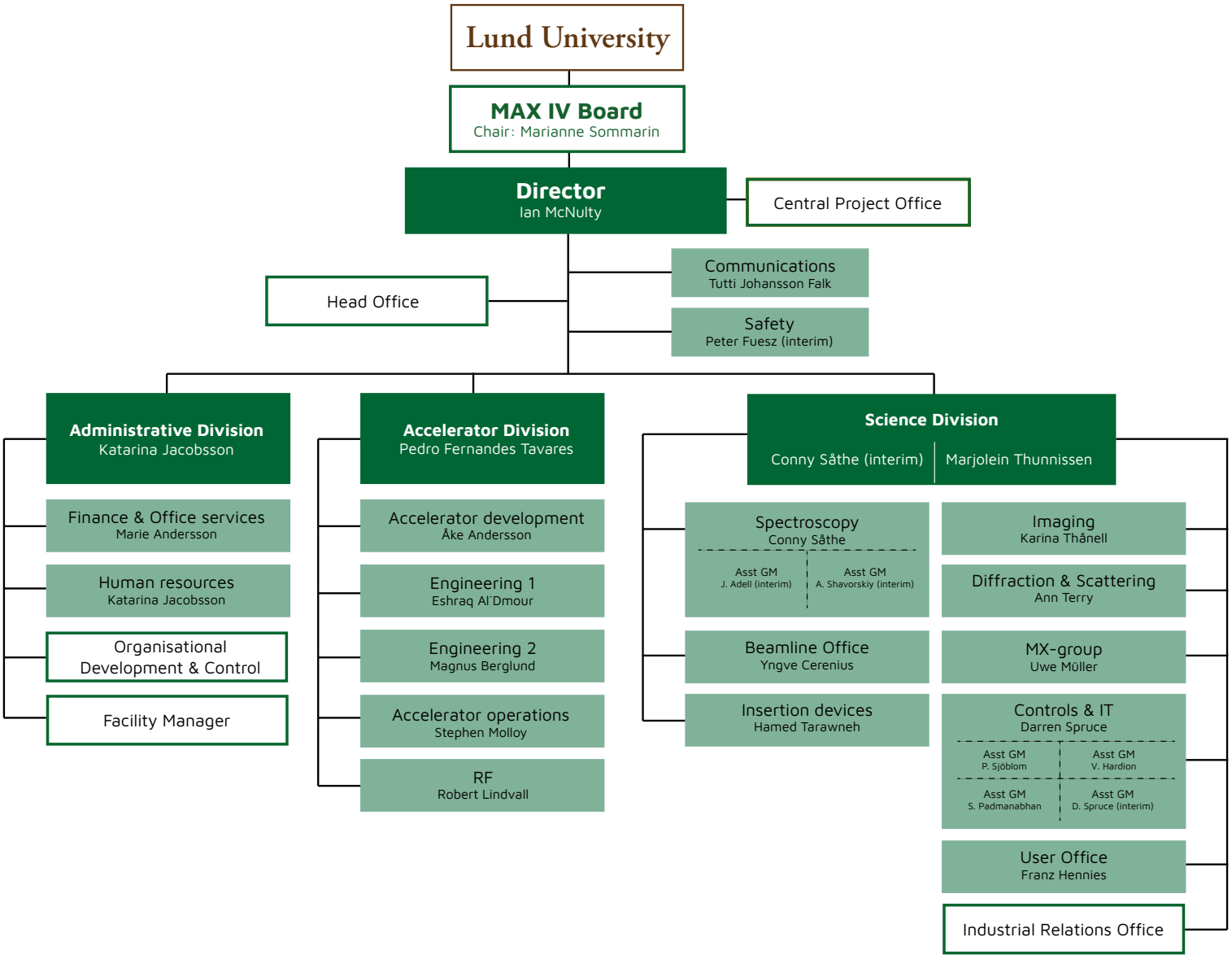

MAX IV organisation 31 December 2019

Follow us on

 twitter.com/MAXIVLaboratory

 facebook.com/MAXIVLAB

 instagram.com/maxivlaboratory

 linkedin.com/company/max-lab

 vimeo.com/MAXIVLaboratory

 youtube.com/MAXIVLaboratorySweden

 maxiv.se/public-media/podcast

MAX IV Laboratory
Lund University
PO Box 118
SE-221 00 Lund
Sweden

Tel: +46 (0)46 222 98 72
maxiv.se

Design & Edit: Tutti Johansson Falk
Photos & Illustrations: Madeleine Schoug, Emelie Hilner, Filippo Guizzetti, Kenneth Rouna, Tutti Johansson Falk, Pedro Fernandes Tavares, Stephen Molloy, Uwe Mueller, Noelle Walsh, Mirja Carlsson Möller